Development and validation of HRCT airway segmentation algorithms

ANEAL CHANDRA

BSc (Hons), MSc

This thesis is submitted in fulfillment of
the requirements of the degree Doctor of Philosophy.

Electron Microscopy Unit

Faculty of Science

THE UNIVERSITY OF SYDNEY

March 2009

Dedication

To my boys, Jasper, Oliver and Edward

The work presented in this thesis is my own unless otherwise stated.

Signed

Aneal Chandra

Abstract

Direct measurements of airway lumen and wall areas are potentially useful as a diagnostic tool and as an aid to understanding the pathophysiology underlying lung disease. Direct measurements can be made from images created by high resolution computer tomography (HRCT) by using computer-based algorithms to segment airways, but current validation techniques cannot adequately establish the accuracy and precision of these algorithms.

A detailed review of HRCT airway segmentation algorithms was undertaken, from which three candidate algorithm designs were developed. A custom Windows-based software program was implemented to facilitate multi-modality development and validation of the segmentation algorithms.

The performance of the algorithms was examined in clinical HRCT images. A centre-likelihood (CL) ray-casting algorithm was found to be the most suitable algorithm due to its speed and reliability in semi-automatic segmentation and tracking of the airway wall. Several novel refinements were demonstrated to improve the CL algorithm's robustness in HRCT lung data.

The performance of the CL algorithm was then quantified in two-dimensional simulated data to optimise customisable parameters such as edge-detection method, interpolation and number of rays. Novel correction equations to counter the effects of volume averaging and airway orientation angle were derived and demonstrated in three-dimensional simulated data.

The optimal CL algorithm was validated with HRCT data using a plastic phantom and a pig lung phantom matched to micro-CT. Accuracy was found to be improved compared to previous studies using similar methods. The volume averaging correction was found to improve precision and accuracy in the plastic phantom but not in the pig lung phantom. When tested in a clinical setting the results of the optimised CL algorithm was in agreement with the results of other measures of lung function.

The thesis concludes that the relative contributions of confounders of airway measurement have been quantified in simulated data and the CL algorithm's performance has been validated in a plastic phantom as well as animal model. This validation protocol has improved the accuracy and precision of measurements made using the CL algorithm.

Acknowledgments

I would like to thank my Supervisors Dr Allan Jones, Associate Professor Greg King and Dr Arndt Meier for their support and encouragement during the last five years. Greg has always kept me on track by asking the right questions and Allan has always given me the most pertinent advice on how to answer those questions.

I am indebted to Brent McParland for his surgical skills and advice preparing the pig lung phantom. I would like to thank Peter Chicco for his help devising the initial CL algorithm.

I am grateful to the staff and students of the EMU and the Woolcock Institute especially Daniel Hayley and Leigh Stephenson (EMU) and Nathan Brown and Jessica Dame Carroll (Woolcock) for their enjoyable and thought-provoking discussion.

HRCT scanner access was provided by Janine Gibbs at the Royal North Shore Hospital and John Magnussen at the Royal Prince Alfred Hospital Radiology Departments. Thank you for making the time to carry out the HRCT scans when faced with huge patient demands.

Last but not least, a big shout out to Katie for her awesome editing skills and day-to-day optimism in the face of what seemed like a mammoth task.

The project would have not been possible without the financial assistance from the Woolcock Institute of Medical Research, Pharmaxis Ltd, Australia, the CRC for Asthma and the Australian Research Council (ARC Linkage Grant #LP0562715)

Contents

List of tables

List of figures

CHAPTER 1

Introduction

For many years, the diagnosis of asthma and other lung diseases has relied on global pulmonary function tests (PFTs). PFTs such as spirometry are insensitive to changes in regional lung structure and function.

Early detection and treatment can lower the cost of lung disease and potentially enhance the survival of patients (Gomez, Rodriguez-Roisin et al. 2002). In order to detect lung disease in its earliest stages, the lung structure and function must be measured on both global and localised levels (Hogg, Macklem et al. 1968).

The Woolcock Institute of Medical Research's *Monitoring Devices* program has been exploring alternative diagnostic techniques that might allow regional analysis within the lung. Modern imaging techniques, and High Resolution Computed Tomography (HRCT) in particular, now provide the capability to measure airway dimensions *in vivo.* Direct assessment of the the magnitude and distribution of airway lumen narrowing and airway wall thickening is potentially useful as a diagnostic tool and as an aid to understanding the pathophysiology underlying lung disease (King, Muller et al. 1999; King, Carroll et al. 2004).

The HRCT image analysis algorithms used in this thesis began as software support for the *Monitoring Devices* program within the Woolcock Institute of Medical Research. As the project developed, it became apparent that the program needed a validation protocol for the algorithms used to evaluate airway changes found in asthma and chronic obstructive pulmonary disease (COPD). This thesis describes the development of a suitable algorithm and the validation protocol to establish its precision and accuracy.

1.1 Lung structure and function

The lungs consist of respiratory airways within a sponge-like structure, the parenchyma. The airways are tubes, known as bronchioles, which continually divide from the trachea downwards to form an inverted tree-like structure (Burrowes, Swan et al. 2008). As the main airway divides, the branches become smaller, terminating at alveoli as shown in Figure 1.1 below.

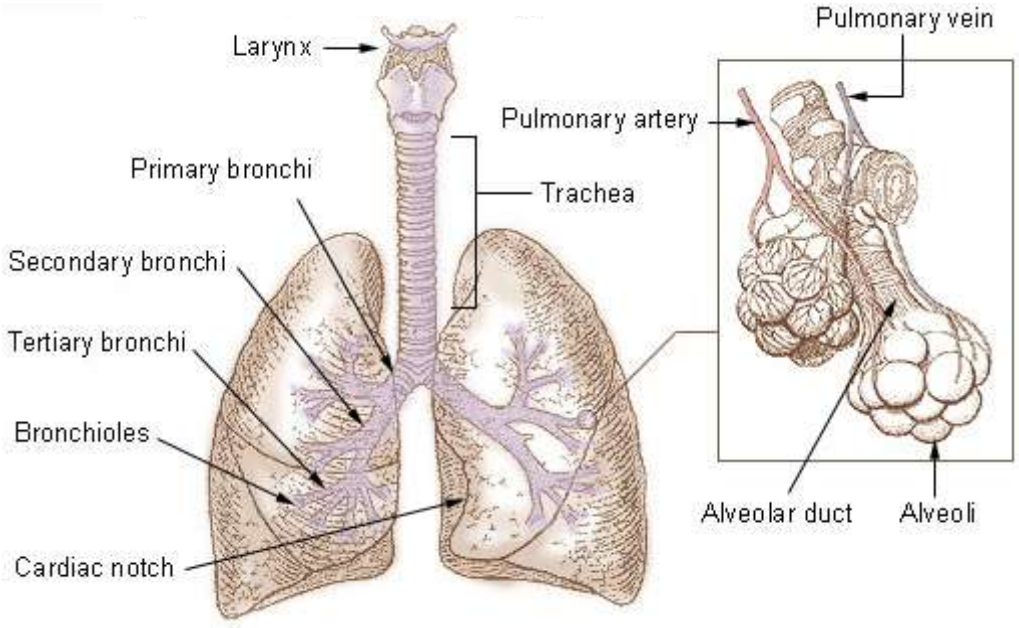

Figure 1.1: Simplified representation of bronchi, bronchial tree and lungs

Source: http://training.seer.cancer.gov/anatomy/respiratory/passages/bronchi.html; last accessed 20/3/09.

The trachea and larger bronchi contain c-shaped rigid bars of cartilage in their walls (Reid 1976). The cartilage helps to keep the airway from collapsing when there is negative pressure in the airway, as occurs during inhalation. The walls of the bronchi contain smooth muscle that can cause the airway to expand or contract (Beachey 2007). For example, during exercise, the airway expands to increase airflow ventilation. Conversely, when exposed to polluted or very cold air, the airway contracts to protect the downstream tissues from injury.

In addition to muscle, the normal bronchial walls contain many other types of cells (Figure 1.2). The innermost layer, the epithelial lining, contains goblet cells, which secrete mucous to lubricate the airways and trap inhaled foreign material such as bacteria, viruses, and pollutants (Catallo, Kennedy et al. 2001).

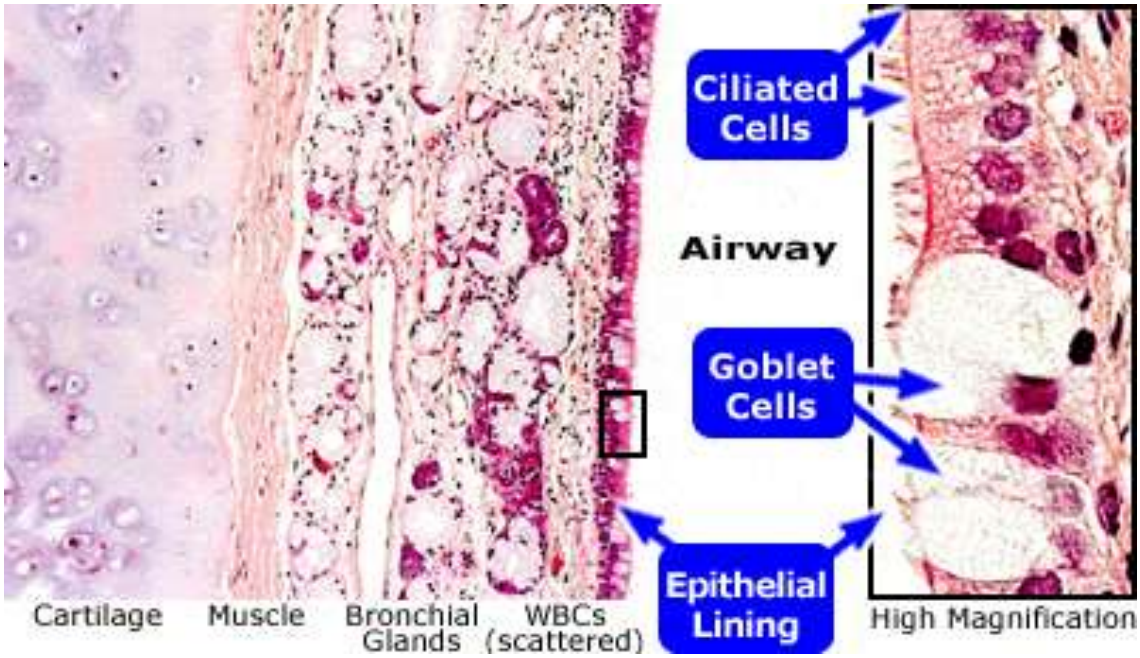

Figure 1.2: Microscopic section of a normal bronchial wall

Source: http://www.medicinenet.com/smokers_lung_pathology_photo_essay/article.htm; last accessed 3/02/09

Beneath the lining of the airway, inflammatory cells such as neutrophils, lymphocytes, and macrophages destroy or engulf any inhaled foreign material that becomes trapped in the mucus. In doing so, however, the inflammatory cells create debris. To help dispose of the debris, most of the cells that line the airway have fine hair-like projections known as *cilia*. These ciliated cells sweep and push the foreign material and debris up into the larger airways where they can be coughed up or spat out (Beachey 2007).

In humans the trachea divides at the level of the fifth thoracic vertebra into two main stem bronchi (the first generation), which continually subdivide into shorter and narrower airways, down to the 23rd generation that ends with the alveoli (Weibel and Gomez 1962). Assuming airways have dichotomous branching there will be approximately 8 million airways and 14 million alveolar ducts. Gaseous exchange via the pulmonary arterial blood supply occurs in the lower part of the airway tree, from the 17th generation. Here, the airways have become deeply embedded in the lung parenchyma and are kept open to maintain airflow by the elastic recoil of the surrounding tissue (Saetta, Turato et al. 2000).

The function of the lungs is optimised by aligning ventilation and pulmonary blood flow at a regional level, allowing the satisfaction of the metabolic requirements of the body at the lowest energy cost (Wilson 1967). The efficiency of this system is highly dependent on the structure and shape of the airways. Efficiency decreases with disease because lung disease alters the structure of the lungs, leading to changes in pulmonary airflow and reduction of the ventilation and perfusion matching (Beachey 2007).

1.2 Airway disease

Diseases of the airways are a common and significant cause of illness and death, with around 15 per cent of the global burden of all disease (Khaled, Enarson et al. 2001). The two most common airway diseases, asthma and chronic obstructive pulmonary disease (COPD), are considered here.

1.2.1 Asthma

Asthma is a chronic or recurring inflammatory condition in which the airways develop increased responsiveness to various stimuli. The disorder is characterised by bronchial hyper-responsiveness, inflammation, increased mucus production and intermittent airway obstruction. During an asthma attack, the lining of the bronchial tubes swells, causing the airways to narrow and reducing the flow of air into and out of the lungs. The symptoms of asthma, which can range from mild to life threatening, can usually be controlled with a combination of drugs and environmental changes.

Asthma has a relatively low fatality rate compared to other chronic diseases, but worldwide 255,000 people nevertheless died of asthma in 2005 (WHO 2008). Recurrent asthma symptoms frequently cause sleeplessness, daytime fatigue, reduced activity levels and school and work absenteeism. According to World Health Organization (WHO) estimates, 300 million people suffer from asthma (WHO 2008). Asthma is the most common chronic disease among children.

Public attention in the developed world has recently focused on asthma because of its rapidly increasing prevalence, affecting up to one in four urban children. However, asthma is a public health problem for all countries, regardless of development. Over 80 per cent of asthma deaths occur in low and lower-middle income countries. Asthma deaths will increase by almost 20 per cent in the next 10 years if urgent action is not taken (WHO 2008).

Asthma is under-diagnosed and under-treated, creating a substantial burden to individuals and families and possibly restricting individuals' activities for a lifetime.

Although the fundamental causes of asthma are not completely understood, the strongest risk factors for developing asthma are inhaled asthma triggers (Dougherty and Fahy 2009). These include:

- indoor allergens (for example, house dust mites in bedding, carpets and stuffed furniture, pollution and pet dander)
- outdoor allergens (such as pollens and moulds)

- tobacco smoke
- chemical irritants such as plicatic acid and isocynates in the workplace.

Allergy is only one risk factor for asthma. Other triggers can include cold air, extreme emotional arousal such as anger or fear, and physical exercise. Even certain medications can trigger asthma, such as aspirin and other non-steroid anti-inflammatory drugs, and beta-blockers (used to treat high blood pressure, heart conditions and migraine). Family history, early childhood infection and urbanisation has also been associated with an increase in asthma, although the exact nature of these relationships are unclear (Mansour, Lanphear et al. 2000).

In most cases, a physician can diagnose asthma on the basis of typical findings in a patient's clinical history and examination. Asthma is strongly suspected if a patient suffers from eczema or other allergic conditions—suggesting a general atopic constitution—or has a family history of asthma. However, physiological testing to find evidence of reversible airway obstruction is recommended to confirm the diagnosis (Sugiyama, Sagara et al. 2008).

Spirometry

In adults, the most reliable method of asthma diagnosis is by spirometry. This pulmonary function test (PFT) uses a spirometer to measure the amount of air entering and leaving the lungs. The patient exhales and inhales deeply, then seals his or her lips around the mouthpiece and blows as forcefully and for as long as possible until all the air is exhaled from the lungs.

Ideally, the patient should exhale for at least 6 seconds. The spirometer measures the amount of air exhaled and the length of time it took to exhale it. The amount of air exhaled in the first second, expressed as "FEV1", is measured and compared to the total amount exhaled. If the amount exhaled in 1 second is disproportionately low to the total exhaled, the patient has an obstruction. To test for reversibility, the patient then inhales a bronchodilator and the spirometry is repeated. If the values of the test performed after administration of the bronchodilator are significantly better than the pre-bronchodilator values, the obstruction is considered reversible.

Sometimes a patient with asthma does not demonstrate reversibility after the inhalation of a bronchodilator. In this case, the patient may be treated for a few weeks with anti-inflammatory medications and then returns for another spirometry test. If the post treatment spirometry results are better than the initial results, the obstruction is considered reversible.

Bronchial challenge testing

Occasionally, a patient with a suspected asthma-related airway obstruction does not demonstrate obstruction in spirometry or peak flow monitoring. In this circumstance, the diagnosis of airway obstruction may be provided by bronchial provocation.

Bronchial provocation, also known as bronchoprovocation and bronchial challenge, identifies and characterises hyper-responsive airways by having the patient inhale an aerosolised chemical, called a broncho-spastic agonist, that triggers a hyper-responsive reaction (Minasian, Wallis et al. 2008). The chemicals most often used are histamine and methacholine.

Patients perform spirometry without inhaling the agent and then inhale increasingly higher doses of the agent. After each incremental dose inhalation, spirometry is performed. Patients who demonstrate a reduction in FEV1 of 20% with a low dose of methacholine or histamine have nonspecific hyper-responsiveness. Although some patients without asthma demonstrate hyper-responsiveness, most patients with a positive reaction have asthma.

The other common bronchoprovocation test is the exercise challenge test, which is used primarily with patients whose asthma is triggered by exercise. The patient performs spirometry and then exercises, usually on a treadmill or exercise cycle. The exercise test should resemble as closely as possible the conditions under which the symptoms are usually triggered. After the patient exercises, spirometry is repeated. This may be done several times, immediately after exercise and periodically, until there is a drop in the FEV1 greater than 20% or until 30 minutes have elapsed.

Testing peak flow at rest (or baseline) and after exercise can be helpful, especially in young asthmatics, who may experience only exercise-induced asthma. If the diagnosis is in doubt, a more formal lung function test may be conducted. Once a diagnosis of asthma is made, a patient can use peak flow meter testing to monitor the severity of the disease (Enright and McCormack 2008).

Problems with current tests

While measurement of lung function is possible for adults, most new cases of asthma are diagnosed in children who are unable to perform such tests. Diagnosis in children is based on a careful compilation and analysis of the patient's medical history and subsequent improvement with an inhaled bronchodilator medication. Enright and Enright (2008) have suggested that spirometry-based testing is poorly understood, hard to administer and evaluate, and has both false positive and false negative results.

1.2.2 Chronic obstructive pulmonary disease

Chronic obstructive pulmonary disease (COPD) is an umbrella term for a group of airway diseases that are characterised by airflow obstruction or limitation, including chronic bronchitis, emphysema and bronchiectasis (Gomez, Rodriguez-Roisin et al. 2002). The most common cause is tobacco smoking, but COPD can also be caused by exposure to other airway irritants like coal dust or solvents. In some cases, the cause is unknown (idiopathic COPD), or the disease may arise due to congenital defects.

COPD is a major public health problem internationally. It is the fourth leading cause of chronic morbidity and mortality in Australia (Berend 2001), and the World Health Organisation (WHO) predicts that COPD will become the fourth leading cause of death worldwide by 2030. According to WHO estimates, 80 million people have moderate to severe COPD and three million people died of COPD in 2005 (WHO 2008).

At present just over 2 million Australians are estimated to have COPD, equating to nearly 1 in 5 (18.6 per cent) people aged 40 or over (Poulos, Toelle et al. 2005). Of these, 1.2 million people have COPD severe enough that its symptoms are starting to or have already affected the way they live their daily lives. The other 900,000 people will have a mild form of COPD where symptoms are often ignored or mistaken for ageing or even asthma. Many of these will go on to develop more severe forms of COPD if they do not take appropriate action (Asia Pacific 2005).

Almost half of all those with COPD are still in the prime of their working lives, and 57 per cent of all people with COPD are women. COPD is more common in any given year than the most common types of cancer, road traffic accidents, ear disease or diabetes. If nothing is done to change the current trends, in 2050 an estimated 4.5 million Australians will have COPD — with 2.6 million of those having moderate to very severe COPD (Frith, Cafarella et al. 2008).

There is general agreement in the literature that COPD has long been under-diagnosed both in Australia and across the world (Lamprecht, Schirnhofer et al. 2008). Under-diagnosis is a significant issue because the earlier COPD is diagnosed, the earlier steps can be taken to improve lung health and to prevent further damage to the airways. Early intervention is the key to reducing the progression of the disease into stages that cause significant impacts on quality of life and costs to the health system (Access Economics Report, 2008). This has ensured that more accurate, and early diagnosis will remain a research priority in the field of respiratory health.

COPD is primarily caused by noxious particles or gases, most commonly from smoking, which trigger an abnormal inflammatory response in the lung (Rennard 2002; Rabe, Hurd et al. 2007). Smoking damages the cilia. The damaged cilia cannot efficiently move

the mucus and, as a result, mucus builds up in the lungs and thickens. When this occurs the lungs become vulnerable to infections. The airways become swollen and begin to narrow when irritants stay in the lungs for an extended period of time. Over time, it is thought that proteolytic activity from the resultant inflammatory cells destroy the lung elastic ability, and making breathing harder (Rabe, Hurd et al. 2007). The loss of elasticity causes the lungs to become flaccid, decreasing their ability to exhale resulting in air becoming trapped. This "hyperinflation" of the lungs makes it difficult and uncomfortable to breathe (Saetta, Turato et al. 2000).

While PFTs are considered the gold standard for assessing several lung properties, they only provide global information describing lung function and structure. Some researchers believe COPD-related changes occur at the small airways (Hogg, Macklem et al. 1968). Since small airways have a relatively minor contribution to the overall airway resistance, early changes are small and may be undetectable by such tests. Currently, based on symptoms and patient history, different PFTs are indicated to confirm or rule out certain pathologies. For instance, a combination of spirometry, before and after a bronchodilator challenge, followed by a diffusing capacity test, could help differentiate between a case of COPD and bronchitis (West 1998).

1.2.3 Airway remodelling

Both asthma and COPD have now been shown to be associated with irreversible changes in airway structure known as airway remodelling (McParland, Macklem et al. 2003). Airway remodelling is defined as changes in the composition, content and organisation of the cellular and molecular constituents of the airway wall.

To date, the little that is known about the pattern of these changes has been detected and quantified using histological examination. Airway remodelling has been documented not only in the large but also in small asthmatic airways (James, Maxwell et al. 2002). The structural changes that have been documented in asthmatic airways include increased smooth muscle mass (Carroll, Elliot et al. 1993) and increased airway vascularity in the form of increased size of airway wall vessels and angiogenesis (Tanaka, Yamada et al. 2003). Evidence suggests that airway restructuring occurs early and is likely to be involved in the development and progression of asthma. Such studies require access to surgical or autopsy samples of the airways and are necessarily cross-sectional in design.

Noninvasive methods are required to further investigate the pathogenesis of airway wall remodelling, to assess changes over time, and to allow the assessment of new therapeutic interventions designed to attenuate or reverse these structural changes. Therefore, the development and application of relatively simple and safe methods for

assessing markers of inflammation and alterations in the airways are vital, especially for children (Djukanovic and Djukanovic 2002).

Although results from PFTs have been used to represent airway remodelling, they have limited use since they are affected by concomitant disease or medication and in any case provide only a global measure of lung function (Niimi, Matsumoto et al. 2004).

Technical advances in computed tomography (CT) allow an assessment of airway wall thickness and cross-sectional area *in vivo* that may be soon comparable to histological examination. However, the information that can be currently obtained from CT is currently less detailed than that obtained from histological examination (Bergeron, Tulic et al. 2007). CT cannot distinguish which components of the airway wall are thickened, for example. Despite this limitation, the ability to measure multiple airways relatively, noninvasively and repeatedly offers major potential advantages.

1.3 X-ray imaging techniques

X-ray imaging is one of the fastest and easiest ways for a physician to view the internal organs and structures of the body. Two-dimensional (2-D) radiography has been available for over 100 years (Kraft and Finby 1980) and is used for a wide range of clinical applications, including but not limited to, assessing skeletal trauma (Cooper and Little 1979), the gastro-intestinal system, mammography, and the thoracic cavity including the lungs and heart.

Radiography is by far the most commonly performed diagnostic X-ray examination, accounting for approximately half of all X-ray procedures obtained in medical institutions. The number of chest X-rays estimated from surveys taken in the U.S., Europe, and Japan is in the range of 200 to 330 per thousand of population per year. As the combined population of these areas is around 760 million, and using the average figure of 265 X-rays per thousand population, this equates to over 200 million chest X-rays taken in these geographic areas per year, or approximately 550,000 chest X-rays each day of the year (Fatz 2004).

1.3.1 X-ray computed tomography

Developed in the 1970s, computed tomography (CT) is a relatively new technique (Hounsfield 1973) for the nondestructive visualisation of the internal structure of objects. CT, like radiography, is based on the attenuation of X-rays with matter producing grayscale images corresponding to the material's X-ray linear attenuation

coefficient, which is primarily a function of density and atomic number. However, there are several advantages that CT has over traditional 2-D medical radiography.

First, CT completely eliminates the superimposition of images of structures outside the area of interest. It is impossible to display within the framework of a conventional 2-D X-ray radiogram all the information contained in the three-dimensional (3-D) scene under view. Objects situated in depth, that is, in the third dimension, superimpose, causing confusion to the viewer.

Secondly, conventional X-rays cannot distinguish between soft tissues. In general, a radiogram differentiates only between bone and air, as in the lungs. Variations in soft tissues such as the liver and pancreas are not discernible at all and certain other organs may be rendered visible only through the use of radio-opaque dyes. Because of the inherent high-contrast resolution of CT, differences between tissues that differ in physical density by less than 1 per cent can be distinguished.

Thirdly, with CT, it is possible to measure the separate densities of the individual substances through which the X-ray has passed. This is because CT uses radiographic images of the object collected from different angles and a back-projection algorithm (Cormack 1963) to reconstruct virtual 'slices' through the object. Individual CT images are sometimes referred to as 'slices' because they correspond to what would be observed if an object were sliced open along the scan plane. Consecutive slices can be reconstructed to create a 3-D volumetric data set, overcoming the main disadvantage of radiography, that is, the superposition of the body's different internal structures in one image, which complicates visualisation and quantification. This allows data from a single CT imaging procedure to be viewed as images in the axial, coronal, or sagittal planes, depending on the diagnostic task required.

These advantages have become more pronounced since the technique was first developed. First generation CT systems, which used a single X-ray beam and a single detector element to acquire the X-ray projection data necessary for image reconstruction, quickly evolved into a third generation system, using a fan-shaped X-ray beam combined with a rotating X-ray tube and detector. With the development of helical CT systems in the late 1980s (Mori 1986), large sections of anatomy could be scanned quickly using linear, continuous table motion.

Density is measured in Hounsfield Units (HU), where water is arbitrarily set to +1000, and a range of density values can be measured from air at 0, to dense bone at +2000. HU is related to density by the following formula:

$$Density\ (g/cm^3) = \frac{HU + 1000}{1000} \quad \textbf{(1.1)}$$

Figure 1.3 shows the range of density values given to a variety of substances.

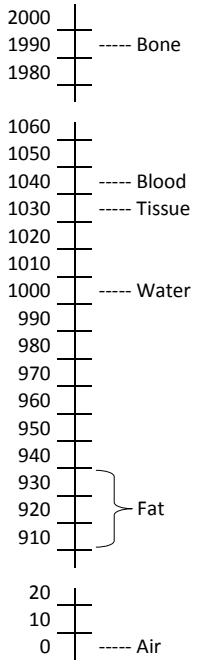

Figure 1.3: Typical tissue densities found in HRCT data

Adapted from http://nobelprize.org/nobel_prizes/medicine/laureates/1979/hounsfield-lecture.pdf
expressed in Hounsfield units (HU+1000)

The fundamental CT data unit is the voxel, a volume element on a regular grid in 3-D space, which corresponds to the volume bounded by the edges of a pixel and the thickness of the image slice. The CT value of a voxel is ideally a function of the attenuation coefficient of the material enclosed within it, although unavoidable blurring causes surrounding material to also have an influence on the CT value.

CT has become an important tool in medical imaging supplementing radiography and medical ultrasonography. Although it is still quite expensive, it is the gold standard in the diagnosis of a large number of different disease entities. With several key technological developments (Walter, De Man et al. 2004), it has more recently begun to be used for preventive medicine or screening for disease, for example colonography for patients with a high risk of colon cancer. Although a number of institutions offer full-body scans for the general population, this practice remains controversial due to its lack of proven benefit, cost, radiation exposure, and the risk of finding 'incidental' abnormalities that may trigger additional investigations (Maher, Kalra et al. 2004). The greatly increased availability of CT, together with its value for an increasing number of conditions, has been responsible for a large rise in popularity. So large has been this rise that, in the most recent comprehensive UK survey, while CT scans constituted 7 per cent of all radiologic examinations they contributed 47 per cent of the total collective dose from medical X-ray examinations in 2000–01 (Hart and Wall 2004).

1.3.2 High resolution X-ray computed tomography

High resolution computed tomography (HRCT) is a specialised CT protocol where imaging parameters are chosen to maximise spatial resolution in the lungs. A high-spatial frequency reconstruction algorithm is used and field of view is minimised, to maximise the resolution of each voxel. Other scan factors (for example, focal spot) may be optimised for increased resolution at the expense of scan speed.

With conventional lung CT, in order to cover the chest in a single breath-hold, it was necessary to use thick sections (10–20mm) in order to ensure contiguous coverage. With HRCT a narrow slice thickness is used (usually 1–2mm) but these slices are spaced 10–40mm apart. The result is a few images which are representative of the lungs in general, but which cover only approximately one-tenth of the lungs.

HRCT can depict the fine structures of pulmonary parenchyma not normally visible on conventional CT or radiograms and is therefore useful for evaluating both acute and chronic changes associated with diffuse infiltrative lung diseases (Nakata, Kimoto et al. 1985; Corcoran, Renner et al. 1992). Direct measurements of airway structures can be made from HRCT image data making it useful for studying asthma (Brown 2008; Carroll 2008), cystic fibrosis (Martinez, Llapur et al. 2005) and COPD (Camiciottoli, Bartolucci et al. 2006). HRCT may be diagnostic for conditions such as emphysema (Gevenois, De Vuyst et al. 1996) and bronchiectasis (Dodd and Muller 2006). Where HRCT is unable to reach a definitive diagnosis, it is able to provide information on the pattern and distribution of the abnormality, so can allow planning of a biopsy which may provide the final diagnosis. In the United States in 1999 more than 62 million CT scans were ordered (Brenner, Hall et al. 2007) of which 31 per cent were used for lung HRCTs.

Initially, HRCT was developed using relatively slow CT scanners that did not make use of multi-detector technology. The parameters of scan duration, z-axis resolution and coverage were interdependent. Recently introduced multi-detector CT scanners are able to overcome this interdependence and are capable of imaging at full resolution yet retain very fast coverage. Acquisition time of HRCT with multi-detector CT is so short that whole-lung HRCT can be performed in one breath-hold. These modern CT scanners now provide slice thicknesses less than 1 mm, so a CT data set covering the chest may contain more than 300 slices. Manual analysis of these images is not only time-consuming, tedious and error-prone due to the increasing number of scans being made, it is increasingly becoming impractical (Aykac, Hoffman et al. 2003).

State-of-the-art medical CT scanners allow up to 0.25mm in-plane and 0.5mm through-plane resolution (Wang, Zhao et al. 2005). However, this level of resolution has been far superseded by parallel technological advances which have extended the resolution capability well below the mm resolution limits of clinical systems.

1.3.3 Micro X-ray computed tomography

Technological advances in the 1980s enabled the construction of microfocus X-ray tubes. Using these tubes, micro-tomography (micro-CT) systems could be developed. Micro-CT instruments are based on the same principles as other CTs, but have the advantage of an enhanced resolution up to 0.001 mm. To create a micro-CT image, a series of projection images are taken around the animal or sample in equally spaced angular intervals (Holdsworth and Thornton, 2002). This collection of images is reconstructed with a backprojection algorithm to produce a stack of 2-D cross-sectional images with each pixel corresponding to a spatial location within the sample (Bushberg et al., 1994).

In contrast to HRCT, because the slice thickness of each image in the stack is equal to the pixel size, the image set is a true 3-D volumetric data set with isotropic voxels. This allows for reslicing the image data to provide the orthogonal or oblique views and visualisation of the spatial orientation of tissues with no loss of resolution within the sample (Ford, Thornton et al. 2003). However, due to the limitations of the sample chamber, the specimen examined must either be relatively small, such as a live rodent, or excised from biopsy material (Holdsworth and Thornton 2002).

Early investigations of micro-CT focused on the technical and methodological aspects, whereas more recent investigations have stressed the practical application aspects of this technology. Feldkamp *et al* (1989) established a micro-CT system to image a 3-D object at spatial resolution of 0.05mm. In the past decade, micro-CT has become a powerful technique in laboratory investigation as technical advances in computer speed and memory size and availability of megapixel charge-coupled device (CCD) detectors have enabled micro-CT systems to generate high-spatial-resolution images of small specimens (Langheinrich, Leithauser et al. 2004). High-resolution serial images of organ micro-architecture have been obtained for biomedical drug testing. Visualisation of a specimen can be obtained quickly and intact specimen analysis is non-destructive.

Micro-CT is currently used for studying the 3-D structure of a wide range of small objects in microscopic detail, such as the microstructure of coke (Jones, Reztsov et al. 2007) and receptor structures of the inner ear (Uzun, Curthoys et al. 2007) but its use in lung has only recently began to be explored (Sera, Fujioka et al. 2003; Shofer, Badea et al. 2007). Micro-CT resolution is almost two orders of magnitude greater than HRCT, where resolution is at best 0.25mm. The resolution of micro-CT should allow airway measurements of similar or greater accuracy to morphometry (San Jose Estepar, Reilly et al. 2008), but in three dimensions, which would allow validation of segmentation algorithms used to measure airway dimensions *in vivo*.

1.3.4 CT artifacts

CT images are inherently more prone to artifacts than conventional radiographs because the image is reconstructed from something in the order of a million independent detector measurements (Voros and Voros 2009).

There are also several known artifacts in CT imaging, each of which can interfere with quantitative analysis, and therefore some of the more important ones are briefly discussed below.

Beam hardening

The phenomenon referred to as ”beam-hardening” results from using polychromatic radiation which is attenuated by the object being scanned in a non-linear way. X-ray attenuation processes in matter are energy dependent. The lower energy X-rays in the beams are more strongly absorbed than the higher energy X-rays such that the energy spectrum of the beam changes as it passes through the object. The emerging beam contains a higher proportion of high-energy X-rays. Hence, the attenuation of an homogeneous object is not strictly proportional to its thickness and the standard reconstruction techniques, which assume a monochromatic source, produce some distortions (Figure 1.4).

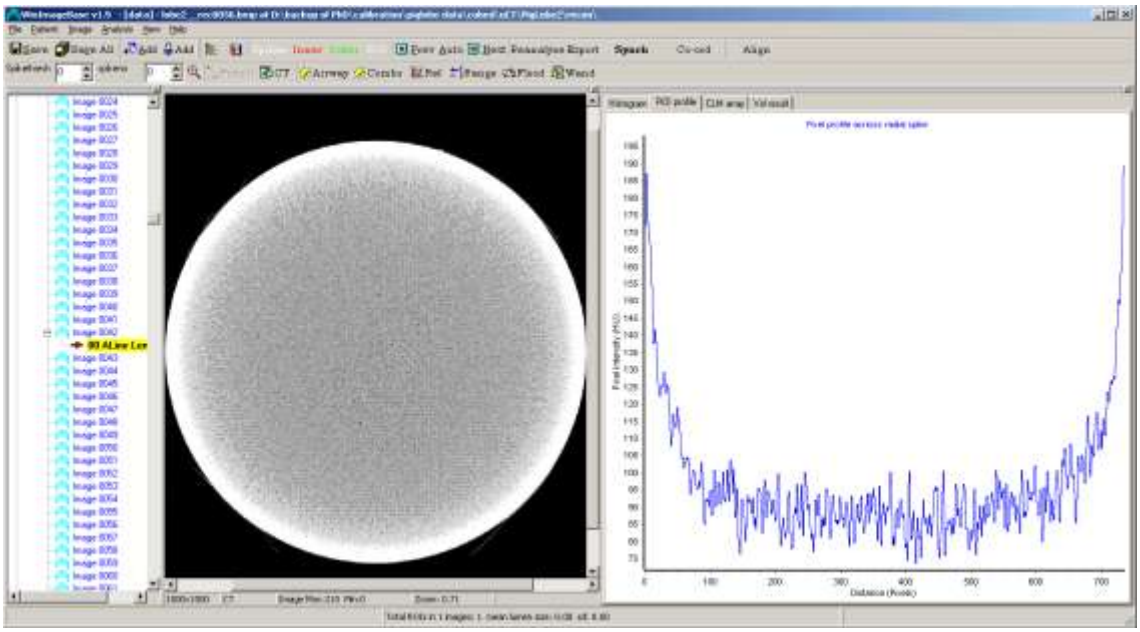

Figure 1.4: Example of beam hardening across a micro-CT image of a uniform air phantom

Pixel intensity profile can be seen on the right corresponding to the pixel profile across the image. Notice the 'cupped appearance' due to more attenuation in the centre of the object than around the edge.

Many methods are used to minimise the effects of beam hardening. These include:

- Filtration: a flat piece of attenuating material such as aluminium or copper 'pre-hardens' the beam by filtering out the lower energy components before it passes through the patient. An additional 'bowtie' filter further hardens the edges of the beam which will pass through the thinner parts of the patient.
- Calibration corrections: some manufacturers provide phantoms in a range of sizes which allow the detectors to be calibrated with compensation tailored for the beam hardening effects of different parts of the patient. This provides an effective means of minimising cupping artifacts.
- Beam hardening correction software: an iterative correction algorithm may be automatically applied when images of bony regions are being reconstructed. This helps minimise blurring of the bone/soft tissue interface in brain scans and also reduces the appearance of dark bands in non-homogeneous cross sections.

Ring artifact

Ring artifacts in reconstructed images appear as sharp rings with a width of one pixel. They arise as a result of badly calibrated or defective detector elements , for example, from dead pixels in a Charged Coupled Detector (CCD). Such detector elements have non-linear responses to incoming intensity. The arrow appearance of this common mechanical artifact has facilitated the development of algorithms to effectively remove it with negligible loss of information (Raven 1998).

Aliasing

Aliasing appears as dark lines or 'streaks' which radiate away from sharp corners. It is usually associated with images of extremely dense objects, such as bone or metal because it is impossible for the scanner to 'sample' or take enough projections of the object. It can also occur when an insufficient X-ray tube current is selected, and insufficient penetration of the X-ray occurs. It is also closely tied to motion during a scan. Although rarely seen in clinical images, it commonly occurs in test objects such as phantoms. Algorithms to counter the effects of aliasing by locally reconstructing the image from truncated data have been effectively demonstrated (Wang, Vannier et al. 1999).

Motion artifact

Patient motion can cause misregistration artifacts, which appear as blurring or streaking in the reconstructed image. Steps can be taken to prevent voluntary motion, but some involuntary motion may be unavoidable during body scanning. There are, however, special features on some scanners designed to minimise the resulting artifacts:

- use of as short a scan time as possible to help minimise artifacts when scanning regions prone to movement
- breath-holds for the duration of the scan to prevent respiratory motion
- cyclical scanning at a single moment of the movement's phase, for instance cardiac gating to avoid cardiac motion and respiratory gating to avoid breathing motion (Farncombe 2008).

Software corrections can also be applied. The maximum discrepancy in detector readings occurs between views obtained towards the beginning and end of a scan. Some scanners have special software corrections which apply reduced weighting to these views to suppress their contribution to the final image.

Volume averaging

Volume averaging appears as 'blurring' over sharp edges. Due to a mismatch between the spatial resolution of CT and the structural dimensions of the materials being measured each voxel is large enough to contain more than one type of material. In this case, the resulting voxel density is made up of the relative contributions of the density of each of the materials in space occupied by that voxel.

For instance, if a voxel contains a small amount of high-density material (for example, bone) and a larger amount of lower density (for example, cartilage), then the resultant voxel density will be averaged somewhere between the two densities. The higher the amount of the low-density material, the lower the resultant voxel density will become. The main consequence is that the distinction in gray levels between materials is blurred and boundaries between them are not well defined (Figure 1.5).

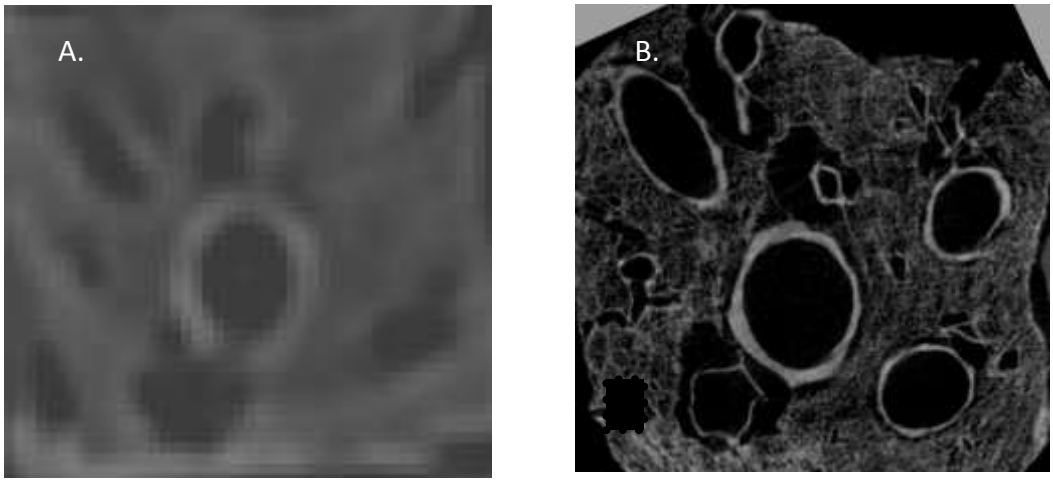

Figure 1.5: Thick slice versus thin slice CT images of pig lung tissue

Volume averaging artifacts are negligible only if the spatial resolution of the CT scanner is much higher than the structural dimensions of the object being measured. For example, with a spatial resolution of 0.05mm, only the centre slice of a 0.15mm

trabecula tissue reaches the correct density (Cowin 2001). Even though the problem of volume averaging is omnipresent, it particularly affects the HRCT modality, where the voxel size in the *z*-axis is often much larger than that in the *x*- *or y*-axes. Volume averaging artifacts are particularly prominent in images of any part of the body where the anatomy is changing rapidly in the *z*-direction, such as in the posterior fossa.

Segmentation algorithms that rely on density levels are known to be adversely affected by volume averaging effects (Berry 2008). Volume averaging can be partially reduced by using a thin acquisition slice, but unfortunately this increases the noise in the image. To reduce image noise, thicker slices can be reconstructed from the acquired data. Because of the non-linear nature of volume averaging it has been suggested that the use of adaptive interpolation might reduce the effects of volume averaging (Wang and Vannier 1994; Chiverton and Wells 2004).

1.4 HRCT airway segmentation algorithms

HRCT airway segmentation algorithms seek to provide an objective and repeatable measures of the airway lumen and wall dimensions, such as those shown in Figure 1.6. Recent interest has arisen from technical improvements in HRCT which have made it theoretically possible to examine small airways, and because qualitative and semi-quantitative measures have been shown to be open to subjective bias (King, Muller et al. 2000).

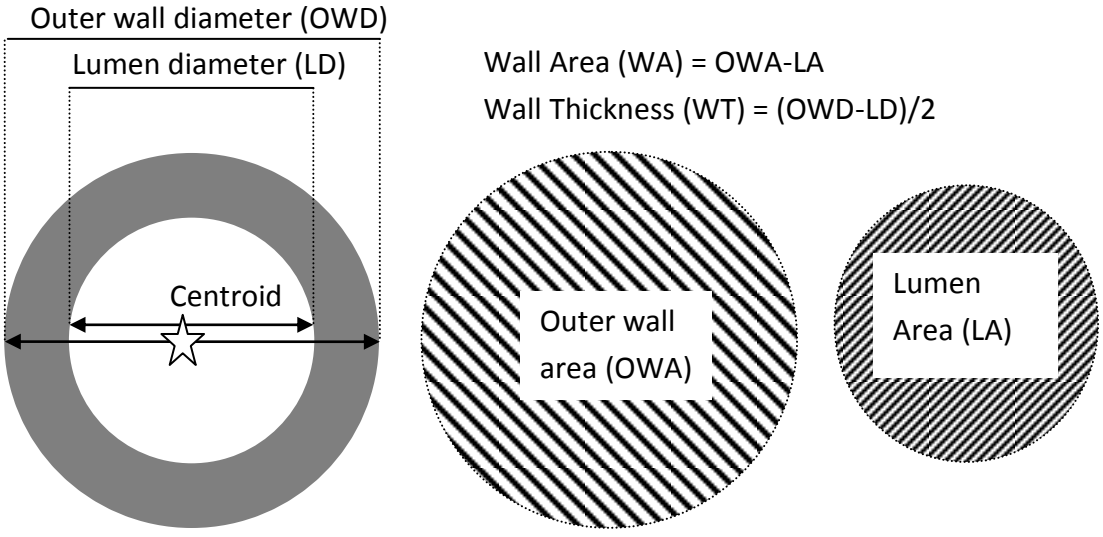

Figure 1.6: Schematic of HRCT calculated airway dimensions most commonly reported

Dimensions are: airway lumen area and airway wall area, outer wall area, outer wall and lumen diameters, wall thickness, airway perimeter, percentage wall area and square root of wall area. The centroid position can be used to calculate and correct for the angle at which the airway is observed.

1.4.1 Algorithm types

Many algorithms have been proposed and used for the measurement of airway size from HRCT images. Initial studies relied on manual tracing of the airway images either on film (Webb, Gamsu et al. 1984), computer screen (Seneterre, Paganin et al. 1994) or via projected image (McNamara, Muller et al. 1992) by the investigators. These techniques are time consuming and error-prone. For example, (King, Muller et al. 1999) noted that error was introduced from the adjustment of window viewing-brightness and contrast for better visualisation. This variation in observer interpretation has been stated as being the weakest area of clinical imaging (Brealey 2001).

In an attempt to increase the precision and accuracy of airway measurement, computer-based methods have been devised to measure airway lumens and walls.

A simple and common computer-based method for lumen segmentation is the seeded region-growing algorithm, where the algorithm is terminated based on a Hounsfield unit (HU) threshold cut-off value. The main problem with this type of algorithm is how to determine the value for the threshold. Some researchers (McNitt-Gray, Goldin et al. 1997) have reported that the airway lumen area could be accurately measured by including all pixels beyond a threshold cut-off of -500 HU, whereas others (King, Muller et al. 2000) contend that a threshold of -577 HU produced the least error. Still others have found the threshold to be dependent on the size of the airway being measured (Nakano, Whittall et al. 2002).

The difficulty in choosing a suitable threshold led to the development methods to circumvent the problem. One such method was introduced by (Mori, Hasegawa et al. 1996) is aptly called “explosion controlled region growing”. This method iteratively increases the Hounsfield Unit threshold value used to define lumen in adjacent voxels until the total number of growing voxels increases too much in one single evolution step. Only adjacent voxels below this CT attenuation value will therefore be defined as lumen. Other types of algorithms have been developed to overcome this problem, including score-guided erosion (King, Muller et al. 2000), Gaussian fit (Berger, Perot et al. 2005, Venkatraman, Raman et al. 2006), and fuzzy connectivity (Tschirren, Hoffman et al. 2005).

The most common successful approach has been the ‘‘full-width-at-half-maximum’’ (half-max) edge-detection method. The user creates a pixel profile allowing the computer to set the threshold at exactly halfway between the wall and the lumen density (Figure 1.7).

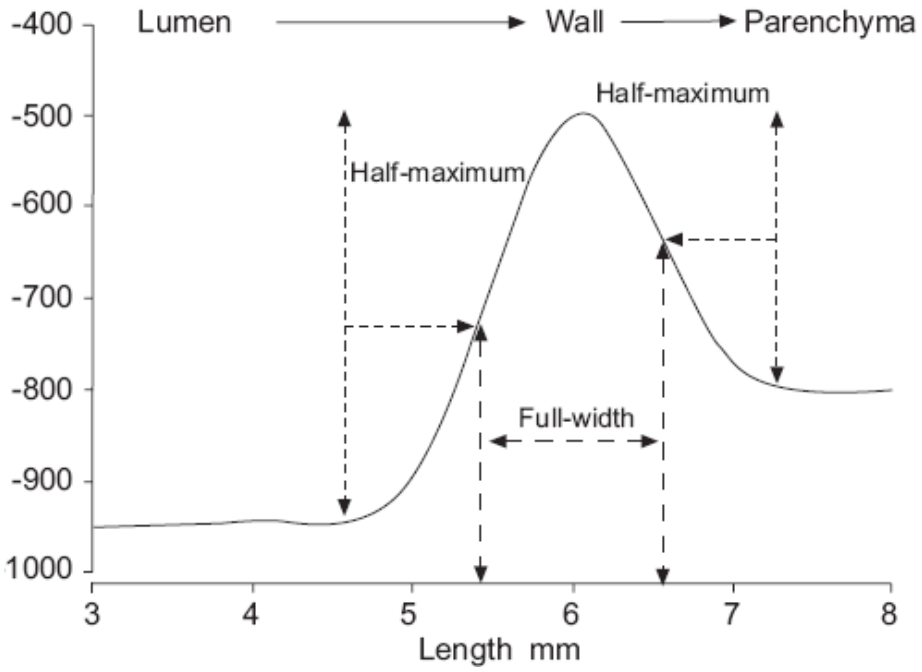

Figure 1.7: Airway measurement using the full-width at half-maximum algorithm

A representative X-ray attenuation curve for a ray that passes from the lumen through the airway wall and into the parenchyma is shown. The thickness of the wall is determined using the half-maximum point of the change in X-ray attenuation as the ray enters and exits the wall. From (de Jong, Muller et al. 2005).

This method of choosing a threshold is more objective, but it does not overcome inherent inhomogeneity found in airway walls in HRCT images, so that a different threshold must be defined for different parts of the airway wall.

The ray-casting algorithm was developed to address this lack of airway wall homogeneity. The algorithm requires that a seed point be placed in the lumen and the X-ray attenuation values be measured along rays cast from this point outward toward the airway wall in all directions. As a ray enters the wall, the attenuation will initially increase, and then decrease as it passes into the lung parenchyma. The distance between the point at which the attenuation is halfway to the maximum on the lumen side and the point halfway to the local minimum on the parenchymal side is considered to be the wall thickness.

Although the more sophisticated ray-casting algorithm does provide a standardised and objective measurement, it was also found to have limitations. When HRCT algorithm measurements were compared with measurements from phantoms and anatomical specimens, the algorithm consistently overestimated WA and underestimated LA (Nakano, Whittall et al. 2002). These systematic errors were thought to be due to a combination of factors including: the spatial resolution of the HRCT scanner; the angle of orientation of the airway within the HRCT slice; the point-spread function; the reconstruction algorithm used; the algorithm used; and inability to visualise the folding of the epithelium.

1.4.2 Validation phantoms

Before HRCT segmentation algorithms can be accepted into clinical practice, validation to establish the accuracy and precision of these methods is crucial (San Jose Estepar, Reilly et al. 2008). In previous studies, a number of validation methods have been proposed for HRCT segmentation algorithms (summarised in Table 1.1). These validation methods are designed to provide a comparison between the "airway" measurement obtained from HRCT and the true airway size.

TABLE 1.1: ALGORITHMS AND VALIDATION USED FOR HRCT AIRWAY MEASUREMENTS

Reported by	Segmentation algorithm used	Validation used	Structure measured
(Tschirren, Hoffman et al. 2004)	Fuzzy connectivity region growing	Human expert	LA
(Reinhardt, D'Souza et al. 1997)	Ray-casting	2-D simulated data plexiglass phantom	LA/OWA
(Palagyi 2003) **(Palagyi, Tschirren et al. 2006)**	Skeletonisation	3-D simulated data plastic phantom	LA
(Wood, Zerhouni et al. 1995)	Region-growing	Plexiglass phantom	LA
(King, Muller et al. 2000)	Region-growing Score-guided erosion	Plastic phantom Pig lung	LA/OWA
(Ohara, Hirai et al. 2006)	Ray-casting	Plastic phantom	LA/OWA
(Venkatraman, Raman et al. 2006)	Gaussian fit	None	LA/OWA
(Saba, Hoffman et al. 2003)	Ray-casting elliptical model	Plexiglass phantom	LA/OWA
(Aykac, Hoffman et al. 2003)	Region-growing	Human expert	LA
(Nakano, Whittall et al. 2002) **(Nakano, Muller et al. 2002)**	Ray-casting	Morphometry	LA/OWA
(Berger, Perot et al. 2005)	Gaussian fit	Silicone tubes Sheep lung	LA/OWA
(Dame Carroll, Chandra et al. 2006)	Ray-casting	Plastic tubes Pig lung	LA/OWA
(Sera, Fujioka et al. 2003)	Skeletonisation	Micro-CT	LA
(McNitt-Gray, Goldin et al. 1997)	Contour following	Low density material with water filled holes	LA
(McNamara, Muller et al. 1992)	Manual	Sweet potato embedded in sponge	LD
(Amirav, Kramer et al. 1993; Brown, Scichilone et al. 2001; Brown, Kaczka et al. 2008)	Ray-casting	Plexiglass disk with holes	LA
(Nakano, Muro et al. 2000)	Ray-casting	Polystyrene	LA/WT
(Matsuoka, Kurihara et al. 2005)	Thresholding	Polystyrene	LA/WT
(Webb, Gamsu et al. 1984)	Thresholding	Lucite tubes	LD
(Wiemker, Blaffert et al. 2004)	Region growing	None	LA/OWA

The most popular validation method uses airway phantoms of known dimensions constructed from non-animal materials such as plexiglass and sweet potatoes (Amirav, Kramer et al. 1993; McNitt-Gray, Goldin et al. 1997; King, Muller et al. 2000) to simulate transverse sections of airways found in the lung. The more advanced versions of these phantoms simulated airways surrounded by parenchymal tissue by using hollow air-filled, high-density tubing embedded in a lower-density material.

Other HRCT validation studies of airways have used explanted animal lungs as gold standards, particularly porcine lungs that were either wet-fixed in formalin (King, Muller et al. 2000) or inflation-fixed in formalin vapour (Dame Carroll, Chandra et al. 2006). Explanted lung preparations have some advantages for validation because they more closely approximate the range of tissue densities and dimensions, and the complex structure of *in vivo* lung tissue.

However, gold standard measurements made from planimetric measurements of a cut surface of the phantom or explant assume that dimensions would be completely uniform along the length of the airway phantom and that the orientation in the z-axis of the scanning plane could be accurately controlled. Hence a proportion of the error estimates of segmentation algorithms derived from these excised lung and phantom based studies is due to inaccuracies of the 'gold standard' measurements made by planimetry (Dame Carroll, Chandra et al. 2006).

Orientation of airways

Webb and coworkers (Webb, Gamsu et al. 1984) were the first investigators who reported airway lumen measurements from HRCT when the airways were imaged at angles other that 90 degrees. Their data showed that airway angle, airway size and slice thickness interact to produce measurement error.

Other researchers have also established that the magnitude of the measurement error depended on how acutely the airways were angled and it was thought that this error was due to volume averaging (King, Muller et al. 1999; de Jong, Nakano et al. 2005). This finding led most researchers to restrict HRCT airway measurement to airways that were scanned in cross-section (that is, orthogonal), ruling out analysis in the majority of airways. Few algorithms have attempted to compensate for the angle. King and colleagues (2000) defined the angle of deviation of each airway from the perpendicular using the centroid of the same airway the two sections on each side of the section on which the measurements are made. Saba and colleagues (2003) developed an alternate technique for measuring airways that were not cut in cross-section. This fitted an ellipse to the airway lumen and wall, and may correct errors in measurement of obliquely cut airways.

These techniques claim to be more accurate than the more commonly used techniques, but have not been generally applied.

While HRCT airway segmentation algorithms have been in development for over a decade, judging their relative accuracy and precision is complicated by a lag in the development of standardised validation protocols. The lag may result from a lack of common data sets with which to compare algorithms (San Jose Estepar, Reilly et al. 2008); difficulty in defining performance metrics and statistics (Brealey 2001); and the difficulty in establishing a true airway segmentation (Udupa, Leblanc et al. 2006).

1.5 Aims and scope of thesis

Thesis statement

This thesis contends that HRCT airway segmentation algorithms can be validated using a combination of simulated, artificial and animal phantoms measured using micro-CT and that the validated algorithm can be applied in a clinical setting to provide improved accuracy and precision of airway measurement.

Aims

To support the achievement of this goal, the following objectives were proposed for this study:

- develop HRCT airway segmentation algorithms that are easily applied and which are anchored in current best practice
- implement prototype computer software that incorporates the algorithms to make quantitative measurements of airway lumen and walls from HRCT images of the lungs
- select the most suitable algorithm to optimise its performance in terms of speed and robustness
- develop a validation protocol for HRCT airway segmentation algorithms using multi-modality data sets of simulated airways, phantom standards and animal models measured with micro-CT and to use this to test the accuracy and precision of the most suitable algorithm
- determine the effects of airway orientation and volume averaging found in HRCT data
- demonstrate the usefulness of the algorithms by examining the relationships between lung structure and pathophysiology in clinical data.

Structure

This thesis is divided into eight chapters:

Chapter 1 provides background information to HRCT airway segmentation algorithms, including previous work done in the area as well as the significance of the proposed research, its hypothesis and aims. This chapter introduces lung anatomy and diseases, lung function testing and CT-based imaging techniques to provide a broad appreciation of the current challenges in making direct airway measurement.

Chapter 2 describes the algorithms that were tested and their results in terms of their speed and robustness in the context of noisy HRCT data. The algorithms are compared to identify a fast, robust and relatively parameter-free algorithm (the CL algorithm) for the measurement of airway lumen and walls.

Chapter 3 describes the construction and function of *winImageBase*, a Microsoft Windows application developed around the algorithms which enabled practitioners from any field to make airway measurements with the minimum of effort.

Chapter 4 develops a 3-D simulated model data set to eliminate the experimental and biological induced variance found in clinical data. The model contains different sized simulated airways and allowed testing of the effect of a number of parameters on the performance of the CL algorithm. The parameters tested included edge-detection mechanism, number of rays, and the effect of various degrees of interpolation. The aim was to validate the algorithm against computer-generated experimental data, thereby establishing the optimal parameter selection.

Chapter 5 tests the performance of the CL algorithm on simulated 3-D data with volume averaging at different airway sizes and orientations. The goal of this study was to model volume averaging effects, derive a method for correction and demonstrate its use.

Chapter 6 compares CL algorithm measurements from HRCT data in an artificial and tissue phantoms where airway dimensions have been established using light microscopy and micro-CT. The goal was to identify whether the performance of the algorithm in HRCT data had been improved by optimal parameter selection and volume averaging correction.

Chapter 7 considers clinical HRCT data, where the effect of mannitol on airway dimensions in patients with bronchiectasis is compared to pulmonary function testing.

Chapter 8 draws conclusions from the thesis.

CHAPTER 2

Algorithm development

Diagnosis of lung diseases using HRCT requires objective airway measurement, which can only be achieved using computer-based segmentation algorithms. In this chapter the selection and development of an optimal HRCT segmentation algorithm is described. The *Monitoring Devices* program within the Woolcock Institute of Medical Research needed the algorithm for fast, objective and repeatable measurement of airway lumen and walls from HRCT images. The algorithm had to be robust to the typical problems occurring in HRCT images, such variations in intensity, size and shape of the airways. To increase objectivity, user initialisation needed to be minimal, but the user was to be given the opportunity to review results and intervene if necessary.

Algorithm development proceeded by testing candidate algorithms within a software support platform (*winImageBase*, described in Chapter 3). As part of the development process, each iteration of the algorithm was qualitatively evaluated for its robustness in the context of randomly selected patient HRCT data, with the aim of defining a reliable and efficient algorithm requiring as few settings as possible.

Since the clinical applicability of the algorithm is largely dependent on the time needed to obtain the result this criterion was also examined. Development here proceeded empirically in consultation with the team from the *Monitoring Devices* program, adapting the algorithms to address perceived problems as they appeared.

2.1 Methods

Three algorithms were developed in the *C++* programming language based on a literature review of the current HRCT airway segmentation techniques currently employed to obtain quantitative measures of airway dimensions (Section 1.4.1). The algorithms all relied on intensity values as a means of discriminating between the lumen-wall boundary and the wall-parenchyma boundary. Each algorithm used a different mechanism to achieve segmentation:

- thresholding
- region-growing
- ray-casting and centre-likelihood

The theory underlying each algorithm's mechanism is now considered.

2.1.1 Thresholding

Thresholding is one of the simplest and fastest algorithms for image segmentation (Berry 2008). It involves choosing a range of pixel intensities that represent the object to be segmented. If the object of interest in an image is brighter than the background, individual pixels are marked as "object" pixels where their value is greater than a nominated threshold value, and as "background" pixels otherwise. For HRCT images, the threshold can be chosen from the Hounsfield Unit scale (Figure 1.3) or based on an analysis of the image histogram (Figure 2.1)

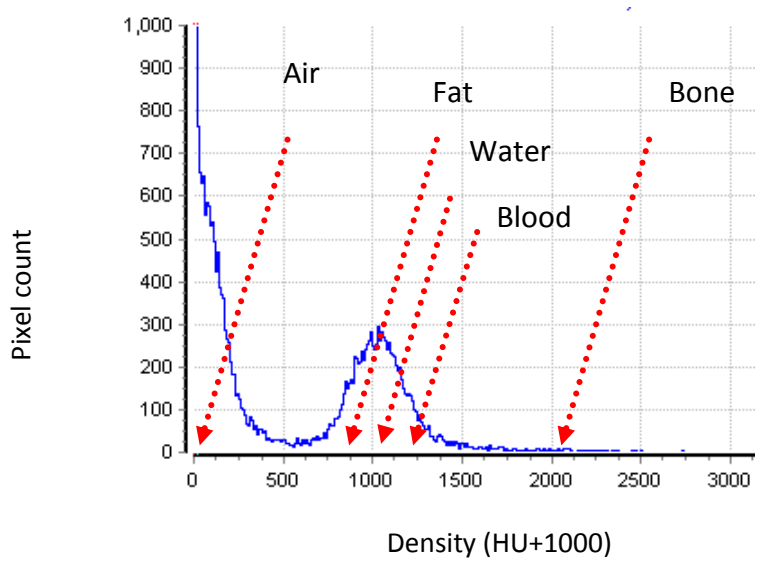

Figure 2.1: Typical histogram of pixels found in HRCT images of the lung

When 'thresholding' a greyscale image with a fixed threshold t, each pixel p is assigned to one of two classes, P0 or P1, depending on whether I(p) < t or I(p) ≥ t. Pixel counts (blue) with threshold (red arrow) to separate the partitions

Summation of the pixels in any one classification allows a simple calculation of the area taken up by that object. For instance setting the threshold as 2000 will allow the amount of bone in the image to be quantified.

Used in this way, thresholding is known as image binarisation. In Figure 2.2 a single threshold has been set at 500, which has allowed all objects with density greater than air to be quantified. If the object of interest had an intermediate density, two thresholds can be chosen. The use of multiple thresholds is often referred as density slicing.

Since the airway lumen contained air, a single threshold was used for this object. However, the airway wall had an intermediate density, so density slicing was applied in this instance.

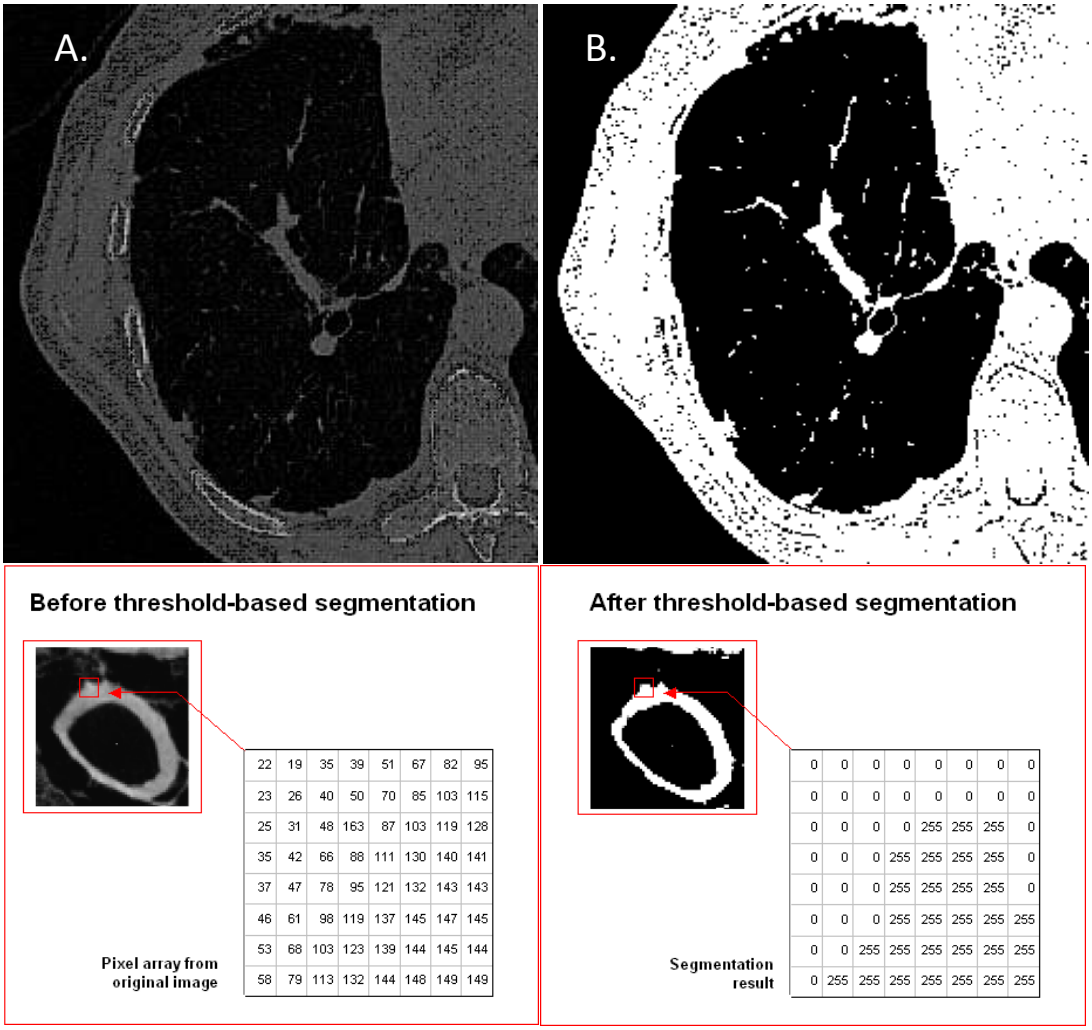

Figure 2.2: Illustration of image binarisation in an HRCT images of the lung

Full HRCT image (top) and single airway (bottom):
(A) original image of an airway with numerical representation of a small region on the wall edge.
(B) segmentation result with all values mapped to either 0 (background) or 255 (object).
Darker pixels are represented by lower values and lighter pixels are represented by higher value.

2.1.2 Region growing

The region-growing algorithm adds another level of complexity to the thresholding segmentation, partitioning the image into regions (Figure 2.3). The user defines a range of densities that represent the object of interest, and chooses a pixel that is known to be part of the region. The nearest neighbouring pixels to this 'seed pixel' are examined for their density to determine whether they should be added to the seed point or not. For every pixel that is added to the region, the process of examining the neighbouring pixels is repeated.

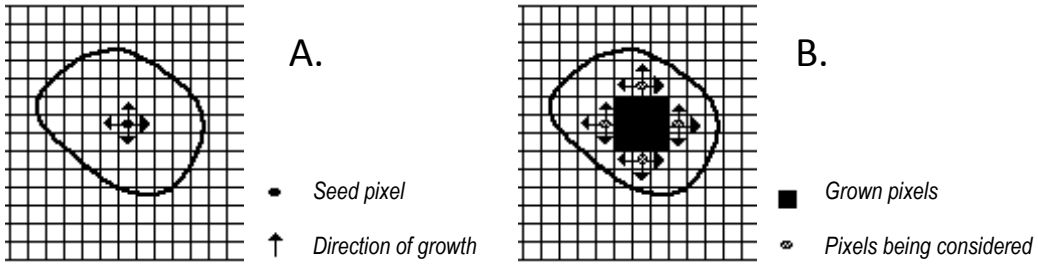

Figure 2.3: The region-growing algorithm process explained

Airway is superimposed on a pixel grid. (A) start of a growing region, (B) growing process after a few iterations

Many types of modification exist to the region growing method. The method tested during this study was to set a tolerance to the threshold, where any pixel value with density equal to the threshold ± tolerance is accepted as part of the region.

2.1.3 Ray casting and centre likelihood

The ray-casting and centre-likelihood (CL) algorithm was originally devised for delineation of blood vessels from 3-D angiographic images (Wink, Niessen et al. 2000).

This project adapted this algorithm for airway lumen measurement by adding:

- airway wall-parenchyma boundary measurement
- rules for handling airway merging and ray termination
- tracking using adaptive region of interest (ROI) and centroid displacement

In the next subsections the most important steps of the process are described.

Determination of the airway centroid

The CL algorithm is initiated by defining the search ROI around the outside of the airway as is shown in Figure 2.18. Identification of the airway's centroid (the geometric centre) relies on the CL algorithm being used at every pixel location in the ROI. At each pixel in the ROI, the CL algorithm casts a set number of equiangular rays from the pixel until they reach the edge of the ROI. The pixel intensity along each ray is used to create a pixel profile, which is used to identify the inner and outer airway walls using an edge detection technique, such as maximum rate of change in pixel intensity (Figure 2.5). This process is repeated at each pixel location to create a set of ray lengths. The opposing ray lengths are then divided and summed, and then divided by the total number of rays to give a probability (*p)* of this point being the centre where (0>p>100).

The percentage *p* calculation is shown as follows:

$$\text{Percentage } p = \frac{100}{n} \sum_{i=1}^{n} \frac{min\left(\left|\vec{r}1_{l_i}\right| \ , \ \left|\vec{r}2_{l_i}\right|\right)}{max\left(\left|\vec{r}1_{l_i}\right| \ , \ \left|\vec{r}2_{l_i}\right|\right)} \qquad \textbf{(2.1)}$$

where every pair of rays $\vec{r}1_{\mathrm{l_i}}$, $\vec{r}2_{\mathrm{l_i}}$ makes up a line and *n* is the number of lines.

Computation of the centre likelihood at every ROI location allows the creation of a CL map, corresponding to the probability of each pixel being the centroid (Figure 2.6). The pixel with the highest centre likelihood is taken to be the centroid of the airway.

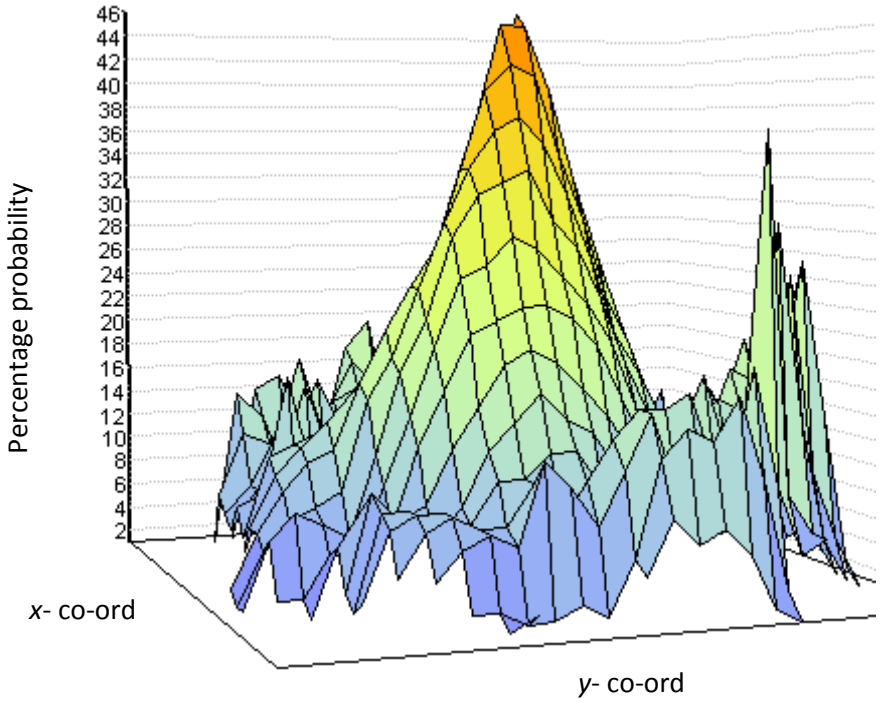

Figure 2.4: CL probability map surface for the ROI

Percentage probability against co-ordinates corresponding to the ROI as shown in Figure 2.18A

Identification of airway wall boundaries

To identify to airway walls a fixed number of equiangular rays are cast from the centroid pixel. A pixel profile is created from the intensity across the ray and an edge-detection technique such as maximum rate of change in pixel intensity is used to identify the point at which the ray crosses the wall. In Figure 2.5 the wall-parenchyma boundary is identified in a similar way to the lumen-wall boundary, by examining the pixel profile between the lumen-wall boundary and the ROI edge for the maximum negative pixel gradient.

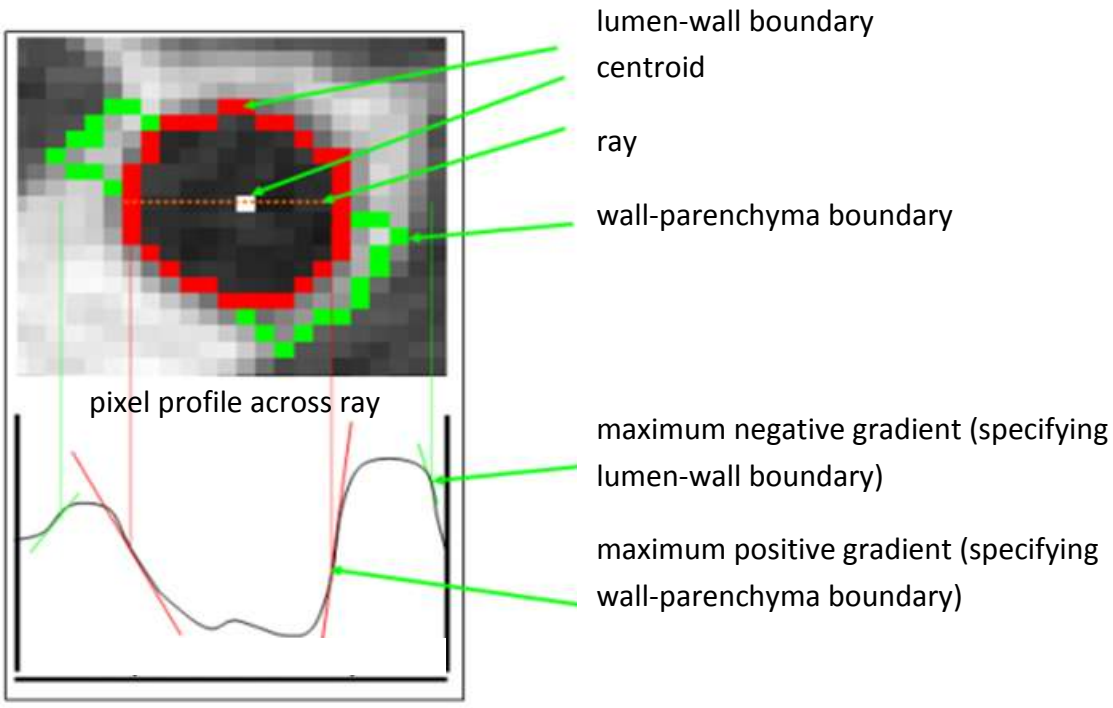

Figure 2.5: Boundary detection using pixel profile

Along the ray, the gradient is computed (top). In the pixel profile (bottom), the maximum positive gradient (red) determines lumen-wall boundary position and the maximum negative gradient (green) determines the wall-parenchyma boundary position.

As each ray is cast another point on the airway wall is identified (Figure 2.6A). This process is repeated and the points at which each ray traverses the wall becomes the vertices of the polygon used to outline the lumen-wall and wall-parenchyma boundaries (Figure 2.6B).

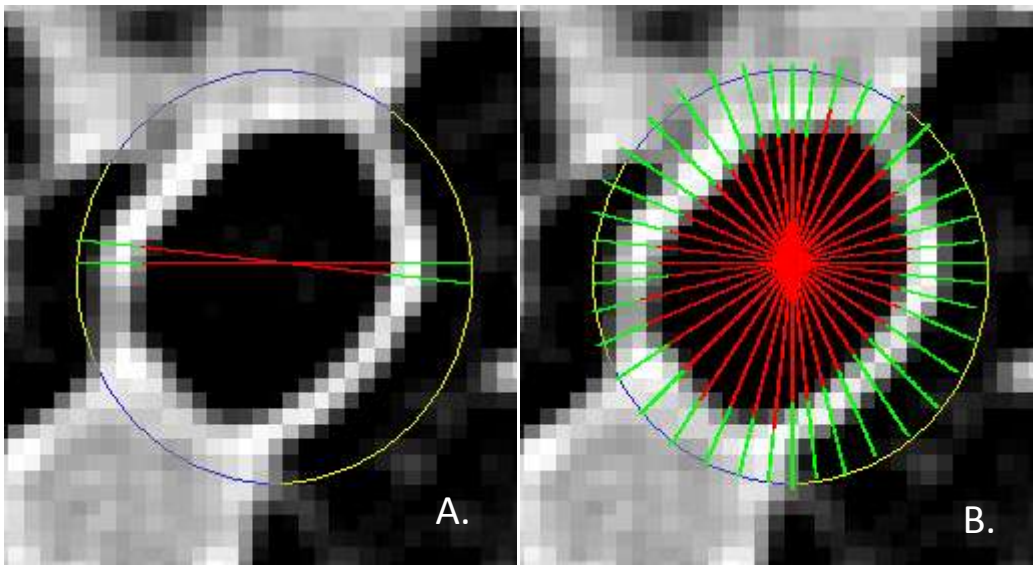

Figure 2.6: Screenshots of ray-casting from a central pixel to identify the airway wall

Rays from centroid to lumen-wall boundary, rays from lumen-wall boundary to ROI (yellow) shown in green:
(A) the fourth ray is cast at 40/360 degrees from the pixel to the ROI
(B) all rays have been cast. The ray endpoints are joined to define the walls.

Airway tracking

The CL algorithm formed a central part of the semi-automatic method for delineation of the airway tree implemented in *winImageBase*. A schematic description of this process is given in Figure 2.8. The process was initiated by user-defined seeding of the visible airways in one image. After the CL algorithm has segmented these airways, an interactive tracking process was initiated. At every iteration, each airway was extended into the next HRCT image. This was achieved using the shape and relative position of the airway and centroid in the previous image. In this image the candidate ROI was searched for the airway centroid, using the CL algorithm. If two or more airway lumens are found to overlap, then a new ROI is calculated by merging the ROIs from the overlapping airways.

During the process, the centroid, ROI, airway-lumen boundary and wall-parenchyma boundary are displayed. This enables the user to monitor the process and take control if needed.

2.1.4 Image selection

To test the robustness of the algorithms an HRCT image series was examined for case images containing airways of the size and orientation required to be measured. A single airway was identified and the airway tracked and measured through 43 images. An example image containing typical airways and surrounding structures is shown Figure 2.7.

Density values were obtained as HUs from the 12-bit image data stored within each HRCT dicom file.

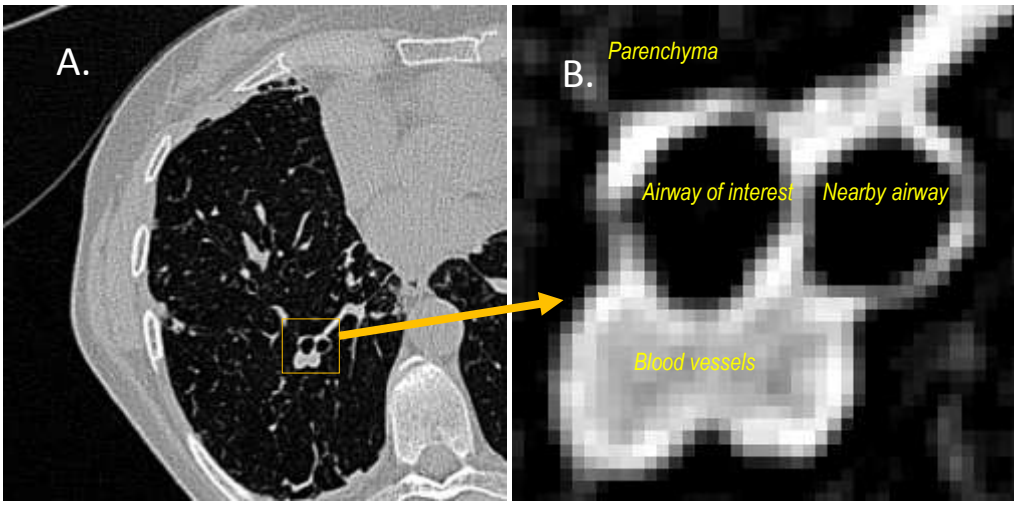

Figure 2.7: An example HRCT image used for testing

(A) original HRCT image, (B) zoomed to show two individual airways and surrounding structures

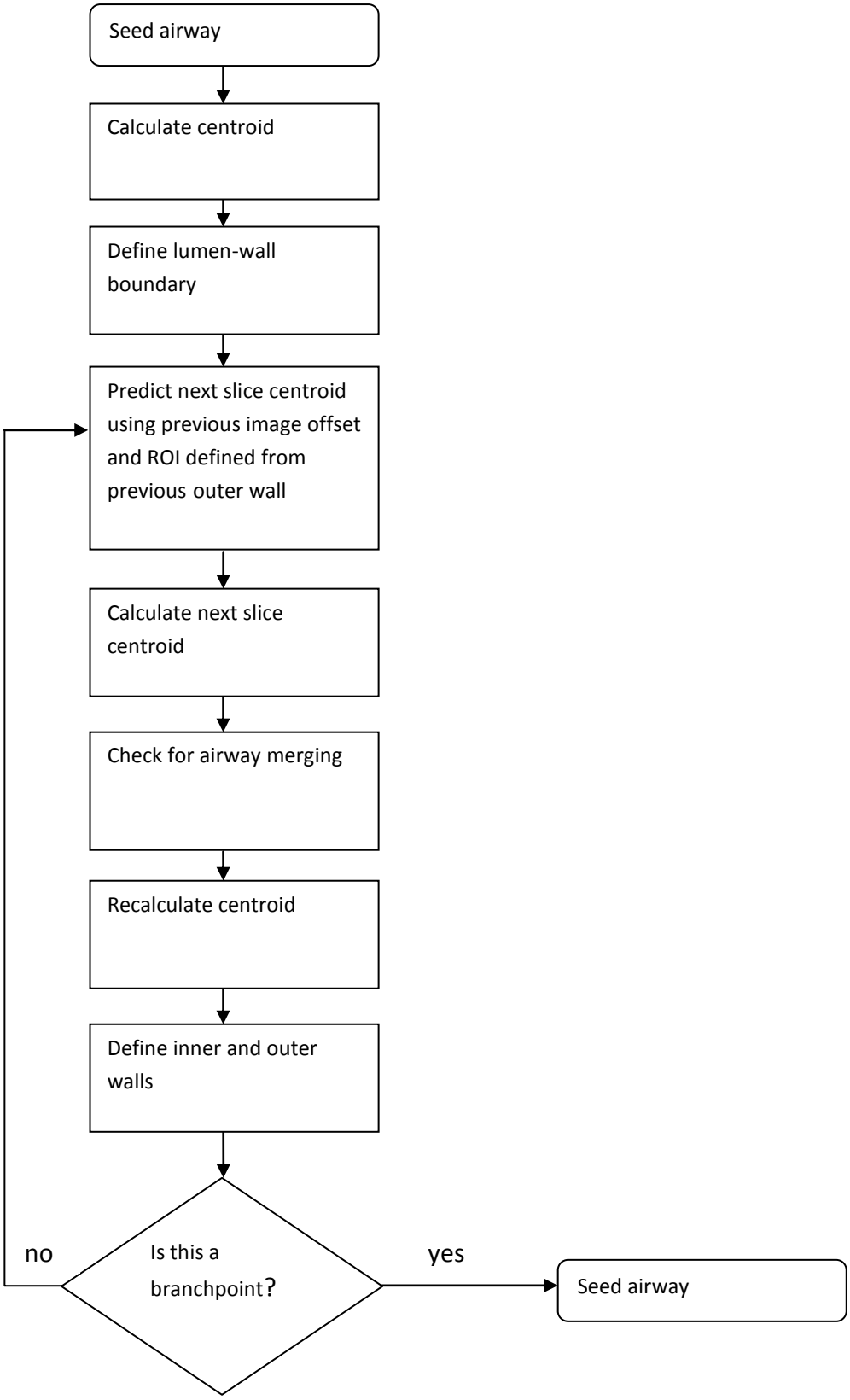

Figure 2.8: Flow diagram showing the steps of airway tree delineation by the CL algorithm

2.2 Results

The three algorithms were tested on a qualitative basis, where their mechanism and settings were modified in order to improve performance.

2.2.1 Thresholding

On testing the thresholding algorithm for lumen and wall segmentation with a number of airways, it became obvious that many pixels from surrounding, similarly dense tissues were included in the segmentation. In the case of the lumen segmentation, the inclusion of pixels from nearby airways and parenchyma was the problem (Figure 2.9).

Since removal of the parenchyma was required, the effect of increasing the threshold was investigated. At increased thresholds it was not possible to remove the nearby airway, since it had very similar pixel values to the airway of interest. Also, as the threshold was reduced, holes started to appear in the lumen segmentation (Figure 2.9B).

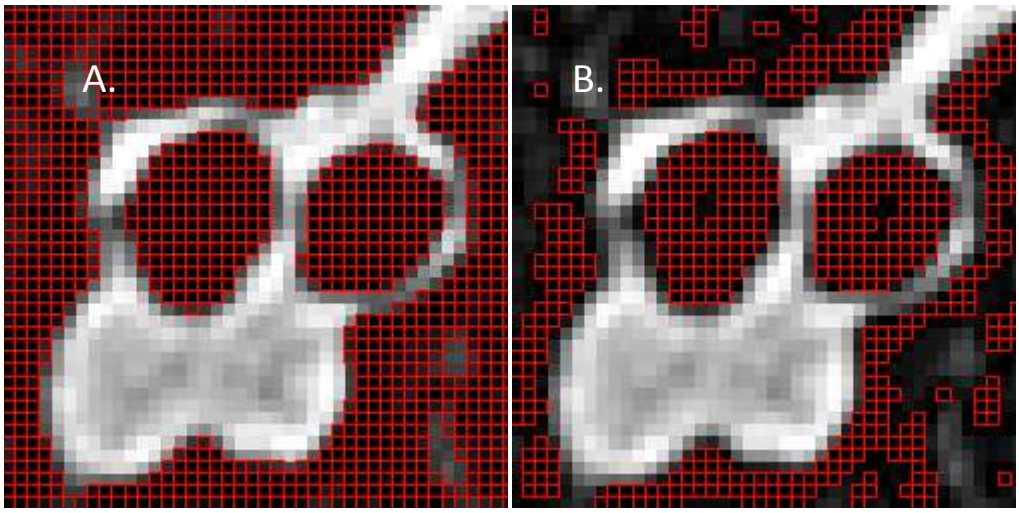

Figure 2.9: Screenshots of thresholding for airway lumen segmentation

Segmented pixels shown in red. (A) lumen at threshold of 10, (B) lumen at threshold of 35

In the case of the wall segmentation surrounding blood vessels and connective tissues were included (Figure 2.10). In an attempt to remove these structures, both upper and lower thresholds were modified to improve the wall segmentation specificity. With increasing lower threshold, removal of surrounding connective tissue was achieved.

Increasing the lower threshold values resulted in removal of the extraneous surrounding pixels, but also removed the airway wall pixels (Figure 2.10B). Reduction of the upper threshold removed some of the pixels in the surrounding blood vessels, but also removed some of the airway wall pixels (Figure 2.10C). Combining both upper

and lower threshold changes resulted in no improvement, since the segmentation still did not include parts of the wall and included parts of surrounding structures of similar density such as blood vessels and connective tissue.

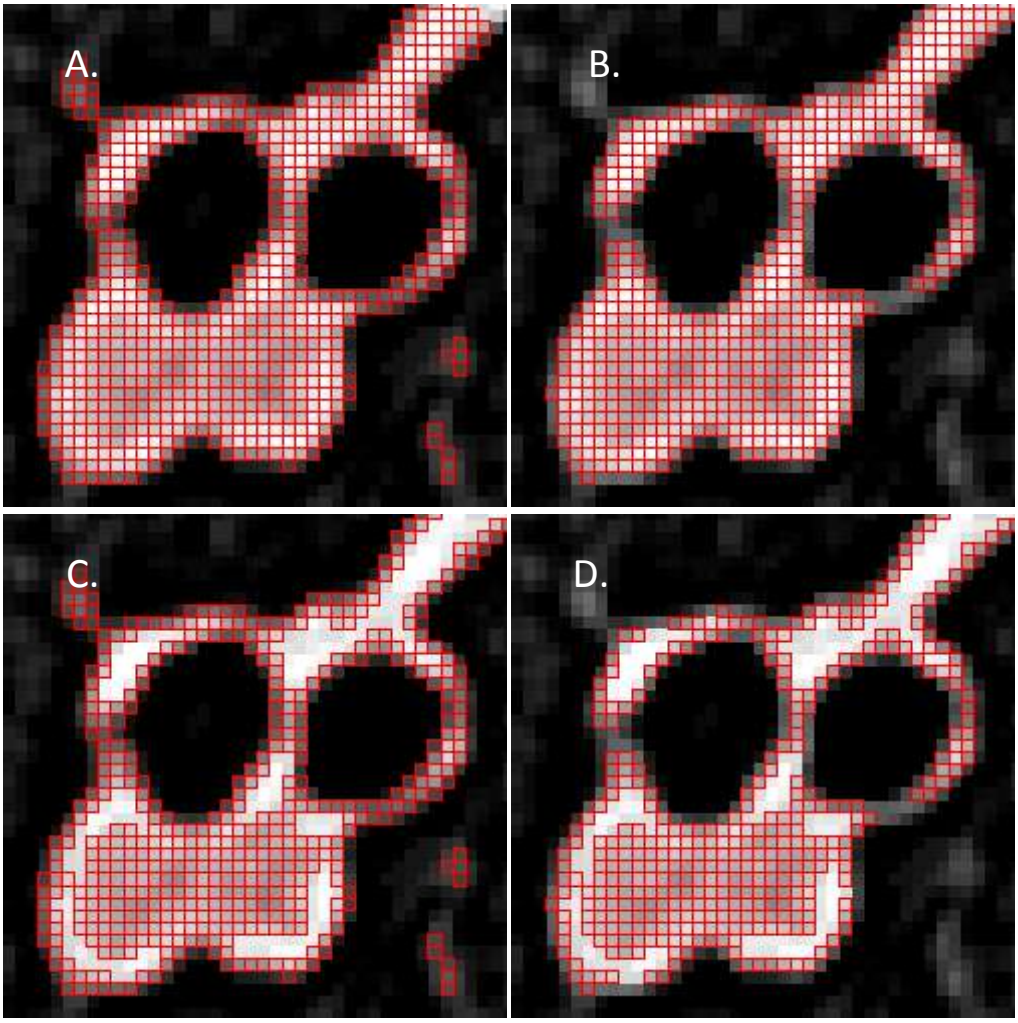

Figure 2.10: Screenshots of density slicing for wall segmentation

Segmented pixels shown in red, with settings as follows:
(A) wall at thresholds of between 2000 and 400
(B) connective tissue removal with thresholds of between 2000 and 686
(C) unsuccessful blood vessel removal with thresholds of between 1330 and 400
(D) wall at thresholds of between 1330 and 686

To help prevent the non-specificity of the segmentation and to improve its discrimination, the algorithm was limited to a user-defined ROI (Figure 2.11). For lumen segmentation, a ROI that encompassed the airway wall and did not include any other structures allowed successful segmentation of the airway lumen (Figure 2.11A). However, if the ROI included any nearby airway lumen or parenchyma, the segmentation became non-specific (Figure 2.11B). For wall segmentation, the ROI position and size determined how much of the walls and other structures were included in the segmentation. As is illustrated by comparing Figure 2.11C to Figure

2.11D, increased ROI size simply results in increased wall area, due to the inclusion of non-discriminated pixels from blood vessels and the nearby airway.

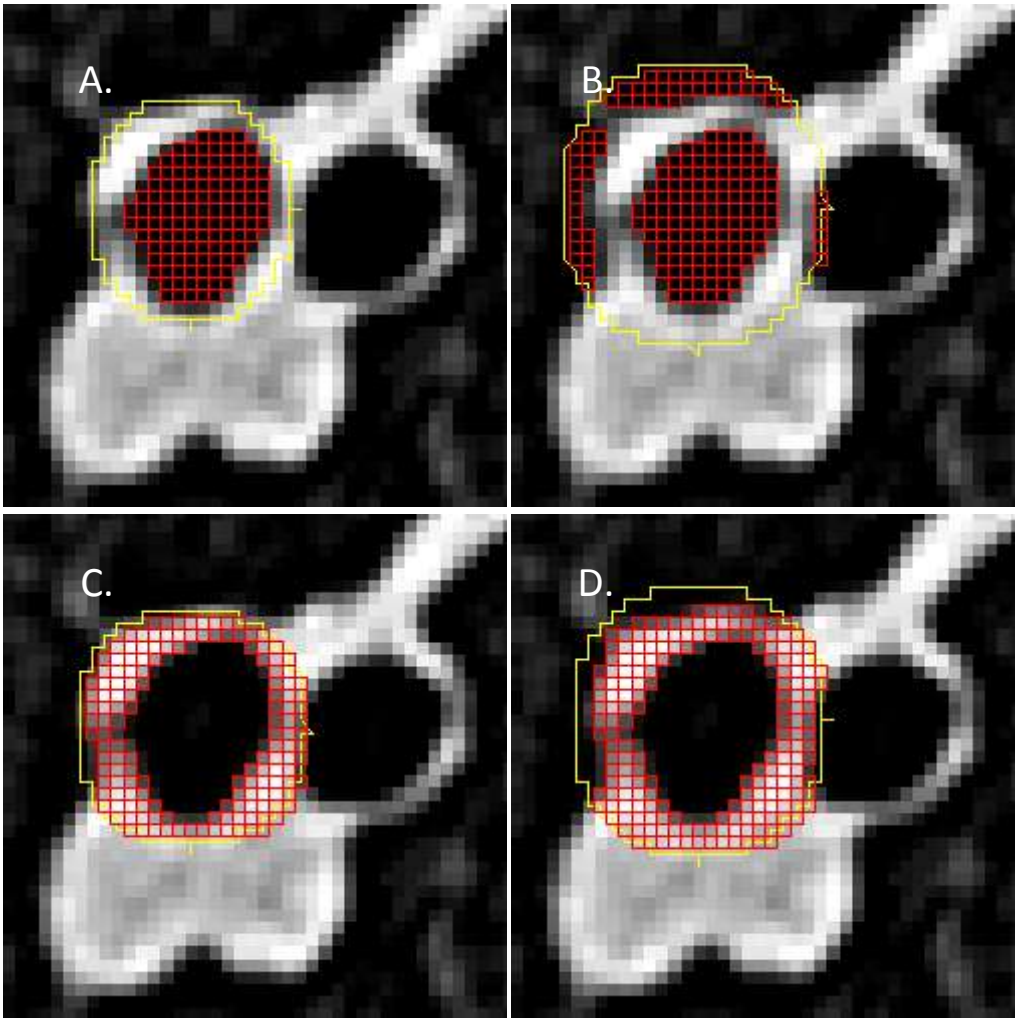

Figure 2.11: The effect of ROI position and size on thresholding segmentation

Airway segmentation shown in red, with ROI in yellow. Settings as follows:
(A) lumen threshold at 130 resulting in area of 119 pixels
(B) lumen threshold at 130 resulting in area of 176 pixels
(C) wall threshold between 2000 and 400 resulting in area of 148 pixels
(D) wall threshold between 2000 and 400 resulting in area of 190 pixels

2.2.2 Region growing

On testing the region-growing algorithm for measuring lumen area in HRCT data, in the majority of airways a reasonable segmentation was produced (Figure 2.12). However, the threshold and tolerance values selected had large effects on the size of segmentation, with increasing tolerance increasing the segmentation area (Figure 2.12B), to the point where a "leaking" from the lumen through the wall into the parenchyma occurred (Figure 2.12C). With smaller airways and thinner-walled airways, leaks into large areas of parenchyma became very common. This leakage was initially prevented by reducing the threshold and/or tolerance, but since the

computation time for this algorithm was much higher than thresholding, leakage of the algorithm caused delays to the display of the result, resulting in small airways taking a long time to measure. In an attempt to overcome the leaking of the segmentation in a more objective way, a mask to filter the holes or outlier was created (Figure 2.12D). Although this prevented the leak, it introduced another user-defined setting, so that the measured area varied as the position of the limiting mask was changed.

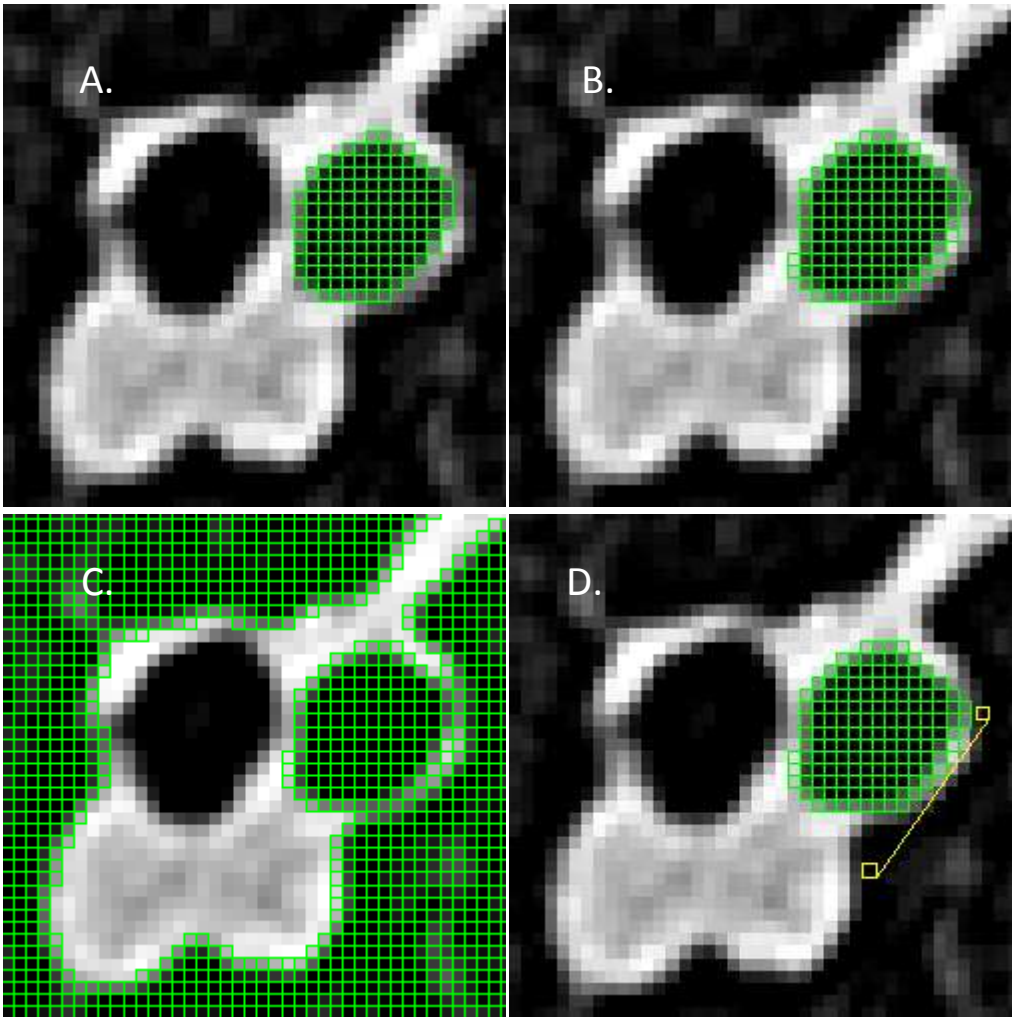

Figure 2.12: Screenshots of region growing for lumen measurement

Segmented pixels shown in green:
(A) lumen at 138 pixels with threshold at 100 and tolerance at 150
(B) lumen at 150 pixels with threshold at 100 and tolerance at 350
(C) 'leaking' problem with threshold at 100 and tolerance at 450
(D) prevention of leaking by application of a limiting mask (yellow)

Wall area measurement by region growing was found to be error-prone (Figure 2.13). Since the variability in density between different parts of the walls was very high, partial wall segmentation occurred unless the threshold tolerance was set high (Figure 2.13A). At higher thresholds, the algorithm tended to include all structures of similar density (Figure 2.13B).

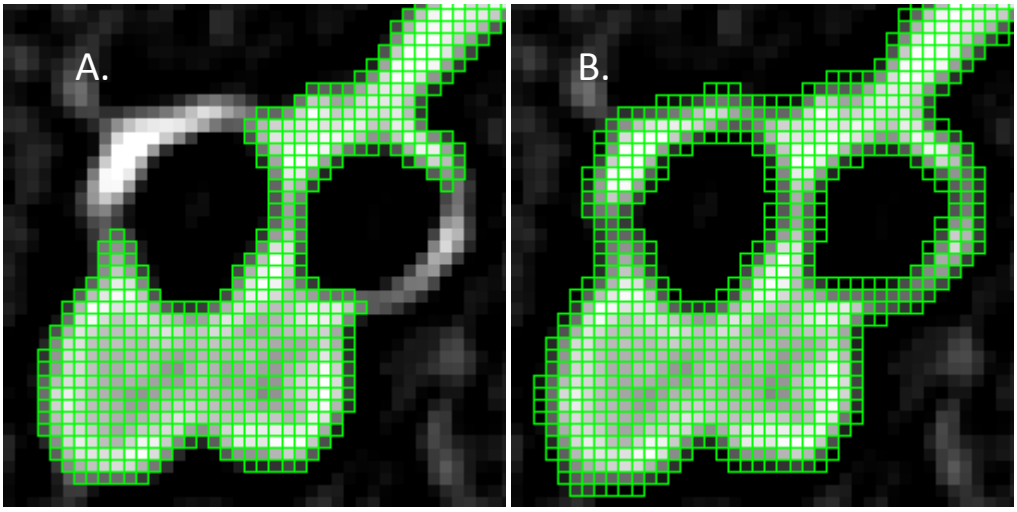

Figure 2.13: Screenshots of region growing for wall measurement

Segmented pixels shown in green:
(A) partial segmentation resulting from reduction in threshold tolerance
(B) inclusion of connective tissue into segmentation result

2.2.3 Ray-casting and centre-likelihood

On testing the CL algorithm for measuring lumen area in HRCT data, a reasonable segmentation could be produced in all of the airways tested. Furthermore, intra- and inter-user reproducibility was very high for larger airways, with almost identical segmentations occurring on almost every repetition (Figure 2.14D).

However, with smaller airways in particular, centroid identification was problematic. If the ROI size was too large the centroid might be identified outside of the airway. If there were two airways inside the ROI then the incorrect airway might be identified (Figure 2.14B) in preference to the airway of interest. It was noted that in some small airways, the centroid position was identified at positions that did not accurately represent the geometric centre of the airway lumen (Figure 2.14D).

In addition, there was an occasional leak where one of the rays missed the wall-parenchyma boundary and terminated at the edge of another more remote structure (Figure 2.14C).

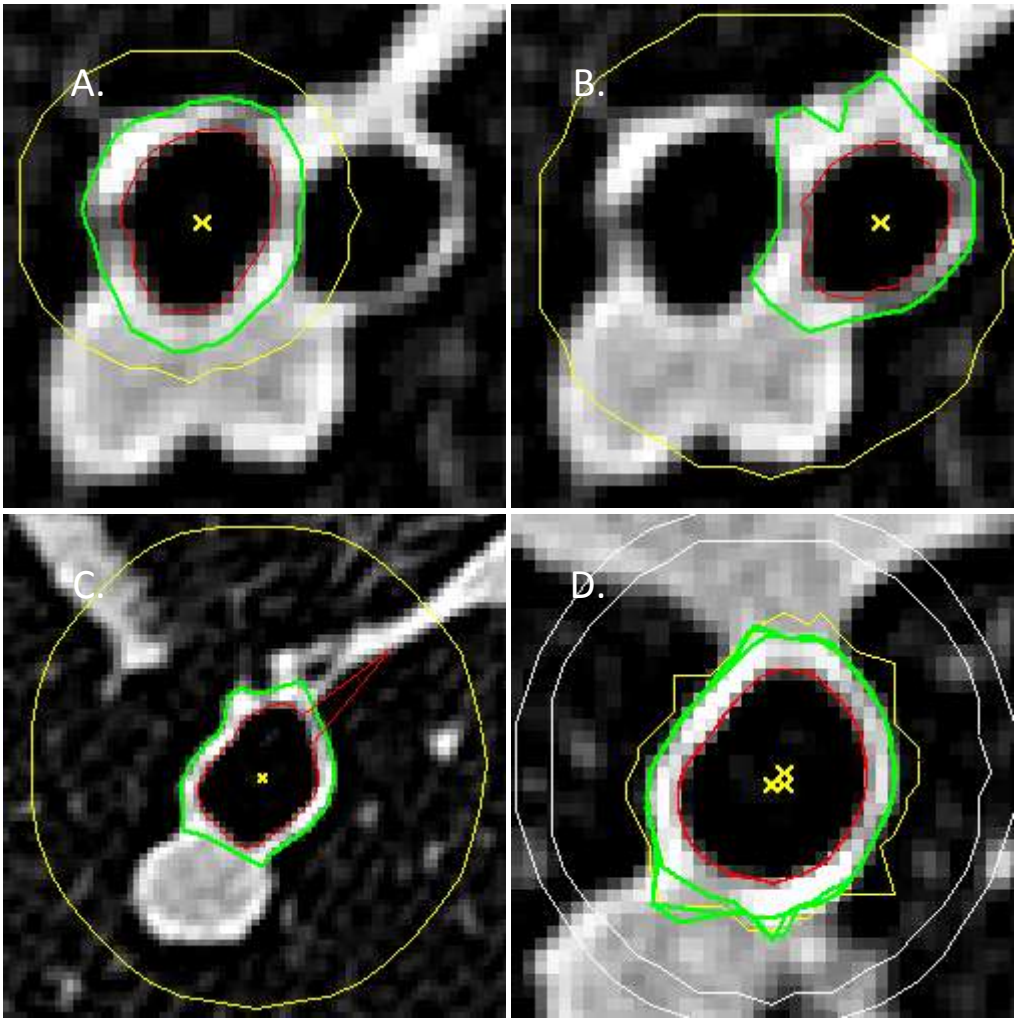

Figure 2.14: Problems resulting from ROI size in CL algorithm measurements

The airway lumen is outlined in red and wall-parenchyma boundary in green. (A) highly repeatable segmentation, (B) selection of the incorrect airway (C) leakage of lumen-wall boundary from one ray (D) centroid position (yellow X)

To quantify these effects, a user-defined ROI that encompassed the whole airway was created on each of the 43 airway images. The CL algorithm result for LA and WA from the user-defined ROI was defined as being the true size.

For each airway, ten observers of increasing inability to estimate the airway size were simulated by automatically creating ten increasing sized elliptical ROIs, each with diameters of six pixels more than the previous ROI. The position of the ROI was not altered since the centroid calculation was in no way dependent on the position of the ROI. Changes in area measurement with increasing ROI were calculated from the difference between measured airway at the computer-based ROI size and the user-defined ROI in all 43 airway images.

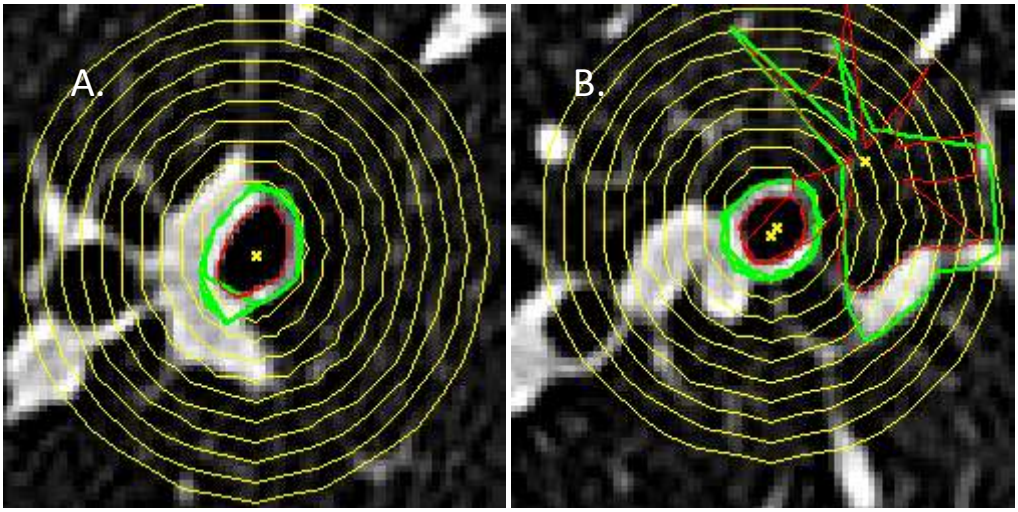

Figure 2.15: Systematic increases of the ROI

The airway lumen is outlined in red and wall-parenchyma boundary in green.
(A) Segmentation largely invariant to ROI size,
(B) Centroid identification outside the airway.

The airway size range was from 71 to 721 pixels OWA, with corresponding user-defined ROIs of 166 to 1225 pixels, and computer-based ROIs ranged from 3730 to 5965 pixels.

Airway measurement accuracy with increasing airway size was estimated in Figure 2.16. Structures of over 100 pixels were accurately measured irrespective of ROI size. Structures less than 100 pixels tended to be over-estimated. When the effect of ROI size on measurements of all 43 airways was investigated, it was found that highly accurate and precise results were obtained where the ROI size was less than 1500 pixels. At ROI sizes greater than this measurement accuracy and precision decreased.

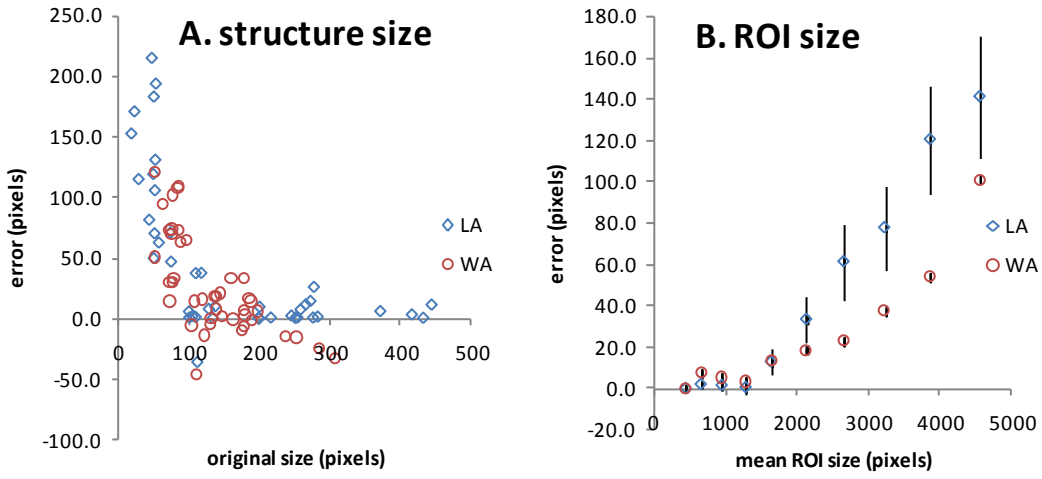

Figure 2.16: Mean error in the CL algorithm

(A) Comparison to true structure size where point represents a mean error of 10 ROI of different sizes (N=43).
(B) Comparison to ROI size where each point represents the mean of 43 airways at each ROI size (N=10)

2.2.4 Refinements to the CL algorithm

Since the problems affecting the accuracy and precision of the CL algorithm occurred sporadically, deletion of the ROI and redrawing it often produced the desired result. To handle the instances when redrawing did not solve the problem, refinements were implemented in the following parts of the CL algorithm:

- centroid identification
- edge detection
- ROI size

Centroid identification refinement

Centroid identification accuracy was most commonly increased by reducing the size of the ROI so it encompassed the airway to be measured and little or no other structures. In some cases, particularly with very small airways, the centroid could not be identified inside an airway. Two solutions were found to this:

1) User-identified centroid. Instead of the relying on the computer-based centroid calculation, the user drew an elliptical ROI around the airway with the centroid defined as being the centre point of the ROI ellipse. This had the benefit of improving the speed of the algorithm, since it bypassed the centroid identification step. However, this introduced an unacceptable level of user-intervention that gave rise to additional variability.
2) Mass centre centroid. This extended the previous solution by using the user-identified centroid as the seed pixel for a region-growing algorithm with a threshold slightly above the value of the seed pixel. The advantage of this solution was that it improved the objectivity of the previous solution and was fairly robust to leaking.

Although these refinements were examined, they were only required very occasionally and therefore they were not used in the thesis. The algorithm performance was satisfactory for the purposes described in later chapters.

Edge detection

On repeatedly testing the CL algorithm on a number of airways, the LA and OWA measurements obtained were largely invariant to ROI size and position.

The only exceptions were as follows:

- where the ROI didn't completely encompass the wall-parenchyma boundary of the airway of interest because the ROI was poorly drawn by the user
- where the airway wall boundary joined to another structure such as a blood vessel or where the airway wall appeared to be stratified by other higher density tissue such as cartilage

In the first case incomplete airway wall (and lumen, in extreme cases) segmentation occurred leading to area underestimation. This was partially countered by calculating the average wall thickness over the wall that could be calculated and then setting the ROI position for that ray to a value greater than this position.

In the second case, a over-segmentation of the airway wall was obtained (Figure 2.17A). To prevent this an additional criteria was required in the ray casting algorithm to prevent this from affecting the result. This was achieved by examining the ray that was cast between the lumen-wall boundary and the ROI for further increases in intensity. As soon as there was any portion of increase the ray was terminated (Figure 2.17B).

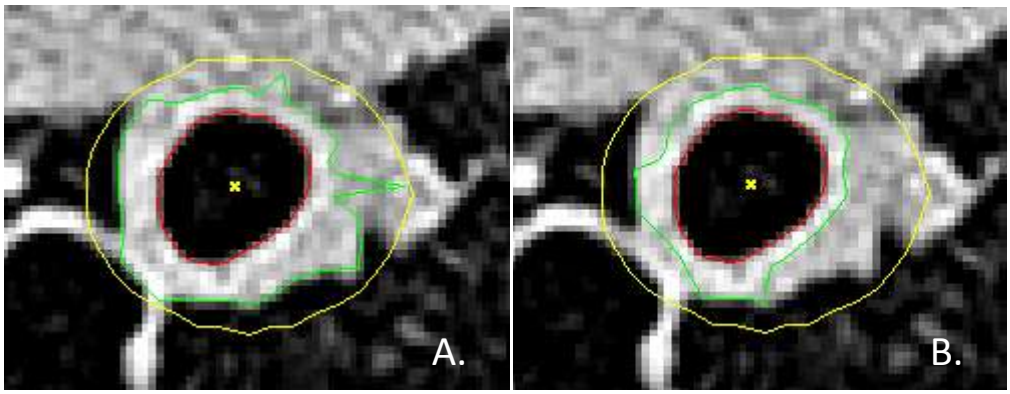

Figure 2.17: Airway wall measurement refinement by early termination of rays

The airway lumen is outlined in red and wall-parenchyma boundary in green. (A) before refinement, (B)after refinement. Notice the refinement has prevented inclusion of a nearby airway wall in the airway of interest's wall measurement (green arrow) and leakage into surrounding non-uniform tissues.

ROI size refinement

For the first measurement the CL algorithm is initiated by the user defining the ROI by outlining an area around the airway (Figure 2.18A), allowing the CL algorithm to calculate the centroid and wall boundaries (Figure 2.18B). In the subsequent image the ROI shape and position is automatically defined by dilation of the previous slice's inner airway boundary and the x-y displacement between centroids (Figure 2.18C).

This method provided advantages as follows:

- automation of the ROI size prediction allowed the tracking of the airway both up and down the airway tree
- decreased ROI size resulting in reduced time taken to find the centroid and reduced chance of finding the wrong airway. Therefore, users who create smaller ROIs are given quicker results, which encouraged them to make more accurate decisions of where the airway wall lied when creating ROIs.

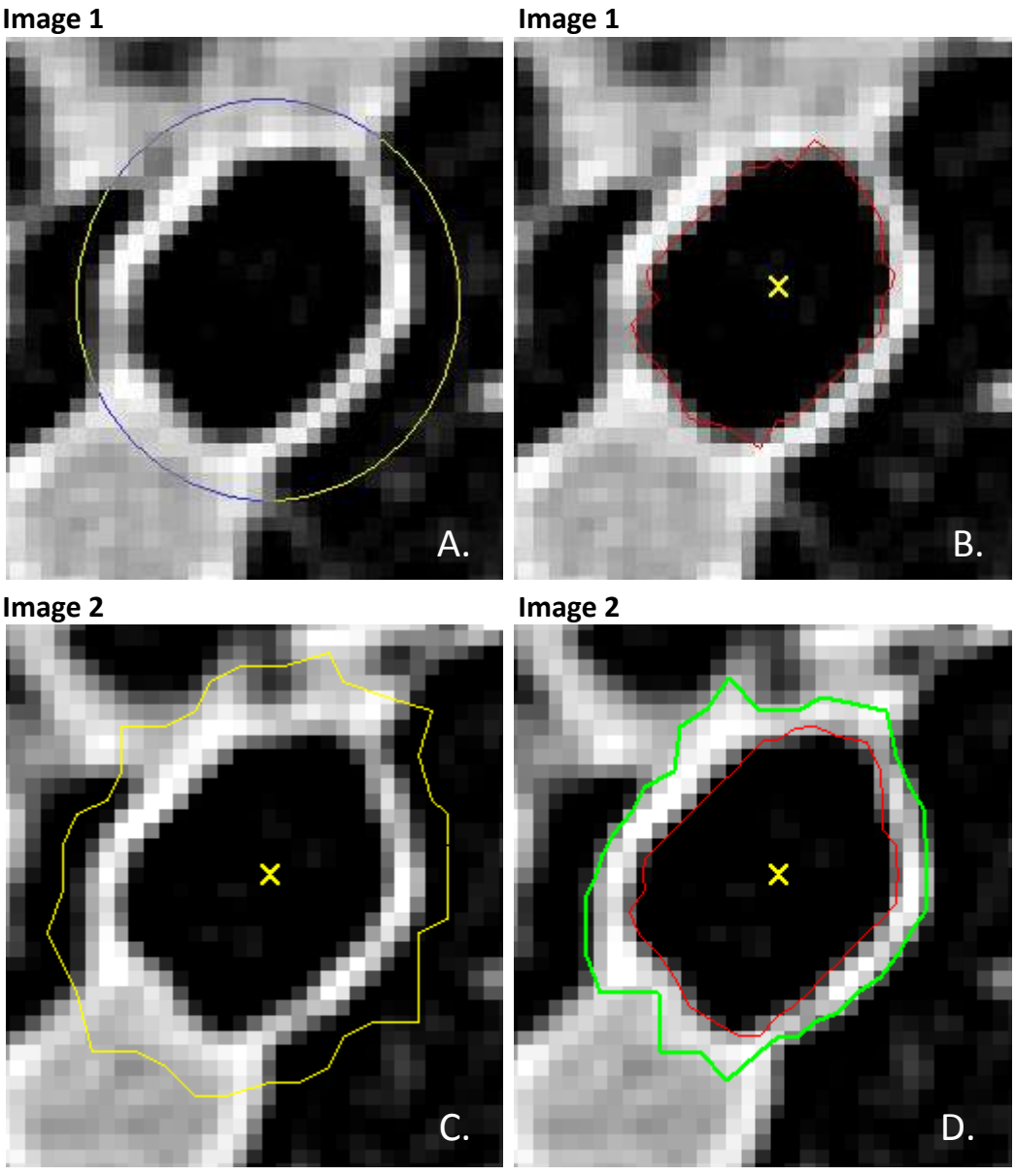

Figure 2.18: Screenshots illustrating the steps in adaptive ROI definition

The screenshots show the use of the CL algorithm in two adjacent slices as follows:
(A) slice 1's user-defined ROI ellipse drawn around airway (yellow)
(B) slice 1's lumen-wall boundary (red) with centroid (yellow cross) defined by CL algorithm
(C) slice 2's ROI defined automatically by dilation of the Slice 1's lumen-wall boundary
(D)slice 2's lumen-wall boundary (red) and wall-parenchyma boundary (green) with centroid (yellow cross) defined by CL algorithm

2.3 Discussion

2.3.1 Thresholding and region growing

Airway lumens and walls can be segmented by thresholding and region-growing algorithms under certain circumstances. However, these algorithms were found to require a high degree of user intervention to obtain acceptable results. This intervention was most often necessitated by 'leaking' into non-relevant structures, something that has been frequently reported in the literature (Wood, Zerhouni et al. 1995; Aykac, Hoffman et al. 2003; San Jose Estepar, Reilly et al. 2008). Prevention of this 'leaking' by altering the threshold and limiting the ROI was attempted with both algorithms.

Since the thresholding algorithm does not take into consideration the fact that the airway is putatively a sealed structure, inclusion of similarly dense non-relevant structures can only be limited by limiting the ROI. Airways are often located in close proximity to other structures of similar density, so the ROI must be accurately determined to include only those pixels making up the airway structure. Since creating this ROI can only be performed by a segmentation algorithm or by a user (Udupa, Leblanc et al. 2006), then this algorithm is either not appropriate or highly subjective.

The region-growing algorithm when applied to LA measurement was also found to leak through the wall from the lumen into the parenchyma. This is due to the sensitivity of the threshold to pixel intensity inhomogeneity and the volume averaging effect often found in low spatial resolution data such as HRCT (Berry 2008). If the threshold is set too low, an incomplete or partial segmentation will occur. If too high, then the algorithm will leak into neighbouring structures. In extreme circumstances this leak grew unbounded into the parenchyma leading to delays in obtaining visual feedback. Noise or variation of intensity resulted in 'holes' or over-segmentation. Although other researchers have managed to choose an appropriate threshold for lumen segmentation, they have done so to find the central axis rather than measure LA (Wood, Hoford et al. 1995).

Ultimately, for quantitative image analysis, the threshold for edge detection must be objective and justifiable. Since the threshold appears to be sensitive to many variables, such as volume averaging and motion-related artifacts (Grenier, Beigelman-Aubry et al. 2003) these techniques will be too limited and subjective for reliable airway measurement.

2.3.2 Ray casting and centre likelihood

The CL algorithm represents a more sophisticated approach to allow for the more realistic intensity variations found in clinical data. Given a seed point, it can successfully determine the centroid of the airway, and use that information to reliably and repeatedly define the lumen-wall boundary. By defining the lumen-wall boundary in each ray, this algorithm overcomes the problem of selecting a single threshold to identify the whole lumen-wall and wall-parenchyma boundaries. This should prevent the under-estimation of LA often found in region-growing algorithms (Wood, Hoford et al. 1995), resulting from too low a threshold.

Furthermore, in this chapter the CL algorithm has been extended to include novel methods for preventing over-segmentation of the airway wall. As recently demonstrated by (San Jose Estepar, Reilly et al. 2008) the half-max edge-detection method can be somewhat sensitive to airway 'leaking' into surrounding structures if the ROI encompassed those structures. Later iterations incorporated refinements which reduced the algorithm's sensitivity to this problem.

Similarly, if the wall could not be identified in some rays perhaps due to the ROI being inaccurately positioned or created too small, this resulted in omission of part of the wall. Although this caused problems for earlier iterations of the CL algorithm, this problem was rectified with a novel refinement, on this occasion by expanding the ROI to include an area greater than the average airway wall thickness.

The application of airway boundary size and position to create ROIs for subsequent images has been coined "Adaptive Regions of Interest" (Tschirren, Hoffman et al. 2004). It was found to successfully contain 'leaks' into the surrounding parenchyma and reduce the overall computing time by analysing the volume locally instead of over the entire data set. The current study used a similar idea to predict the shape of the airway in subsequent slices. However, it extended the work of Tschirren, Hoffman et al. 2004 who used elliptical ROIs, by using the more advanced technique of dilating the lumen-wall boundary to create the ROI shape. Since the CL algorithm's reliability was found to be largely invariant to ROI size, the main advantage of this was to accurately localise the airway position in 3-D during the tracking process.

The experiment in Section 2.3.2 examined the effect of increasing ROI size on airway measurements gave some indication of the precision, but not the accuracy, of the CL algorithm since no true measure of airway lumen or wall was possible from this clinical data. However, the CL algorithm was found to be robust in the face of increasing ROI size and now provides automatic ROI size prediction, and as a result offers great potential for fully automatic 3-D segmentation of the airway tree.

In the context of this thesis, the CL algorithm provides a simple, fast and robust technique to determine the airway centroid when given an image of an airway and a seed point. In Chapter 4 the effect of parameter choice on CL algorithm accuracy and precision will be examined.

CHAPTER 3

Software implementation

The *winImageBase* software was created to provide a support platform for developing and validating HRCT airway algorithms described in this thesis. *winImageBase* has been subsequently used by researchers at the Woolcock Institute of Medical Research as a research and teaching tool for academics and students. The software is now a commercial product available to physicians who require state-of-the-art analysis and imaging techniques to measure airway dimensions from HRCT scans.

The software design, prototyping and programming were undertaken using some of the techniques now described as Agile Methods and explained in http://www.agilemanifesto.org/

These can be summarised as follows:

- satisfy the customer through early and continuous delivery of valuable software
- welcome changing requirements, even late in development
- deliver working software as frequently as possible since this is the primary measure of progress
- work together daily throughout the project
- build projects around motivated individuals
- continuous attention to simple and good design
- effective communication with the team on a face-to-face basis.

These practices ensured that high quality software was delivered quickly, and to specification. However, there are some limitations in the software design that have come to light, particularly involving scalability, maintainability and platform independence when used in clinical settings. These aspects are considered towards the end of this chapter and new judgments are presented to show how to proceed with the design of the next version of the software.

3.1 Requirements definition and specification

The *winImageBase* specification focuses on code re-use (Madau 2008) and the development of a quality user interface to provide an easy-to-use system, designed for use by researchers. This broad starting point enabled the requirements to be more formally defined.

3.1.1 Requirements definition

Meetings were conducted with the key members of the Clinical Mechanisms team to determine the goals, functions, and constraints of the new software system. From these meetings a brief statement was defined as follows:

The software must provide a means of making measurements from a series of images using various image analysis algorithms. The software must be of commercial quality and compatible with Microsoft Windows.

3.1.2 Requirements specification

The requirements definition was developed into a flexible *requirements specification*, with the final scope of the project limited by the ability to develop the algorithms and provide a suitable *graphical user interface* (GUI) using the tools available and within the time-limits imposed by the research:

- develop an environment for experimenting with and further developing various airway segmentation algorithms.
- provide a commercial quality interface compatible with current versions of Microsoft Windows (2000/XP and Vista)
- re-use existing algorithms where possible
- provide viewing of image files generated by various medical imaging platforms.
- interface with MS-Excel for additional statistical analysis.

3.2 Development environment

After the specification of *winImageBase* had been agreed by the Clinical Mechanisms team, the development language and environment were chosen. The high number of images to be processed and numerical content of the image analysis algorithms required a language that offered favourable execution speed from compiled code. Speed was chosen as the criterion since there is little to choose between most high-

level languages regarding accuracy. Some languages such as Java or any one of the languages utilising the .NET framework did not, at least at the time, provide suitable performance. In the end *C++* was chosen as the development language for several reasons:

- *C++* offered the best combination of execution speed, object-oriented features and memory management
- the original CL algorithm code was written in *C*
- suitable Microsoft Windows-based development tools exist for *C++* including *Microsoft Visual C++* and *Borland C++ Builder*
- Third party tools, for example for charting and reporting, are widely available with *C++* and Microsoft Windows interfaces.

The two potential software development tools - *Microsoft Visual C++* and *Borland C++ Builder* - were compared. Both development environments provide *integrated development environments* (IDEs). They offer good project management facilities with a project dialogue box showing all the files and components of a system. Both have strong editors, incremental compilers and good debuggers but with varying capabilities. Both systems support the latest *C++* extensions such as *bool*, namespaces and the Standard Template Libraries and each support *Microsoft foundation classes* (MFC), essential for programming native Microsoft Windows applications.

However, visual GUI building is absent from *Microsoft Visual C++* and this is a major drawback for *rapid application development* (RAD). Conveniently, Borland has also abstracted Microsoft's MFC to provide a simpler programming interface through their *visual component library* (VCL).

Borland C++ Builder was chosen as the development environment because it was more comprehensive, especially regarding GUI development. The GUI building capability and the VCL abstraction of the MFC library combine to produce a well-designed RAD tool.

3.3 Design and prototyping

Instead of having a fixed architecture for *winImageBase* at the start of the project, the software was constructed incrementally in small stages. This allowed continuous review of the application and addition of new features in response to new user requirements identified during prototyping. For example:

- there were no initial plans to write code to perform synchronised pre/post-treatment analysis on the data using two executables

This requirement was added towards the end of the project, during the assessment of the CL algorithm's performance in clinical datasets

- after implementing the synchronisation function, it was realised that it would be a small extension to allow the user to perform registration between two corresponding data sets in synchronised *winImageBase* executables.

The main benefits of this approach to programming *winImageBase* were that the project was flexible enough to adapt as new techniques and skills were developed. Now that *winImageBase* has been produced and has been used for some time by a number of research groups, it is possible to determine what features would be useful and how the application should be developed in the future.

3.3.1 Prototyping *winImageBase*

Several 'throwaway' prototype systems were developed to understand how an integrated environment could work. One such prototype can be seen in Figure 3.1.

Although this prototype is no longer used, it was useful at the time to highlight several important requirements:

1. users wanted to be able to interactively review the immediate data around the ROI by zooming and panning the image and by examining adjacent images. Also altering the *Window level* and *width* was considered important
2. standardisation: the position, zoom, level and width as set to one image should be applied to all images in the volume/series
3. results of HRCT image algorithm should be superimposed onto the images
4. all the airway measurements from a single airway (i.e. between branch points) and their relationship to the images from the HRCT series need to be easily collected together and viewed
5. it was desirable to be able to automate obtaining results from the software to some extent. This would be mainly by propagating the results from one image to the next in the series. In this way the airways through the CT series so measurements of whole airways could be more objectively computed
6. an export facility should be provided to allow results to be analysed in standard applications. These included spreadsheets, such as *Microsoft Excel*, databases such as *Microsoft Access* and statistical analysis packages such as *SAS*)
7. locating and measuring the same airway in different patients or in the same patient pre/post treatment was particularly time consuming. Some method of alignment of two volumes was required
8. it was important to be able to close the program and resume from the position.

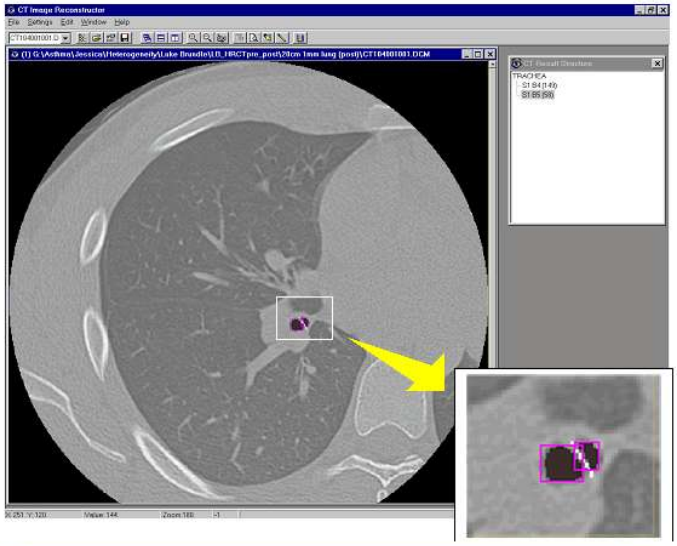

A. Image 1

Two airways (shown in black) are measured by a region growing algorithm, separated by a rectangular ROI (red) and a limiting tool (white)

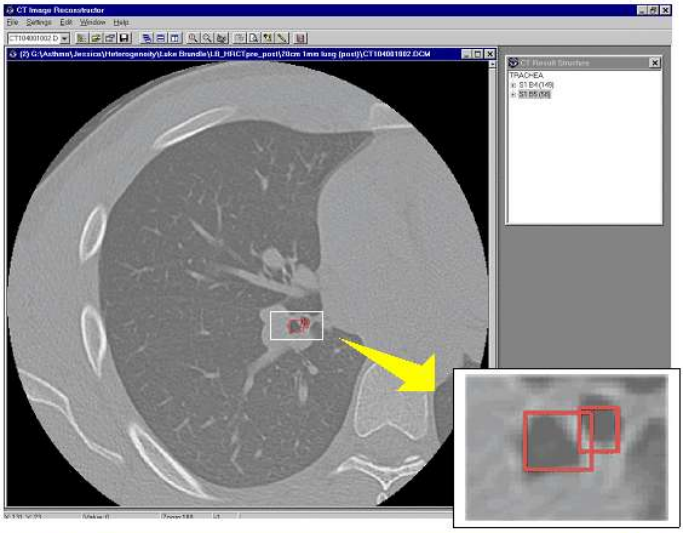

B. Image 2

The ROI position and size have been transferred from the previous image to create candidate ROI positions (orange)

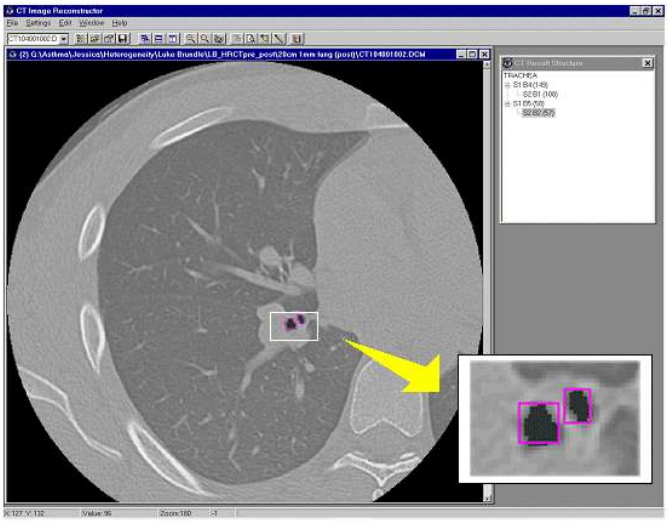

C. Image 2

The user clicks in each candidate ROIs and the ROI have been successfully measured allowing the semi-automatic delineation of the airway tree

Figure 3.1: Three screenshots of prototype software tracking

Overlay shows an early region growing segmentation algorithm being used to measure and track two airways in adjacent HRCT images

Project-based operation

Analysis of a data set can involve many experiments. The first iteration of the software, *CT Image Reconstructor,* allowed single experiments to be run, where it was up to the user to manage the results as they were produced. Since analysis of the performance of image analysis algorithms on an image data set can involve many experiments, it soon became clear that it would be beneficial to manage repeated experimentation on a data set within the context of a *database environment*. This lead to the proposition that experimentation should be recorded for a given data set and that the resultant database should be able to be saved to disk and loaded back into *winImageBase* at a later time.

Data set management

One of the requirements that came from developing a prototype system included the facility to view multiple data sets. Data sets fall into three categories: (1) the simulated data used to develop the algorithms, (2) the phantom data sets used to validate the algorithms, and (3) patient data set used to test the algorithms in a clinical setting.

A number of components are available within *Borland C++ Builder* for retrieving and displaying data, ranging from reading the data into a text box (the simplest) to a full database option (the most complex). The database solution introduced additional complexity to the software, requiring either a database engine to be shipped with *winImageBase* or by providing an Open Database Connectivity (ODBC) interface to the user's existing databases.

For this first version of *winImageBase* it was more important to provide the core functionality of HRCT image analysis algorithms so the database development was dropped. Ultimately, a user's data would most likely be available in spreadsheet, database or plain text format.

Although this approach requires the user to export their data to an ASCII format file, it was felt that it provided the greatest flexibility for the least development effort leaving, as a priority, the main task of developing the analysis algorithms. A method to retrieve the text files and display the data in the *TreeView* component mimicking the airway tree structure was chosen.

Results visualisation

Initial prototypes used a commercial version of *LeadTools ActiveX Component Library* since it supported many image types, and had many tools for loading and manipulating image data. However, over time as more sources of medical images were included, more sophisticated image handling was required. It became apparent a large amount

of development effort was being devoted to learning to use LeadTools. The pixel data stored within each of the data files could also easily be displayed in the standard Windows visual component that *Borland C++ Builder* encapsulated, the *Timage*. However, this proved to be cumbersome to program and slow to execute. Other problems included flickering images during zooming and panning. Although the learning curve was very high, it was found that the Windows Application Protocol Interface (API) provided very fast and flexible graphic display capabilities. Optimised routines were written to load and manipulate many file format types in memory including dicom, bitmap, interfile, raw, and tiff.

Although standard numerical results from the algorithms, such as wall and lumen area were easily displayed in any of the standard Windows visual components, it was also desirable to include additional graphical information about the images. The charting components available in *Borland C++ Builder* were compared during prototyping. The *TeeChart* component was chosen because the component includes the ability to display scatter plots, histograms, three-dimensional charts, line charts, real-time charts and custom drawing routines. In addition to these visualisation techniques, methods to zoom/pan, print/preview, export and customise the charts were also provided.

Exporting results

To enable statistical analyses and modelling of the algorithm results, an export facility was built into the software. This allowed results to be directly transferred into spreadsheet, database, presentation and mathematical software. All components that contain data, charts and results were implemented with an export facility. It was decided to export charts as either a chart image (in a number of standard image formats) or as raw data for re-generation in another application. These routines provided enough flexibility to analyse the results and re-create the charts in most readily available software.

Handling user interaction

Handling normal user interaction with the GUI had to be maintained even when *winImageBase* was performing processor-intensive tasks and this was achieved using threads. Although this produces a slight computational overhead in terms of thread management and multi-tasking, it is not onerous and is more desirable than removing all user interaction with the application while computation is being performed. Feedback was provided to the user with a progress bar and a cancel button which the user could press to cancel the current operation, if required.

It became apparent that the software was often used to examine different types of scan of the same object, for instance a pre-/post-treatment clinical data sets or Micro-

CT/HRCT scans of a pig lung phantom. This meant that quickly locating and measuring the same airway in different datasets was important. The advent of multi-core CPUs and cheaper liquid crystal display units made development of a system designed to be used with a dual screen workstation with a dual-core CPU feasible. An inter-process communication protocol was developed using the MS-Windows API to enable bidirectional communication between two (or more) distinct *winImageBase* executables (Figure 3.2), with the following advantages:

- synchronisation during zooming and panning of images
- synchronised measurement. When the user creates a ROI on one *winImageBase* executable, the same ROI is automatically created on the other *winImageBase* executable. Each executable initiates the CL algorithm and both ROIs are measured without any loss in speed because each executable's processing is automatically performed by a different core. This effectively allows the user to measure and track two airways in the same time as it took to measure a single airway
- the ROI for both airways is defined over the same part of the image, so any user-introduced measurement error will be the same on both datasets. This may further decrease subjectivity of the CL algorithm

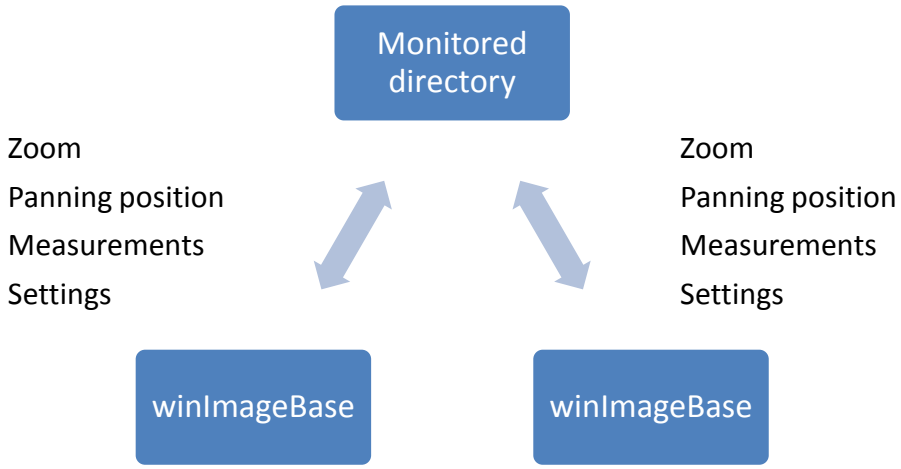

Figure 3.2: Inter-process communication between two winImageBase executables

Communication was achieved by updating a text file on a monitored directory with changes to zoom, panning position, addition of removal of ROIs and other settings.

An extension of this protocol allowed semi-automatic registration two-dimensional alignment of two datasets. By setting user-defined fiducial ROI to serve as markers of reference on the same structure in two datasets, it was a simple task for either executable to automatically compute the required zoom and panning position automatically align the datasets in either direction.

3.4 Discussion

winImageBase is a fully functional application that meets the original design specification. It enables practitioners from any field to make airway dimension measurements with the minimum of effort.

In the evolution of the project it has become apparent that many other features could be useful and these are introduced here.

The *winImageBase* interface evolved through various prototypes and in its current form has proven very usable. It has provided a development environment for integrating, testing and debugging several HRCT image analysis algorithms.

There are some structural improvements that could be made to the code as complications have been introduced as *winImageBase* has evolved. The original code has been repeatedly adapted as the algorithms have been modified and improved. This creep effect has been very hard to eliminate because many of the features now in *winImageBase* were not envisioned during the preliminary design stage.

3.5 Future development

This section considers features to assist with image analysis algorithms and model building, or technological approaches that could be adopted to improve the performance of the software.

3.5.1 Fully automatic airway segmentation

Operation of the *winImageBase* program requires a suitably qualified analyst to locate the airways and interpret the segmentation results. This dependency on skilled users could be reduced by automating the airway recognition part of the process.

winImageBase was constructed as an image analyst's workbench and, as with any such tool, there is a learning curve which must be ascended to acquire the necessary skills to apply the tool effectively. However, as more experience in the use of *winImageBase* was gained, an initial analysis protocol was developed. It has become apparent that much of the analysis process could be automated with relatively small loss in effectiveness. It thus appears quite practical to construct an automated tool which presented with a data set and some general data-semantics could perform a complete airway tree analysis and return the results to the user in the form of a report and models in the form of, for example, *MS-Excel* macros.

To produce such software may be a requirement to construct a rule base extracted from the experience of many *winImageBase* experiments and this would require some further research. Such a tool might well form a useful and commercial product.

3.5.2 Three-dimensional analysis

The current design of *winImageBase* has limitations preventing true 3-D analysis. Since each image is considered separately, all the images in a dataset are not required to load into memory, facilitating fast program startup and data set retrieval. To carry out true 3-D analysis, the dataset would have to be loaded into memory, allowing processor intensive calculations such as tri-linear interpolation for reslicing of the data to execute without disk access. Techniques such as 3-D registration require both data sets to be loaded into memory, and the allocation of a temporary memory buffer of the same size as the largest data set, which in the case of the latest micro-CT technology can be in excess of 10 GB. This is not feasible in 32-bit operating systems, and while 64-bit hardware and operating systems are now available, they are not yet in widespread use.

Since another piece of software used extensively throughout the thesis (*win3D* described in Section 5.3.1) already contains many of the functions to perform 3-D image manipulation, it is a matter of integrating the functionality of *win3D* with the CL algorithm into a 64-bit operating system to allow for large data sets to be processed within a reasonable time.

3.5.3 Visualisation

In the current iteration of the software no 3-D volumetric data visualisation was provided. 3-D airway tree visualisation, although not necessary for the current study, has several advantages in a clinical setting, such as aiding diagnosis by depicting the airway anatomy in any orientation (Remy-Jardin, Remy et al. 1998), and virtual bronchoscopy (Suter, Reinhardt et al. 2008). Research is currently being conducted to measure the impact of these methods in a clinical setting (McLennan, Namati et al. 2007).

Graphical routines in *winImageBase* were implemented using *TeeChart*. Although this software component provides some very flexible features, it is virtually impossible to extend the usability of *TeeChart* beyond that envisioned by the authors. This is a limiting factor of the component when additional visualisation routines are required. The *TeeChart* component is also bonded to the Microsoft Windows environments, making the transition to a platform independent version of *winImageBase* more

problematic. At present some or all of these limitations would be overcome by choosing new or additional charting components.

3.5.4 Platform independence

The goal of platform-independent software is primarily to extend the market audience. Importantly this goal provides a secondary benefit over multiple platform implementations in that only one variant of the source code is maintained and developed.

At the time when *winImageBase* was being specified it was decided to use *C++* because that produced the fastest code. Additionally *Borland C++ Builder* was chosen to provide the best way of coupling the algorithms to an interface. At the time *Java* was considered it did offer platform independence, but was not a serious contender regarding execution speed, because it required a virtual machine to interpret the Java code. However, there have been massive performance improvements since the project was specified and *Java* would now provide a more credible development language.

However, using a single development language is not necessarily the only solution. The speed of *C++* code still makes it superior to Java, and is available for most computer architectures. Providing development follows standard conventions, such as those specified by American National Standards Institute (ANSI), then a single implementation of the code can be compiled for multiple architectures. In this way, the next version of *winImageBase* may benefit from the speed of the *C++* algorithms and a platform independent *Java* interface.

3.5.5 Distributed/parallel algorithm implementation

One of the limitations of the current implementation of *winImageBase* is that it cannot handle very large data sets in reasonable time due to the required computation.

3.5.6 Database support

Linking *winImageBase* to a database could provide two important improvements. The first is that a database could be used to store all of the experimental results. The second is that a lot of commercial data is stored within a database and this could be accessed directly rather than requiring the user to export data from the database prior to image analysis algorithms.

ODBC (open database connectivity) and JDBC (Java database connectivity) provide industry standard interfaces for database access. If *Java* or *C++* is used as the development language then these tools could be employed accordingly.

The volume of data held on corporate databases can be very large, so if *winImageBase* is turned into a data mining application accessing large hospital databases then the image analysis algorithms would have to be speeded up using some of the ideas discussed in the previous section.

3.5.7 Internet access

Internet access to *winImageBase* provides a number of attractive solutions. Firstly this approach provides an attractive way to handle software licensing because the user would be required to connect to a license server that would validate the authenticity of the user/software. Secondly it is feasible to implement the interface to *winImageBase* as a *Java* or *ActiveX* application that could be accessed using a web browser. This could provide a method of analysing data via an internet connection, perhaps providing access to a powerful remote machine that would otherwise not be available to the user.

However, there are still technological limitations to such an implementation where the bandwidth would limit how much communication could be made to the remote machine. In the case of running *winImageBase* remotely, only modestly sized data files could be transferred in reasonable time.

CHAPTER 4

Parameter selection

To be clinically useful, HRCT segmentation algorithms must be accurate and precise, and deliver airway measurements with minimum delay. Chapter 2 established the CL algorithm as a robust HRCT segmentation algorithm for measuring airway narrowing and airway wall thickening in pulmonary diseases such as COPD and asthma. This was based on observations of reliability and speed in areas such as leak prevention. Now that a suitable algorithm has been selected for airway measurement, a more rigorous and objective approach is required to assess its performance and select optimal parameters for its use.

The use of computerised airway models has been stated as being the crucial first step for the purposes of HRCT segmentation algorithm validation (San Jose Estepar, Reilly et al. 2008). This is because artificial data eliminate the experimental and biological variance found in clinical data, and therefore establish a ground truth for airway dimensions.

The model developed in this chapter contains simulated airways of known size, referenced from the literature on airway dimensions. This model is used to evaluate the effects of the following user-defined parameters on the CL algorithm's performance:

- edge detection mechanism
- number of rays
- amount of interpolation.

The performance indicators were the effect of these parameters on the algorithm's accuracy, precision and speed. The aim was to validate the algorithm against computer-generated experimental data, thereby simplifying optimal parameter selection.

The theory underlying ray-casting was reviewed to help explain its effect on the algorithm's performance, and this is now shown.

4.1 Ray-casting approximation theory

Assuming the airway centroid has been identified, the first step in measuring lumen area (LA) is casting *n* rays from the airway centroid to the lumen-wall boundary. The lumen area (LA) is calculated by joining each of the edges together to form a polygon of *n* vertices. Assuming the airway to be measured is a circular object of radius *r*, its area can be approximately represented by the equation shown in Figure 4.1.

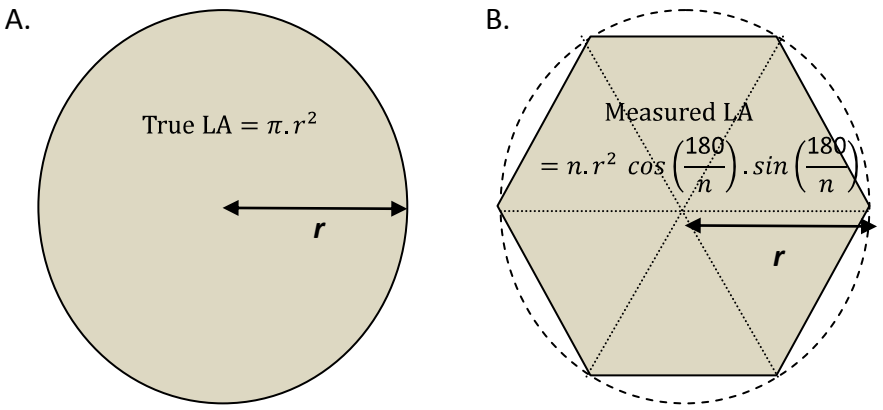

Figure 4.1: Ray-casting approximation theory

Area calculations and areas shown in grey: (A) Circular airway, (B) hexagonal n=6 approximation of circular airway. Notice that the number of vertices is equivalent to the number of rays cast.

From Figure 4.1, the difference between the true and measured areas can be expressed as an error in estimation:

$$\text{error} = n . r^2 \ cos\left(\frac{180}{n}\right) . sin\left(\frac{180}{n}\right) - \pi r^2 \quad \textbf{(4.1)}$$

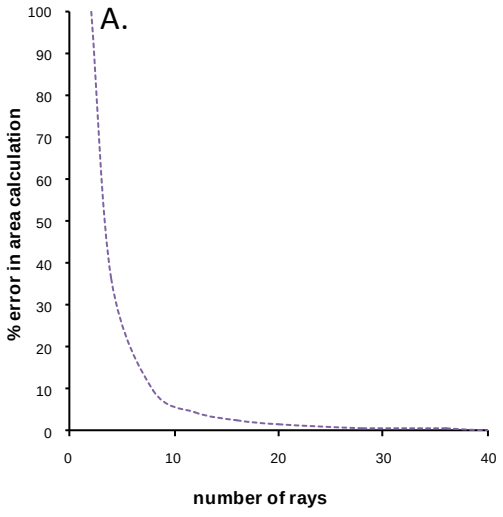

B.

Number of rays	Area % error
2	100.00
4	36.34
8	9.97
12	4.51
16	2.55
20	1.64
28	0.84
36	0.51
40	0.41
80	0.10
100	0.07

Figure 4.2: Theoretical effect of number of rays cast on area estimation

Area percentage errors resulting from equation (4.1) and shown as graph (A) and as table (B).

Using equation (4.1) the extent of the area percentage error can be evaluated (Figure 4.2). For any number of rays, the area is always under-estimated. However, the percentage error in lumen area estimation rapidly decreases to near zero with increasing ray number, so that from 12 rays onwards the error is less than 5 per cent.

Since ray casting is used to calculate LA, OWA and WA in the same way, the same percentage error will occur for all measurements.

4.2 Methods

The CL algorithm's performance in terms of accuracy, precision and execution speed was evaluated on simulated data of known dimensions and density. The following steps were carried out to construct and manipulate the model dataset, measure its airways and evaluate the CL algorithm's performance.

4.2.1 Simulated CT data preparation

In order to create a model of HRCT airways, reference values were required for the intensity and size of structures typically found in lung HRCT images.

Airway intensity selection

The intensity values for the simulated airway lumen, airway walls and surrounding parenchyma were obtained from HRCT images of a random selection of patient data. Using the *winImageBase* software, a line was drawn through different structures in the HRCT images. These were used to create a profile from which the average intensity through this structure was calculated. In Figure 4.2 the process of creating airway lumen and bone pixel profiles is illustrated. The mean density value of parenchyma was determined as 725 HU, whereas the mean value in the airway lumen was found to be 135 HU. These values were normalised against bone (2700 HU) and air (0 HU) to create reference values for the model data (Table 4.1).

TABLE 4.1: REFERENCE VALUES USED TO SELECT PHANTOM AND MODEL DATA PIXEL INTENSITY

Structure measured	Intensity value range (HU+1000)	Mean normalised value (% of bone)
Wall	1300-1800	57.6
Parenchyma	500-950	26.9
Lumen	0-185	3.4

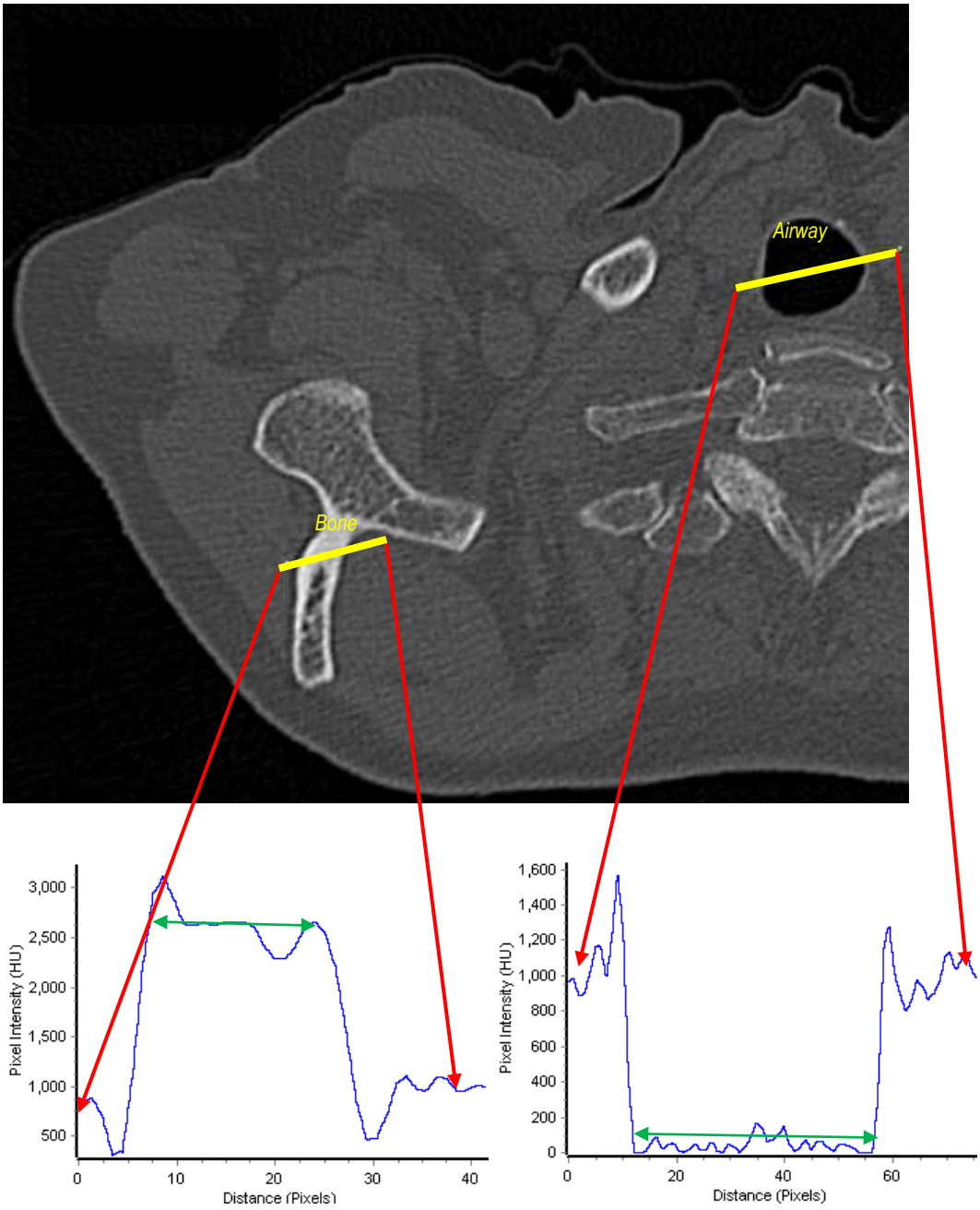

Figure 4.3: HRCT image and pixel profiles used to create reference values

Mean intensity value across pixel profile shown with green arrow.

Commonly available office software (Microsoft Office 2007) was used to create airway simulation data using the reference values from Table 4.1. The *circle* object was used to create 72 simulations of HRCT airways. HRCT structure density was simulated using the nearest available shading values. Therefore, “black less 5 per cent” shading was used to represent near zero density airway lumen and “white, darker 40 per cent” shading was used to simulate airway wall. The *circle* objects were superimposed onto a *rectangle* object set with fill of ‘black, 25 per cent lighter’ shading representing the density of parenchyma (Figure 4.4).

Airway size selection

Circle object size and line point size were varied for each airway allowing the creation of differently sized airway lumen and walls (Figure 4.4). Airway dimensions were converted to millimetres (using the conversion where 1 Didot point = 0.352mm). Sizes were chosen to be representative of airway generations 19 and smaller (Table 4.2).

TABLE 4.2: HUMAN AIRWAY AREAS FOUND AT DIFFERENT GENERATIONS

Airway generation	Count	Lumen diameter (mm)*	Lumen area (mm^2)
25 (trachea)	1	16	201.1
19	6	6.6	25.5
18	8	4.9	18.8
15	20	3.3	8.6
10	85	2.4	4.5
5	499	1.51	1.8
3	1104	0.93	0.7
1	2843	0.79	0.5

** Lumen diameters were obtained from cast of the lung (Horsfield and Cumming 1968)*

The literature does not refer to the range of human airway wall dimension measurements, so for each row of airways, the airway wall thickness was systematically varied. In Table 4.3 it can be seen that increasing the wall line thickness reduced the lumen diameter. This encroaching of the wall resulted in a negative lumen diameter in row f, which necessitated removal of these artifacts from the simulated model in Figure 4.4.

TABLE 4.3: SIMULATED AIRWAY AREAS

Model airway row	Lumen point size (mm)	Wall thickness range (mm)		Resulting LD range (mm)	
A	6	9.0	1.5	5.5	2.8
B	5	5.0	1.5	4.5	3.2
C	4	5.0	1.5	3.5	2.2
D	3	5.0	1.5	2.5	1.2
E	2	5.0	1.5	1.5	0.2
F	1	5.0	1.5	0.5	-0.8
G	2	1.0	0.1	2.0	1.6
H	1	1.0	0.1	1.0	0.6
I	0.5	1.0	0.1	0.5	0.1

The image was converted to a 12-bit 512x512 bitmap. The calibration line as shown in Figure 4.4 was 442 pixels and measured as 73.2mm, allowing the calculation of the pixel x-y size as 0.1629mm and the field of view of 88.3mm.

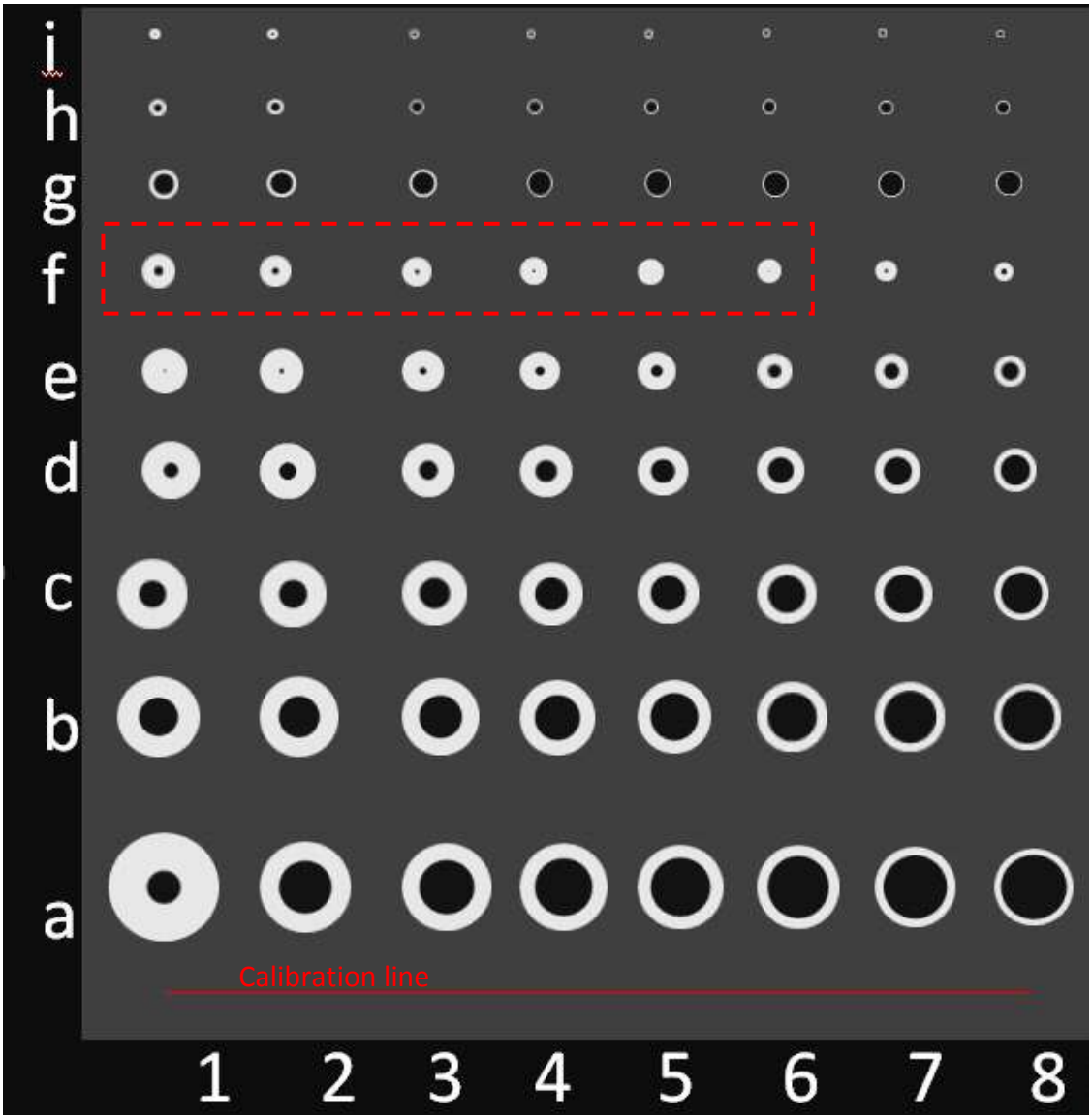

Figure 4.4: Image of the HRCT airway simulation data

High density airway walls (white), low density lumen (black) and parenchyma external to airway (gray). A numbering system 1 to 8 horizontally and A to I vertically was used to identify airways. Airways 1f to 6f bounded by red dashed box were excluded due to overlapping airway wall artifact.

The 67 remaining airways had a wide distribution of airway areas (Figure 4.5A) with LA ranging from 23.5mm^2 to 0.1mm^2, OWA ranging from 45.1mm^2 to 0.2mm^2 and WA ranging from 33.2mm^2 to 0.1mm^2. Similarly, a wide distribution of LD from 5.4mm to 0.12mm and OWD from 7.5mm to 0.05mm and WT from 6.2mm to 0.26mm was obtained (Figure 4.5B). The increased number of airways with smaller dimensions

reflected the need to characterise the performance of the algorithm near the limits of detection.

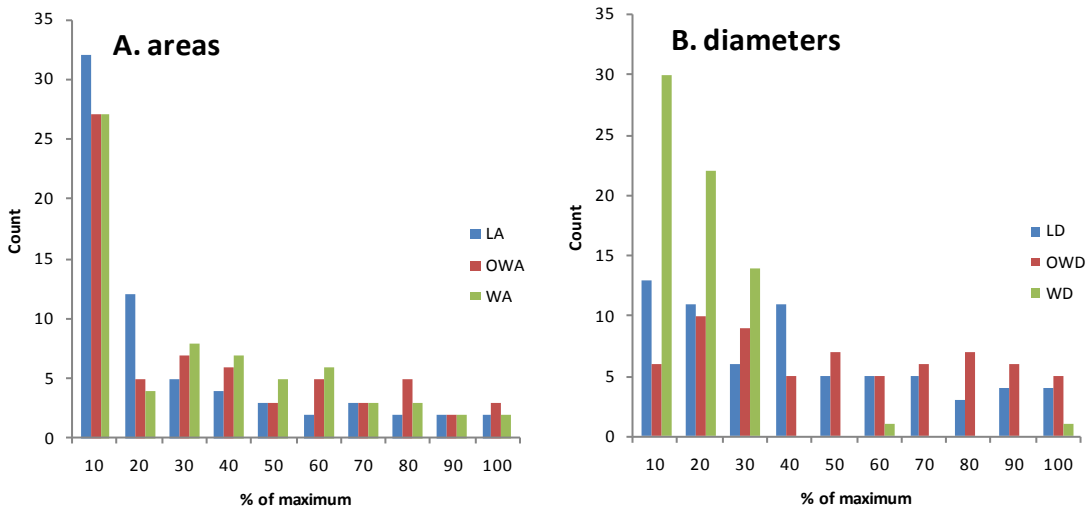

Figure 4.5: Simulation data frequency distributions

(A) LA, OWA and WA areas and (B) LD, OWD and WT in the model data.

4.2.2 Model measurement by CL algorithm

The *winImageBase* software was modified to include methods that allowed the user:

- to change the number of rays cast by the CL algorithm
- to set whether interpolation was ON or OFF during ray-casting. If interpolation was ON, the amount of interpolation per pixel could also be chosen
- to define the edge-detection method as either the maximum gradient (max-grad), or full width half max (half-max).

Bitmaps of the simulated airways (Figure 4.4) were imported into the *winImageBase* software and one CL measurement was made from each airway.

The speed of execution of the CL algorithm from user-initalisation to completion was measured on a desktop PC with an Intel Core 2 Duo 2.33Ghz.

4.2.3 Data manipulation

Settings within *winImageBase* were used to modify parameters such as the mechanism for edge detection, the number of rays cast during edge detection and the degree of interpolation. To determine the effect of rotation, the image data was rotated in 3-D at 15, 30, 45, 60 and 75 degrees using the *Win3D* software (see Section 5.3.1 for description) prior to CL measurement in *winImageBase*. To determine the effect of volume averaging in rotated airways, 2, 4, 6 and 8 rotated adjacent images were

combined in *winImageBase*. To determine if measurement was more precise and accurate on straightened airways, averaged and rotated data was re-rotated back to orthogonal prior to measurement in *winImageBase*.

Statistical analysis

Error from actual size was calculated for each individual measurement. Accuracy (bias) was calculated as percentage error in size from true size; negative bias represents measurement under-estimation whereas positive bias represents measurement over-estimation. Individual measurements were grouped by size, allowing calculation of mean bias and standard deviation. Precision (standard error or uncertainty) for each group was calculated as standard deviation divided by the square root of the number of measurements within each group. Groups were compared for significant differences using a paired, two-tailed T-test.

4.3 Results

In each of the following sections the effects of CL algorithm parameter choice on airway measurement accuracy, precision and speed were considered.

4.3.1 Effect of edge-detection method

LA and OWA areas appeared slightly different when comparing the two edge detection methods that were investigated, with the half-max method producing a more true circular approximation of the inner and wall-parenchyma boundaries (Figure 4.6).

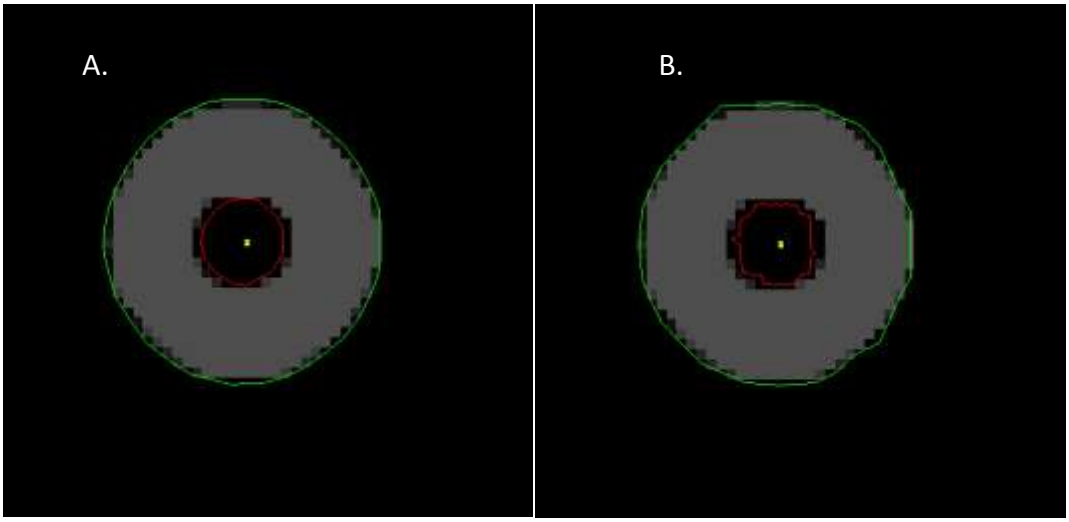

Figure 4.6: Examples of airways measured with different edge detection methods

(A) Half-max and (B) max-grad edge detection methods compared in airway 2D. The airway lumen is outlined in red and wall-parenchyma boundary in green.

However, when the results of the two algorithms were compared, very little difference could be observed in the spread or magnitude of the measurement errors (Figure 4.7A and Figure 4.7B). For the smallest airways OWA and WA were over-estimated and LA was under-estimated by similar amounts. However, with increasing airway size increasing measurement error was noted to occur from the max-grad method, so for instance OWA was increasingly over-estimated with increasing airway size. This contrasted strongly with the half-max method, where no size dependency was observed. Both methods appeared to have increased error spread with increasing airway size. Overall, the max-grad method appears to have a slightly larger spread of errors than the half-max method.

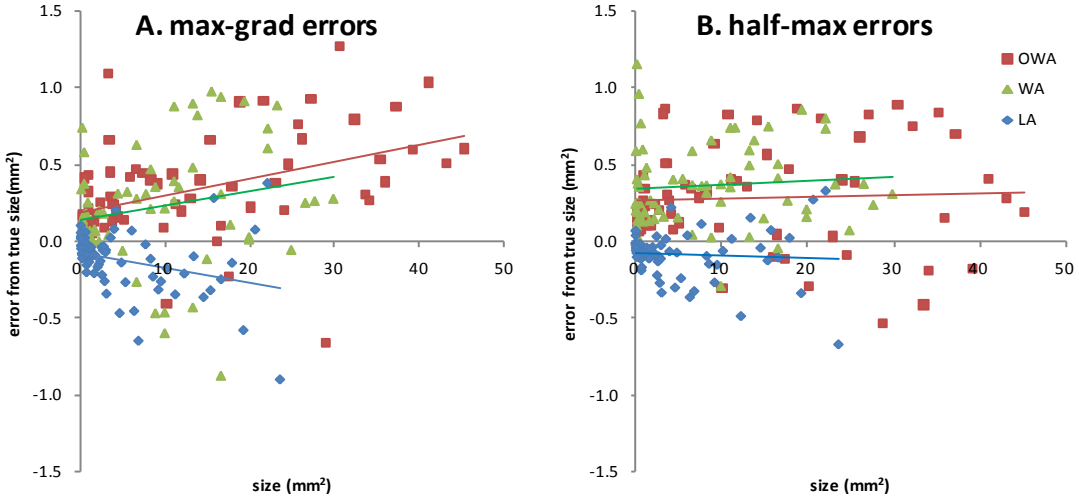

Figure 4.7: Measurement errors from model data

LA, WA, and OWA errors with the two types of edge detection on all 67 measurements with (A) max-grad and (B) half-max methods of edge detection. Results collected using the following CL parameters: 40 rays, interpolation 10 samples/pixel.

To further elicit any differences between the two methods percentage errors were considered in Figure 4.8. In terms of all measurements both algorithms have similar performance, with large bias at small sizes tending towards zero with increasing size. For OWA (Figure 4.8C and Figure 4.8D) and WA (Figure 4.8E and Figure 4.8F) both algorithms have increasing positive bias with decreasing size whereas LA has decreasing negative bias with decreasing size (Figure 4.8A and Figure 4.8B). However with the max-grad method at very small sizes, further size reductions resulted in a swap in the direction of the bias, whereas with the half-max method the bias continues to follow the trend. At very small sizes the LA bias was less than the WA and OWA bias.

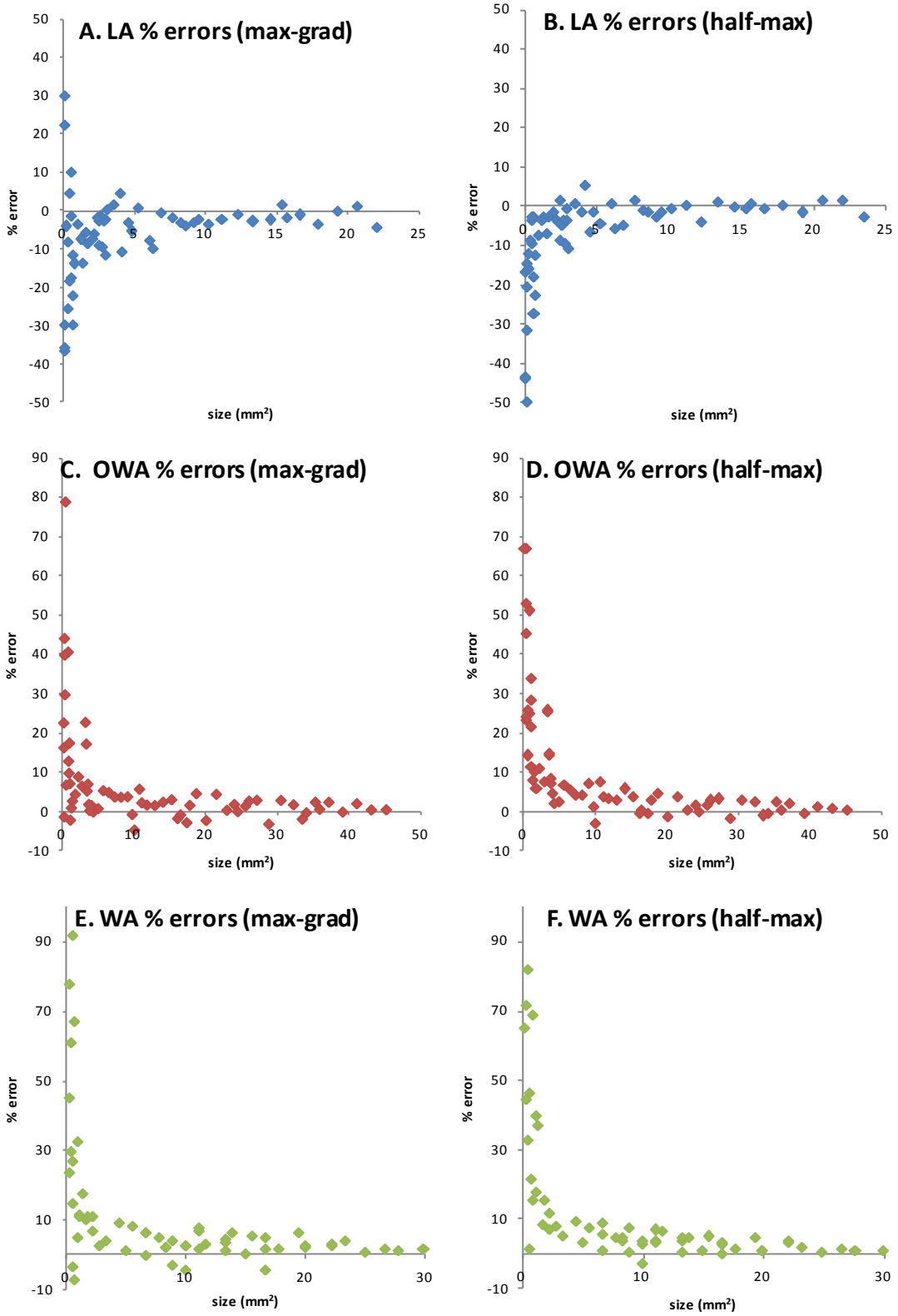

Figure 4.8: Effect of edge-detection method on all percentage errors

Percentage errors from max-grad in (A) LA, (C) OWA, (E) WA and half-max in (B) LA, (D) OWA, and (F) WA on 67 individual measurements. Results collected using the following CL parameters: 40 rays, interpolation 10 samples/pixel.

In Figure 4.9 the relative performance of the two algorithms are considered on all the measurements as a group. Overall, both algorithms underestimate LA and overestimate OWA and WA (Figure 4.9A). LA is measured with more precision than OWA and WA by both methods. When tested for significance between these algorithms no difference was found. Overall LA bias was close to zero with both methods (Figure 4.9B), with the max-grad method having more uncertainty. OWA bias was positive for both methods, with similar levels of uncertainty. Both methods measured WA with a relatively small positive bias and high precision.

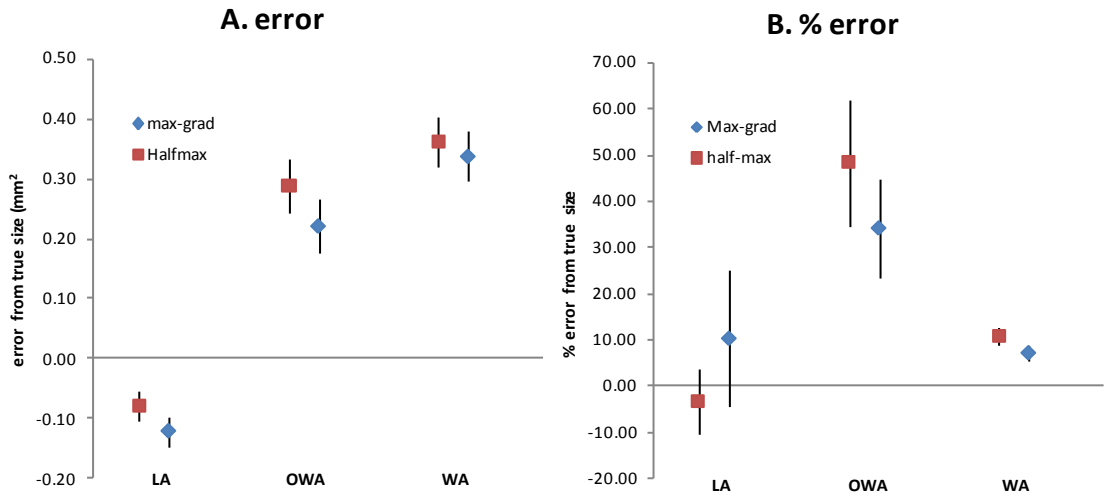

Figure 4.9: Effect of edge-detection method on mean errors

(A) Mean LA, WA, and OWA errors and (B) % errors with the two types of edge detection on all 67 measurements. Results collected using the following CL parameters: 40 rays, interpolation 10 samples/pixel. Results presented with error bars representing ± standard error.

In Figure 4.10 the results have been grouped by size, allowing further investigation of size-dependency in the measurement error. When the LA percentage errors obtained from the two edge detection methods were tested using a two-tailed, unpaired T-test, no significant difference ($p>0.05$) was found (Figure 4.10A). On comparing the OWA results obtained from the two methods, no significant difference was found except for the smallest group ($p=0.019$) (Figure 4.10B). Similarly, when WA results were tested all differences were non-significant except for the smallest group ($p=0.0004$).

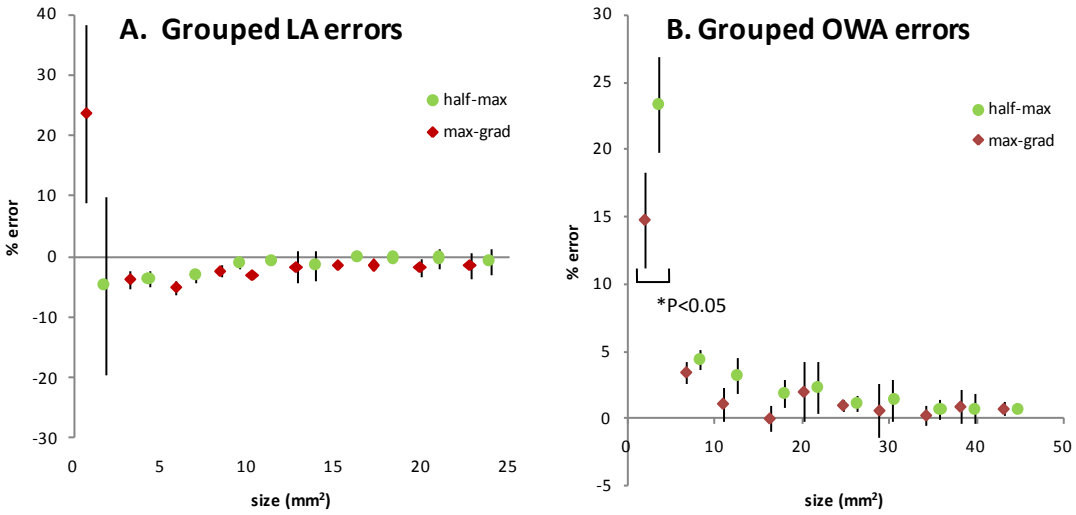

Figure 4.10: Effect of edge-detection method on mean errors (grouped)

(A) Mean LA and OWA errors and (B) % errors in model data with the two types of edge detection on all 67 measurements presented with error bars representing standard error. Results collected using the following CL parameters: 40 rays, interpolation 10 samples/pixel.

To investigate why these significant differences occur in the smallest group, this group was separated into 10 subgroups based on the lumen diameter so they could be examined further (Table 4.5). The max-grad method appeared to produce a similar bias irrespective of airway size whereas the half-max method tended towards increased under-estimation with decreasing size. However, with the max-grad method there were much larger increases in the uncertainty with decreasing size.

TABLE 4.4 COMPARISON OF LA BIAS AND UNCERTAINTY IN THE SMALLEST AIRWAYS

Mean LA (mm^2)	Mean LD (mm)	Half-max method		Max-grad method	
		Mean % error	Standard error	Mean % error	Standard error
0.01	0.2	175.30	245.74	-5.51	1008.94
0.07	0.4	-26.46	21.47	-4.46	59.64
0.18	0.6	-31.29	9.68	-4.04	57.64
0.42	0.8	-9.34	2.74	-1.94	41.69
0.62	1.0	-12.91	4.62	-1.56	584.00
0.86	1.2	-15.10	7.76	-2.29	1.61
1.26	1.4	-3.33	0.39	-1.09	5.77
1.64	1.6	-4.89	2.11	-1.14	42.35
2.22	1.8	-1.94	1.24	-1.10	5.11
2.80	2.0	-6.05	1.43	-1.57	5.02

4.3.2 Effect of interpolation

With increasing airway size, similar airway size-dependent trends were observed in LA and OWA bias irrespective of the amount of interpolation (Figure 4.11A and Figure 4.11C). Over the size ranges tested, the max-grad method produced a large under-estimation of LA and OWA if no interpolation was used. However, this negative bias was markedly reduced by using 1 interpolation per pixel. Furthermore, with increasing sampling frequency of the interpolation there was a trend of decreasing bias, although this difference rapidly tailed off with increasing interpolation, to the point where the difference between 40 and 100 samples/pixel appeared very small.

LA and OWA uncertainty followed similar trends in both LA and OWA (Figure 4.11B and Figure 4.11D), with a similar baseline uncertainty being achieved at all but the smallest grouping. This baseline's uncertainty was largely unaffected by interpolation. However, much higher uncertainty was observed in the smallest airways group, especially with LA uncertainty. Interestingly, interpolation appeared to have the reverse effect on LA uncertainty as compared to OWA uncertainty. Increased LA uncertainty was observed with increasing interpolation.

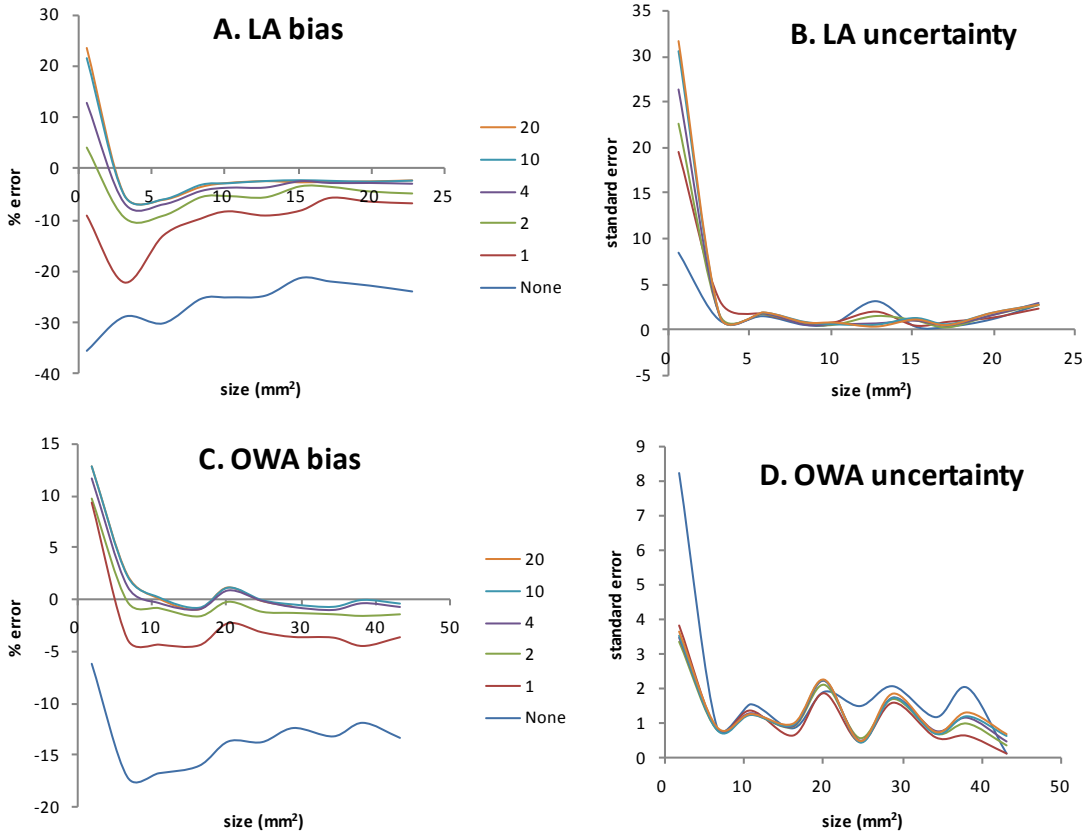

Figure 4.11: The effect of various degrees of interpolation on model data

(A) mean LA bias, (C) mean OWA bias, (B) LA uncertainty, (D) OWA uncertainty. Grouped measurements in model data with all 67 airways. Results collected using the following CL parameters: 40 rays, max-grad edge detection.

4.3.3 Effect of number of rays

On examination screenshots of simulated airway images overlaid with measurements, ray number did appear to have an effect on LA and OWA measurement (Figure 4.11). Increasing ray number appeared to produce a more true circular approximation of the inner and wall-parenchyma boundaries and hence a more accurate approximation of the areas being measured.

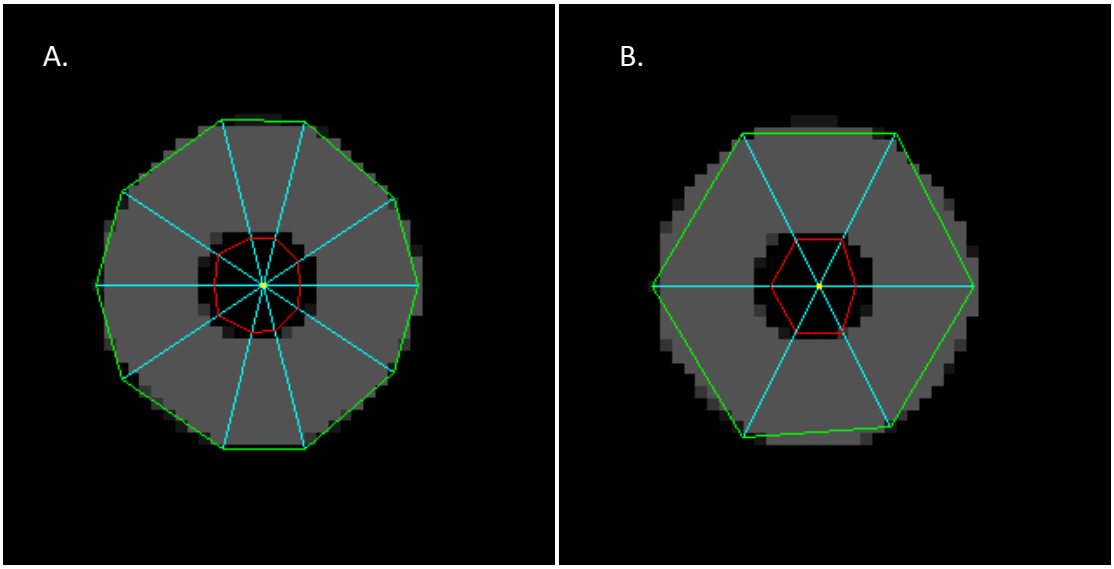

Figure 4.12: Example screenshots of airways measured with different numbers of rays

(A) Ten and (B) six rays with max-grad edge detection in airway 2D. In images the airway wall appears grey. Rays (blue) from the centroid (yellow) pass to the ROI (not shown). The LA is calculated as the area spanned by the vertices (red) obtained from joining the measured airway lumen boundary as measured at each ray. Similarly OWA is calculated by joining the vertices as defined (green) by measuring the wall-parenchyma boundary.

This observation was confirmed when LA and OWA bias were examined. Decreasing ray number increased the under-estimation of both LA (Figure 4.13A) and OWA (Figure 4.13C). The pattern of the bias introduced from reducing the number of rays was similar to that from interpolation but was much larger in magnitude than the interpolation bias. Similar to the bias results from interpolation, the LA and OWA uncertainty did not appear to be affected by ray number, except in the smallest group where there was a much greater degree of uncertainty (Figure 4.13B and Figure 4.13D).

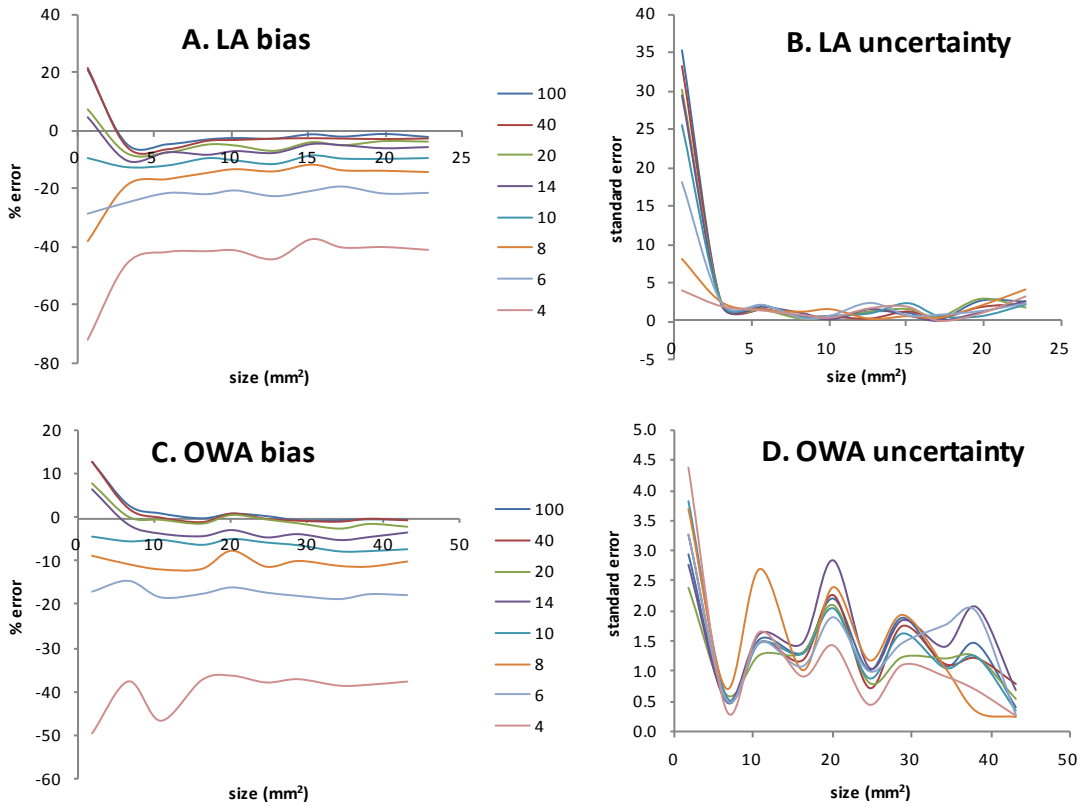

Figure 4.13: The effect of ray number on bias and uncertainty on model data

(A) mean LA bias, (C) mean OWA bias, (B) LA uncertainty, (D) OWA uncertainty. Grouped measurements in model data with all 67 airways. Results collected using the following CL parameters: 40 rays, max-grad edge detection.

In Table 4.5 the bias from largest airway group is compared against the theoretical deduced bias as shown in Figure 4.2. Excellent agreement with the theory was found in all cases, with difference in bias of less than 2 percent.

TABLE 4.5: OWA RAY NUMBER BIAS COMPARED TO THEORETICAL PERCENTAGE ERRORS

number of rays	% theory error	% actual error	% difference
4	-36.3	-37.6	1.3
6	-17.3	-17.6	0.3
8	-10.0	-10.0	0
10	-6.5	-7.3	0.8
14	-3.3	-3.2	-0.1
20	-1.6	-2.2	0.6
40	-0.4	-0.4	0
100	-0.1	-0.5	0.4

4.3.4 Algorithm speed of execution

The effect of edge detection was firstly assessed on all 67 airways by measuring the time taken to perform each of the tasks involved in making a measurement, namely:

- centroid identification
- airway segmentation
- drawing annotations and overlaying segmentation results.

The method chosen for edge detection appeared to have no effect on the time taken to perform centroid identification or airway segmentation (Figure 4.14). Centroid identification took longer than airway segmentation for airways at any size. Drawing of the results was constant at 0.1 second. For very small airways centroid identification took a relatively smaller proportion of the total time taken, since airway segmentation was fairly invariant to the effects of increasing ROI size.

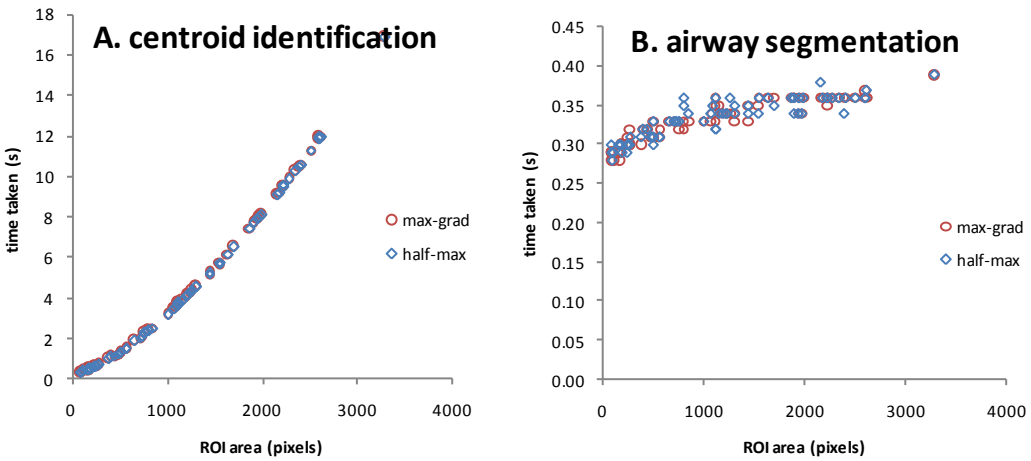

Figure 4.14: Time taken to make a single measurement using CL algorithm

Results collected using the following CL parameters: 40 rays, 10 samples/pixel.

Next, the effect of ray number was quantified. Centroid identification took much longer than drawing, which took longer than airway segmentation. Increasing the ray count caused proportional increases in the time taken to perform each of the tasks (Table 4.6). However, since the centroid identification took so much longer, the effect of increasing ray number on the total time taken was much larger.

TABLE 4.6 EFFECT OF RAY COUNT ON TIME TAKEN IN SECONDS IN AIRWAY A2

Ray count	Centroid identification	Airway segmentation	Drawing
100	11.89	0.08	0.27
40	4.74	0.04	0.10
20	2.41	0.03	0.06

Finally, the effect of interpolation on CL algorithm speed was quantified (Table 4.7). Interpolation has no effect on centroid identification or on drawing the results, but a large effect on airway segmentation. With increasing interpolation there were proportional increases in time taken to segment the airways. Since airway segmentation takes up a very small proportion of the total time taken, the effect of interpolation on total time taken was small.

TABLE 4.7 EFFECT OF INTERPOLATION ON TIME TAKEN IN SECONDS IN AIRWAY A2

Ray count	Centroid identification	Airway segmentation	Drawing
20	4.72	0.09	0.10
10	4.71	0.06	0.10
8	4.71	0.06	0.10
6	4.71	0.04	0.10
4	4.71	0.04	0.10
2	4.72	0.03	0.10
1	4.70	0.03	0.10
0	4.73	0.02	0.10

4.4 Discussion

Since Nyquist sampling theory (Nyquist 1928) states that approximately 2.3 pixels are required across a structure for its detection, the minimal detectable diameter for any structure to be measured in this simulated data set is approximately 0.32mm. Structures of less than this value are not theoretically detectable, so they could have been excluded from the analyses. This would have reduced the number of lumen measurements to 66 and wall measurements to 49.

Structures below the minimum detectable limit were not removed because it was important to quantify the CL algorithm performance below these limits. HRCT scanning technology is currently undergoing a revolution; although existing scanners currently cannot exceed 0.25mm *x-y* dimensions, this is likely to improve greatly in the near future.

4.4.1 Effect of edge detection

The two edge-detection methods appear to have broadly similar performance in most of the airways tested. Both methods perform accurately in larger airways, with a bias less than 5 per cent for measuring airways in most cases.

Small airways

With relatively small airways (for instance with LA between 1mm^2 and 10mm^2) there was an under-estimation in LA with both methods, which can be attributed to the errors in the estimation of the centroid position. Inaccurate placement of the centroid in small lumen airways potentially increases the baseline intensity value from which all the rays are cast. With both methods, if the pixel value at the wall is less than the value at the centroid for some rays, then these rays will not find the wall boundary. Any rays that cannot find the wall boundary are set to zero length and an under-estimation in the lumen area will result.

When the methods were given the task of measuring airways close to the minimum detectable size, they performed in very different ways. The max-grad method became less precise but maintained its overall accuracy, whereas the half-max method retained its precision but lost its accuracy. The max-grad method had both negative and positive bias randomly occurring in these small sized airways, resulting in a less precise measurement at small airway size. This is in agreement with the findings of previous studies using the half-max method (Reinhardt, D'Souza et al. 1997; Nakano, Whittall et al. 2002), who found loss of accuracy in thinned walled structures with this method. The max-grad edge detection may be more sensitive than the half-max method to noise across the smaller centroid–wall differential found in thinner wall structures (Reinhardt, D'Souza et al. 1997; Vasiljevic and Khalil 2008).

A high degree of precision is required since the clinician must have confidence in the algorithm's repeatability and since inaccurate measurements can be easily corrected for by calibrating the measurement, it is of less concern than reduced precision. For these reasons the method recommended for edge detection is the half-max.

However, the differences observed between the half-max and max-grad performance warrant further exploration since the number of airways with very small dimensions in this study was small, and it was not possible to test for significant differences between these small groups.

To improve the algorithm, a more accurate method of determining the centroid is required—such as a modified mass centroid or ray casting with interpolation methods.

However, both these methods have problems. The modified mass centroid method relies on a flood-fill inside one of the airway's boundaries, which may not be reliably found, making it more suitable for a 'quick and dirty' assessment. Ray casting with interpolation has a high processing overhead and will slow the CL algorithm, making this the approach to take where accuracy is paramount.

4.4.2 Effect of interpolation

This study observed that any form of interpolation was beneficial to measurement accuracy and precision. This benefit was observed across all airway sizes but was most marked in the smaller airways groups. This was because when there was no interpolation the placement of each ray was subjected to a stepping effect, causing a loss of precision in estimation of the rays' position and therefore the position of the wall. With one interpolation per pixel, the exact intensity value of any point within a pixel can be better estimated using the relative contributions of the surrounding pixels. This resulted in a much better approximation of the ray's intensity than with no interpolation. With greater degrees of interpolation, benefits to observed errors were also obtained but the benefits were reduced in magnitude. The optimal amount of interpolation was 10 samples per pixel, since this provided a good improvement with a relatively small increase in computation time.

This study presented one form of interpolation with the max-grad edge detection. Other forms of interpolation, such as bi-cubic or tri-linear, may better represent the true airway wall boundary, allowing for improved accuracy at smaller sizes. The current study found decreasing precision with increased interpolation with very small airways using the max-grad method. This is because the edge-detection method depended on the wall thickness, which is not directly taken into account with the simulated data. To better understand the effects on interpolation on edge detection a more detailed study is required where the wall thickness is kept constant.

4.4.3 Effect of number of rays

Increasing the number of rays reduces bias by better approximating the true boundary of the airway walls (Figure 4.12). However, the effects of increasing ray number rapidly diminished after a certain point in accordance with the theory presented earlier in the chapter.

The optimal number of rays is 40; increasing the number of rays beyond this provides little or no further reduction to the CL algorithm's measurement bias. Although the effect of ray numbers could effectively be countered in all cases by applying the correction equation, this equation makes the assumption that the airway is an

idealised circular structure presented orthogonally. Real airways do not present in this way, and therefore a larger number of rays might better allow for airways that are not circular.

This comparison of the results with theoretical bias assumes that all airways are large. With smaller airways, this agreement may not be as good, since parameters errors will start to have a greater effect. These errors include those arising from the edge-detection method, as was discussed in the previous section.

4.4.4 Speed of execution

The ray-casting part of the algorithm was fast, and largely unaffected by the size of the ROI, whereas the centroid identification part of the algorithm was by-far the slowest to execute. Centroid identification execution time could be reduced by using region growing to create a segmented area inside the lumen and a mass centroid calculation to identify the centre of this segmentation. However the robustness of this adaptation and its effect on centroid estimation accuracy and precision has yet to be established (Tschirren, Hoffman et al. 2004).

Now that optimal parameters have been determined for idealised 2-D airways, the techniques developed during this chapter for exploring accuracy and precision will be used as a foundation for testing the CL algorithm performance in 3-D data in Chapter 6.

CHAPTER 5

Handling confounders

Having established that half-max was the edge-detection method of choice, this chapter examines the effect of confounders on CL algorithm performance. The CL algorithm was tested on a 3-D version of the simulated data presented in Chapter 4, after the addition of some of the known confounders found in HRCT data.

Modelling the common problem of airway orientation, simulated airways were presented at different orientations to the scanner by rotating them in three dimensions before assessing the performance of the algorithm. To simulate another problematic effect — volume averaging in angled airways (Hopper, Iyriboz et al. 1998) — the rotated dataset was averaged to various degrees, before assessing the performance of the algorithm. In both cases, the effect of the confounder was compared before and after the application of theoretical correction equations.

Lastly, to determine whether the performance of the algorithm could be improved by rotating the airways back to orthogonal before measurement, the rotated and averaged data was re-rotated back to orthogonal prior to measurement.

Before investigating the ways these confounders affect the algorithm's performance, the theoretical effects of angle change and volume averaging are now considered.

5.1 Angle theory

As reported by (King, Muller et al. 2000), when an airway is rotated relative to the scanning plane, the measured lumen diameter and thus the measured lumen area increases. This area can be calculated in an idealised circular airway as the deviation from circular to elliptical (Figure 5.1).

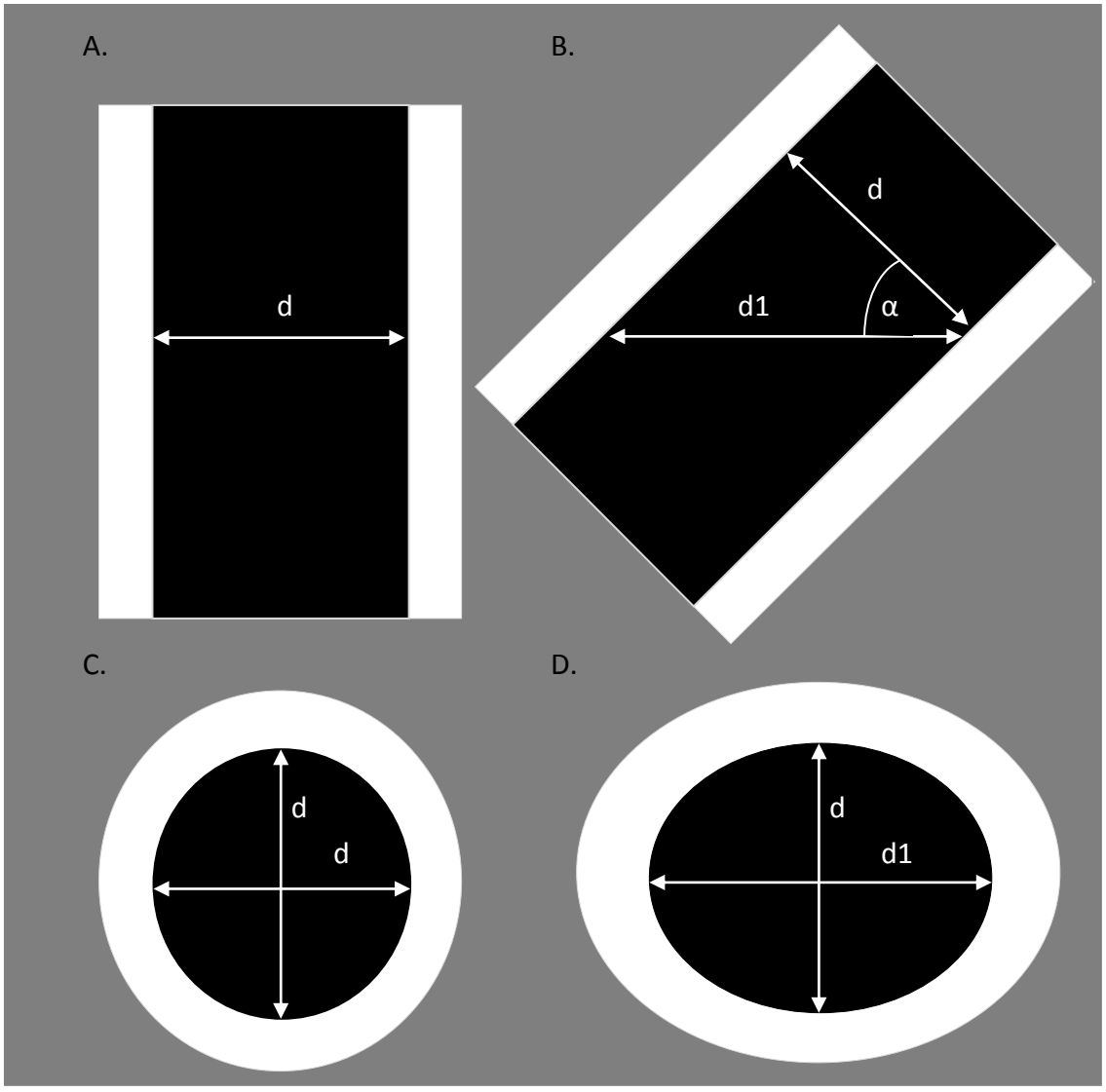

Figure 5.1: An idealised circular airway undergoing rotation

Airway lumen (black) and wall (white) superimposed onto parenchyma (grey) with true lumen diameter d and measured diameter d1 at angle α. (A) longitudinal orthogonal, (B) longitudinal rotated, (C) transverse orthogonal, and (D) transverse rotated views.

If we rotate this airway by angle α, the diameter d in the measurement plane becomes $d1$. The true lumen area LA is now measured as lumen area $LA1$.

Hence,

$$cos\ \alpha = \frac{d}{d1}$$

Therefore the measured diameter:

$$d1 = \frac{d}{cos\ \alpha} \quad \textbf{(5.1)}$$

Substituting this value into the equation of a circle, $A=\pi r^2$, where *r* is the radius of the lumen, the measured lumen area can be expressed:

$$LA1 = \pi . \frac{d}{2\cos\alpha} . \frac{d}{2} \quad \textbf{(5.2)}$$

Similarly if rotation occurs in both planes, the measured lumen area can be expressed:

$$LA1 = \pi . \frac{d}{2\cos\alpha} . \frac{d}{2\cos\beta} \quad \textbf{(5.3)}$$

Assuming the airway is circular and no other effects are present, we can state the measured lumen area *LA*1 in terms of the actual area *A* as follows:

$$LA1 = \pi . \frac{\sqrt{A/\pi}}{\cos\alpha} . \frac{\sqrt{A/\pi}}{\cos\beta} \quad \textbf{(5.4)}$$

where α and β are the angles to the scanning plane.

Since area and radius measurements are proportional in Equations (5.3) and (5.4), we can state that percentage change in area is equal to percentage change in radius. Similarly, it follows that when measuring wall area or wall thickness, the percentage change is always the same.

Eliminating π, measured lumen area can be expressed simply when only one angle changes:

$$LA1 = \frac{A}{\cos\alpha} \quad \textbf{(5.5)}$$

Similarly, if rotation occurs in both planes, the measured lumen area is:

$$LA1 = \frac{A}{\cos\alpha . \cos\beta} \quad \textbf{(5.6)}$$

5.1.1 Effect of angle theory

As the angle of rotation increases the airway lumen area is increasingly over-estimated (Figure 5.2). If the angle in one plane is kept at zero and the angle in the other plane is increased, the measured area doubles at an angle of 60 degrees and triples at an angle of 75 degrees. If the angle in both planes changes then this over-estimation is compounded, so that if both angles are 75 degrees the area is over-estimated approximately 14-fold.

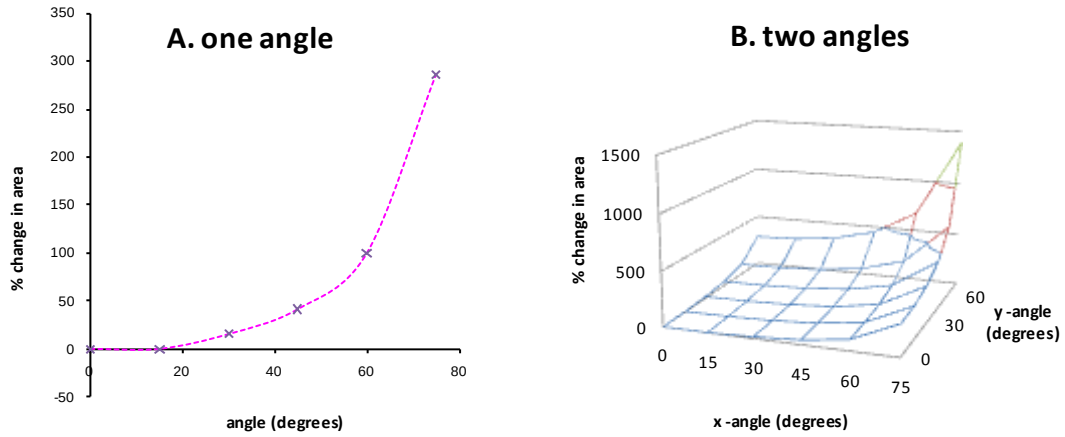

Figure 5.2: Theoretical effect of angle change on airway area

(A) one angle using Equation (5.5) and (B) two angles using Equation (5.6).

5.2 Volume averaging theory

In addition to the effect of angle change, an additional consideration with HRCT data is volume averaging, which takes place due to averaging in the *z*-axis in 3-D data. Volume averaging is always present in 3-D data, however the extent of its effect is particularly apparent in HRCT data, since the image's *z* resolution is often poor relative to the *x* and *y* resolution. Because each voxel is made up of a large amount of *z*-dimensional surrounding material this problem manifests as excessive blurring of structures in otherwise relatively high resolution images.

In Figure 5.3, obtaining measurements with and without volume averaging is considered. Figure 5.3A shows the idealised situation of a rotated airway where the *y*-*z* plane of each voxel is exactly bisected by the airway wall boundary. When the two-dimensional pixel profile of the rotated airway is taken (that is, with no volume averaging), the calculated value at each pixel is made up from either containing only lumen or wall or parenchyma. Since the edge-detection method of the CL algorithm finds the point at which half the maximum intensity occurs, the airway wall is measured at exactly two pixels in diameter in both cases.

However, if the 3-D voxel profile (that is, with volume averaging) is considered (Figure 5.3C), then the calculated value at each voxel is made up of contributions of more than one structure. For instance, in Figure 5.3C the airway wall voxels are reduced in value because they are made up of 7/8 wall and 1/8 lumen or parenchyma. This blurring of the wall intensity into the surrounding structures causes the walls to appear larger.

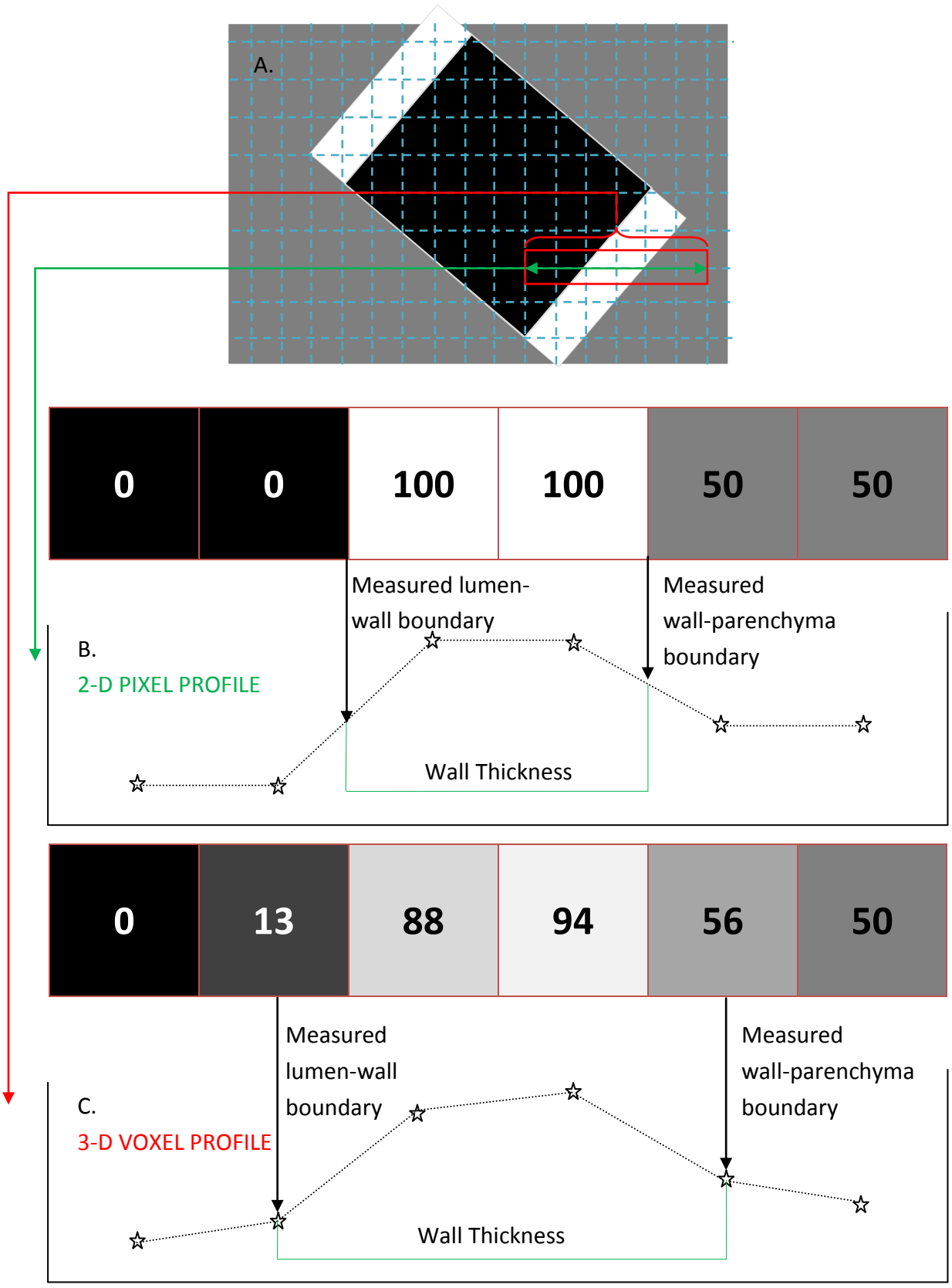

Figure 5.3: Partial volume effects in longitudinal rotated airway

Longitudinal airway section (A) with voxel grid (blue) superimposed, 2-D pixel profile along green line (B) and 3-D voxel profile across red area (C) from pixel/voxel intensity allowing estimation of inner and outer airway wall. In (C) volume averaging effect has altered lumen-wall and wall-parenchyma boundary positions by ½ pixel/voxel width in both cases.

In Figure 5.4 the lumen-wall boundary position is under-estimated by $\frac{L}{2}$ because the edge-detection method of the CL algorithm finds the point at which half the maximum intensity occurs, that is, half-way along *L*. Similarly, the wall-parenchyma boundary position is over-estimated by $\frac{L}{2}$ because the point at which half the maximum intensity occurs is found is exactly half-way along *L*. Since these effects occur in both walls, lumen diameter will be under-estimated by *L*, and outer wall diameter over-estimated by *L*.

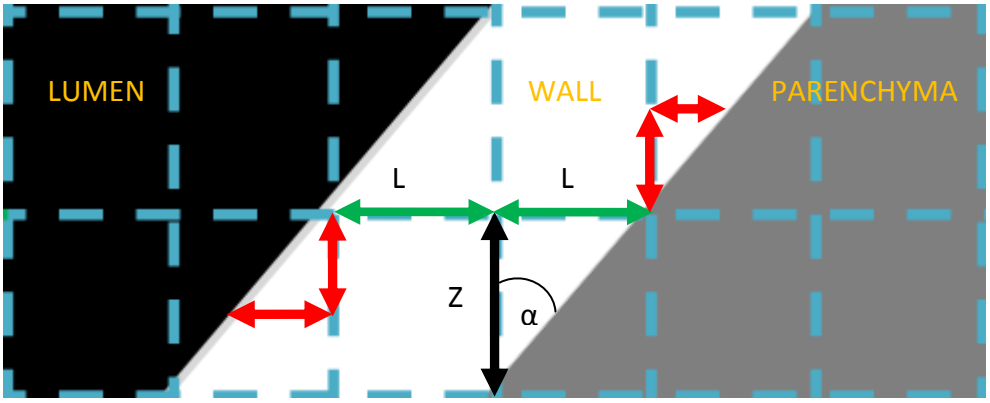

Figure 5.4: Idealised airway wall section illustrating calculation of volume averaging effect

Voxel grid (blue) representing dimensions (x, y, z) as (L, L, Z). Angle of rotation as α. Contribution of volume averaging (red) to measured wall thickness (green).

From Figure 5.4, since $tan\ \alpha = \frac{L}{z}$

$$L = z.tan\ \alpha \tag{5.7}$$

where α is angle of rotation.

Therefore, substituting into Equation (5.1), measured lumen area is:

$$LA1 = \pi\ .\ (Lrx - \frac{z.tan\ \alpha}{2})\ .\ (Lry - \frac{z.tan\ \beta}{2}) \tag{5.8}$$

Where *Lrx* and *Lry* are the radii of the lumen in each plane.

Similarly, measured outer wall area is:

$$OW1 = \pi\ .\ (Wrx + \frac{z.tan\ \alpha}{2})\ .\ (Wry + \frac{z.tan\ \beta}{2}) \tag{5.9}$$

where *Wrx* and *Wry* are the radii of the outer wall in each plane.

With increasing angle, an increasing under-estimation of the lumen area and an increasing over-estimation of outer wall area are obtained (Figure 5.5). With higher *z*-axis resolution, the relative contribution of volume averaging error to the overall error

is less. Therefore, at small *z*-dimension, the volume averaging-induced error is small even at large angles. However, when rotation has occurred in two angles then the error is compounded. Comparing the effects of volume averaging to angle theory effects (Figure 5.2), it can be seen that the contribution of volume averaging to overall error is less than that of angle theory.

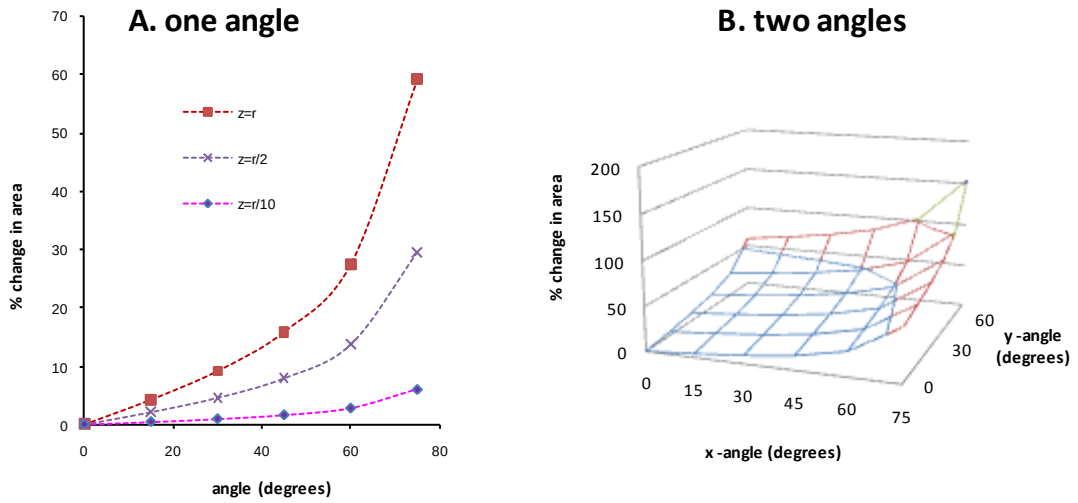

Figure 5.5: Theoretical volume averaging effect on airway area

(A) one angle and (B) two angles on area with z=r.

5.2.1 Combined effect of confounders

Since we have already established with angle theory the true radius of the airway, we can substitute into Equation (5.8) values for *r1* and *r2*, where:

$$rx = \frac{d}{2\cos\alpha} \qquad ry = \frac{d}{2\cos\beta}$$

Therefore, the measured lumen area can be expressed:

$$LA1 = \pi.\left(\frac{d}{2\cos\alpha} - \frac{z.\tan\alpha}{2}\right).\left(\frac{d}{2\cos\beta} - \frac{z.\tan\beta}{2}\right) \qquad \textbf{(5.10)}$$

Expressing this in terms of the true *LA*, the measured lumen area is as follows:

$$LA1 = \pi.\left(\frac{\sqrt{LA/\pi}}{\cos\alpha} - \frac{z.\tan\alpha}{2}\right).\left(\frac{\sqrt{LA/\pi}}{\cos\beta} - \frac{z.\tan\beta}{2}\right) \qquad \textbf{(5.11)}$$

Since the volume-averaging effect is small relative to the angle effect for any one angle, the combined effect is similar to the angle effect alone (Figure 5.6). Increasing *z*-dimension has increasing effects on the over-estimation, but in the quantities examined here, even at large angles, the change in error is small.

Furthermore, the volume-averaging effect is additive to the angle theory effect in outer wall area and reductive to the angle theory effect in lumen area, a larger spread in over-estimation is found when comparing lumen, outer wall, and wall area errors. Lumen over-estimation is much smaller than outer wall area over-estimation. With increasing angle, both effects combine to increase the over-estimation of OWA, whereas they counter each other in LA estimation. Since WA is obtained by subtracting LA from OWA, the OWA over-estimation is partially countered.

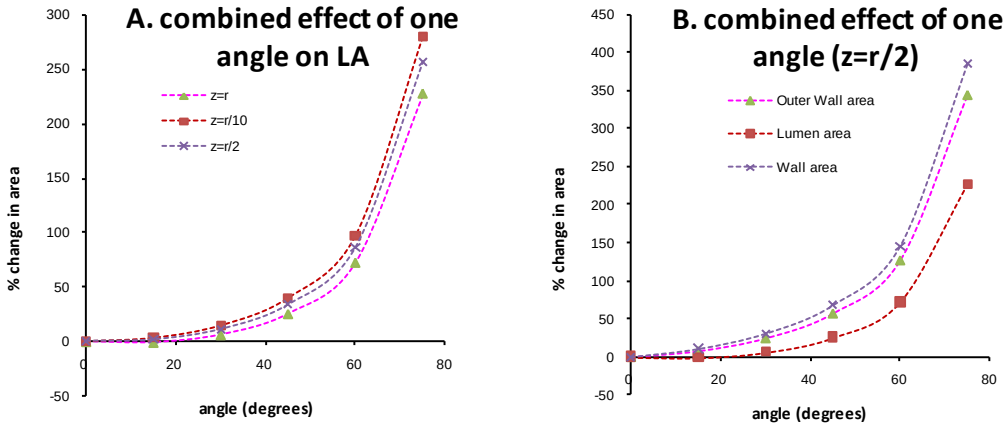

Figure 5.6: Combined volume averaging and angle theory effect

(A) Effect of angle change on lumen airway area with various z-dimension and (B) lumen, outer wall, and wall areas at constant z.

5.3 Methods

Investigation of the effects of angle and volume averaging used the simulated data produced in Chapter 4. It required new software for three-dimensional rotation and measurement using the CL algorithm. These steps are presented below.

5.3.1 Software

A custom MS-Windows *C++* software program was created for these experiments. Briefly, the *win3D* software incorporated a tri-linear interpolation algorithm, allowing rotation of any three-dimensional dataset from any point in three dimensions. Three viewing windows allowed the data to be visualised in *x-y*, *x-z* and *y-z* orientation. Post-rotated datasets were saved in the same format as the original, allowing the data to be easily imported into and measured by the *winImageBase* software. Datasets were averaged in various *z* dimensions by reading the density information of each of the adjacent voxels in each image.

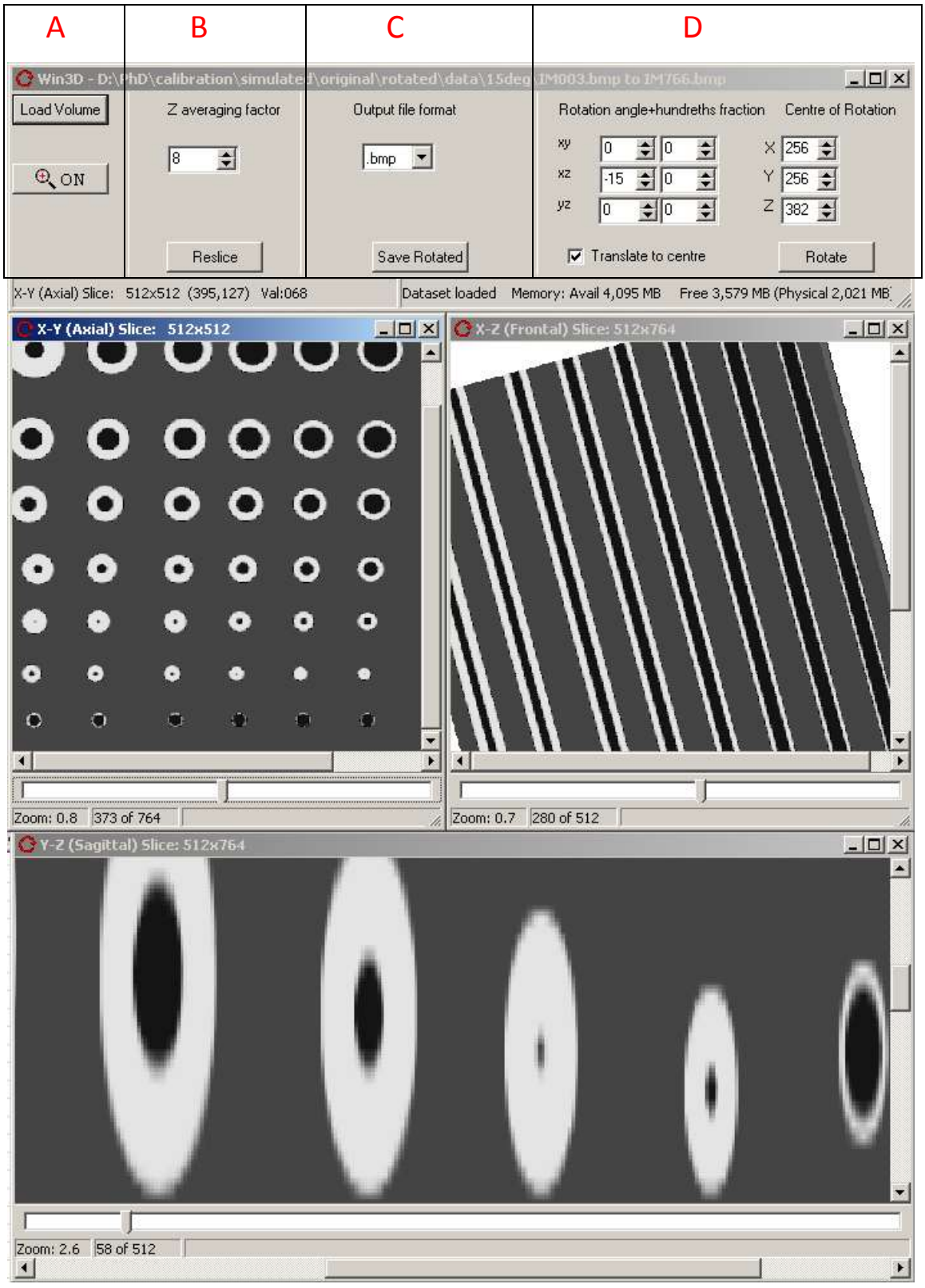

Figure 5.7: Win3D software screenshot showing airway simulation data in rotation

Three views of 512x512x764 volumetric dataset rotated at 15 degrees are presented to the user. Each view has been zoomed [using the zoom button], panned [using the scrollbars] and traversed [using the trackbar at the bottom of each view]. Functions are grouped into 4 categories: (A) loading and manipulating a dataset, (B) averaging and reslicing the data, (C) saving the data in various formats, (D) rotating the data in three dimensions.

5.3.2 Data manipulation

To determine the effect of rotation on airway measurement, the image data was rotated in 3-D at 15, 30, 45, 60 and 75 degrees in the *x*-z plane using the *win3D* software (Figure 5.7). The images were saved in bitmap format, and then imported into *winImageBase* for CL algorithm measurement.

To determine the effect of volume averaging in rotated airways, pixels from between two and eight adjacent images were averaged and saved using *winImageBase*. To determine if measurement was better on straightened airways, averaged and rotated data was re-rotated in 3-D back to orthogonal before measurement in *winImageBase*.

The 67 airways present in the model dataset were separated into 10 groups based on LA, OWA and WA. Example airway images from representative groups were taken directly from *winImageBase* as screenshots.

5.3.3 Statistical analysis

Error from true size was calculated for each individual LA, WA and OWA measurement. Bias was calculated as percentage error in size from true size; negative bias represented measurement under-estimation whereas positive bias represented measurement over-estimation. Individual measurements were grouped by size, allowing calculation of mean bias and standard error (uncertainty) for each group. The group measurements were compared for significant differences using unpaired, two-tailed T-tests.

5.3.4 Model measurement by CL algorithm

The bitmap data was imported into the *winImageBase* software. For each of the airways a ROI was selected and one CL measurement was made from each. The image data was saved as 8-bit bitmap. One hundred (100) identical images were created, simulating a 3-D data set.

5.4 Results

In each of the following sections screenshots of three example airways are presented before and after the application of volume averaging and airway rotation. These airways are representative of the large and small airway groups in terms of LA, OWA and WA. Graphs showing the LA, OWA and WA bias and uncertainty at various angles and how these change with volume averaging were then considered. The effect of

applying correction equations was calculated and finally the relative contributions of the LA and OWA bias and uncertainty to WA bias and uncertainty were examined.

5.4.1 Effect of rotation

When the images of the rotated airways were examined, rotation caused the airways to appear elliptical with larger airway lumen and walls (Figure 5.8) as expected. The greater the rotation angle the greater this effect appeared to be. Furthermore, with increased angle there was increased blurring of the airway walls both into the airway lumen and into the surrounding space.

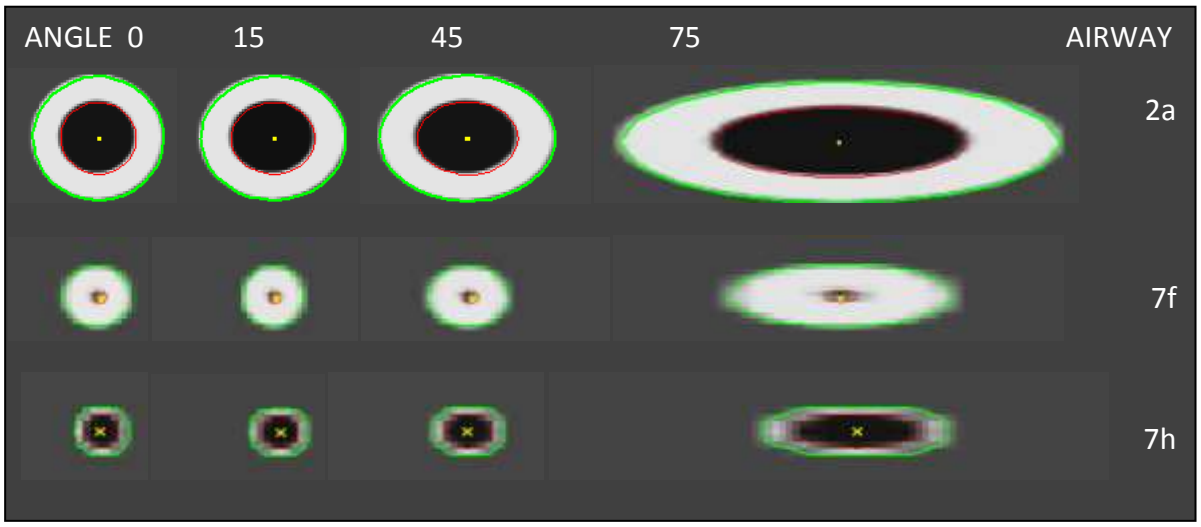

Figure 5.8: Example screenshots of airways showing the effect of rotation

Three airways: 2a (top), 7f (middle) and 7h (bottom) were rotated to 0, 15, 45, 75 degrees (left to right). Algorithm measurements are superimposed on the airways as follows: centroids shown in yellow, lumen-wall boundary in red, wall-parenchyma boundary in green.

The algorithm measurements followed the contours of the wall boundaries well, with the blurring having little or no visible effect on the wall position.

These observations were confirmed when the algorithm measurements were examined (Figure 5.9). There was a similar angle-dependent bias in both LA and OWA, so that at larger angles, greater over-estimation took place (Figure 5.9A and Figure 5.9C). However, there was no size dependency with either LA or OWA bias, except in the smallest sized groups.

For example, with OWA there were size-dependent increases in bias below approximately 8mm^2 (Figure 5.9C), so that the bias in smaller airways moved from near zero to progressively larger with decreasing OWA. For LA, there were size-

dependent decreases in bias from approximately 8mm^2 (Figure 5.9A), so that smaller airways were progressively under-estimated.

When examining the LA and OWA uncertainty size dependency (Figure 5.9B and Figure 5.9D) it was observed that in both cases they rapidly converged to near zero at similar sizes to that found with LA and OWA bias. Further increases in size had small effect. In all cases there was angle dependency in the uncertainty, so that increasing angle increases the uncertainty.

The LA and OWA effects combined in WA to reduce size-dependent bias, so that little or no-size dependency could be observed in any of the groups (Figure 5.9E). However, the angle dependency remained at similar levels to that of LA and OWA. WA uncertainty was also similar to LA and OWA uncertainty for a particular size, except for the smaller groups, where WA uncertainty was much smaller (Figure 5.9F).

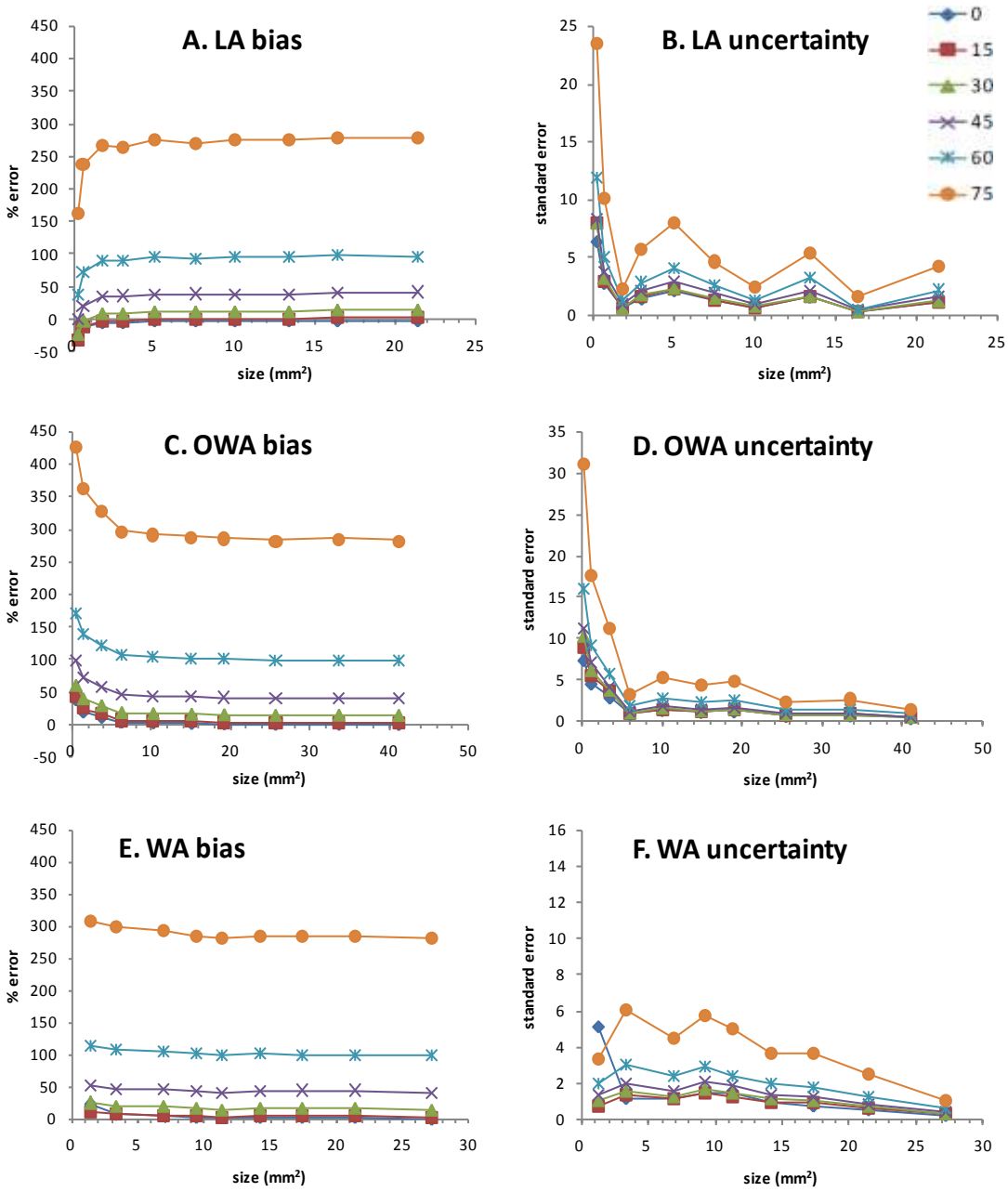

Figure 5.9: Bias and uncertainty before correction

LA, OWA and WA with increasing airway size at 0, 15, 30, 45, 60 and 75 degrees of airway rotation.

Effect of angle theory correction

After the application of the angle theory correction (Equation (5.4)), the angle-dependent bias of the measurements decreased substantially in all cases (Figure 5.10A, Figure 5.10C, and Figure 5.10E). The bias remaining was angle dependent; increased angle resulted in increasing negative bias.

Also, for smaller airways, the remaining LA, OWA and WA bias was still dependent on the size of the structure being measured. Indeed, the smaller groups followed a similar pattern to the corresponding pre-corrected bias (Figure 5.9A, Figure 5.9B, Figure 5.9C).

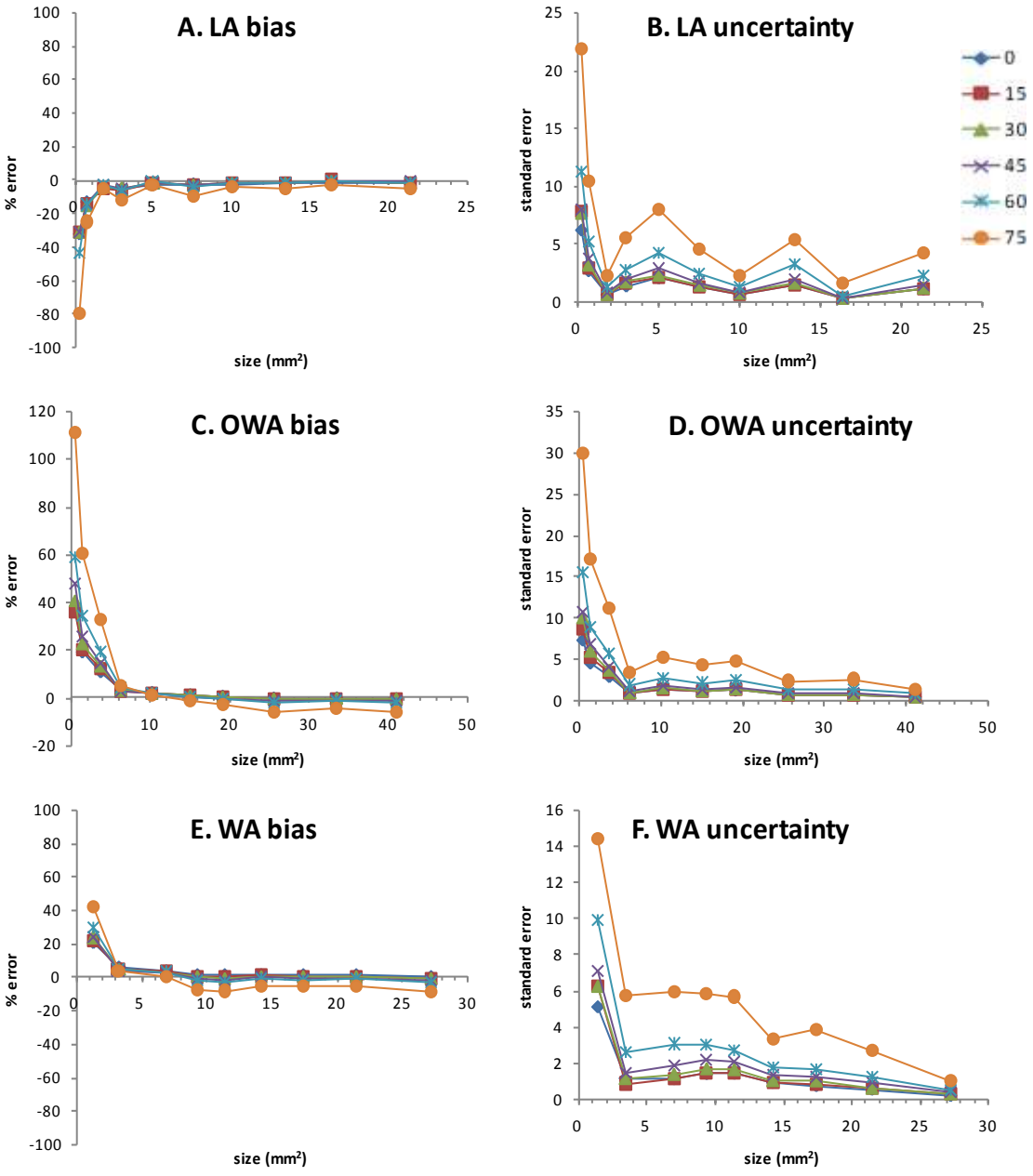

Figure 5.10: Bias and uncertainty after angle correction

LA, OWA and WA with increasing airway size at 0, 15, 30, 45, 60 and 75 degrees of airway rotation.

The uncertainty was largely unaffected by the application of the angle theory correction (Figure 5.10B, Figure 5.10D, and Figure 5.10F). With the smallest group of airways WA uncertainty at all angles was increased after correction.

5.4.2 Effect of volume averaging on rotated airways

Volume averaging was observed primarily as blurring during examination of the rotated and averaged airways (Figure 5.11). At increased rotation angles there was visibly more blurring of the wall boundaries in that plane.

The CL algorithm measurements followed the contours well, except for small airways, where the lumen-wall boundary was sometimes not completely measured. Volume averaging appeared to have a much greater effect on smaller airways than larger ones for any given rotation. In larger airways there was little or no change in estimated wall-parenchyma boundary position whereas, in smaller airways, large increases were observed. In smaller airways this increased the measured airway wall area.

To quantify the effects of volume averaging the second smallest group of airways was selected for further investigation (3.0mm^2 LA and 6.6mm^2 OWA groups). These airways represented the smallest structures that could be expected to be discriminated by the CL algorithm since their diameters were approximately two pixels or over.

Observations from visual inspection were confirmed when the algorithm measurements in these groups were examined (Figure 5.12). Increased volume averaging resulted in reduced positive bias in LA and increased positive bias in OWA (Figure 5.12A and Figure 5.12C). However, these effects were much less than that resulting from increasing angle and mostly occurred in the 75 and 60 degree groups. Increased volume averaging results in increased uncertainty in LA and OWA in all rotated groups: groups at larger angle had greater changes in uncertainty with increasing volume averaging (Figure 5.12B and Figure 5.12D). At angles of 45 degrees and above there was a sigmoidal relationship between LA and volume averaging, whereas for OWA and volume averaging, the relationship was linear.

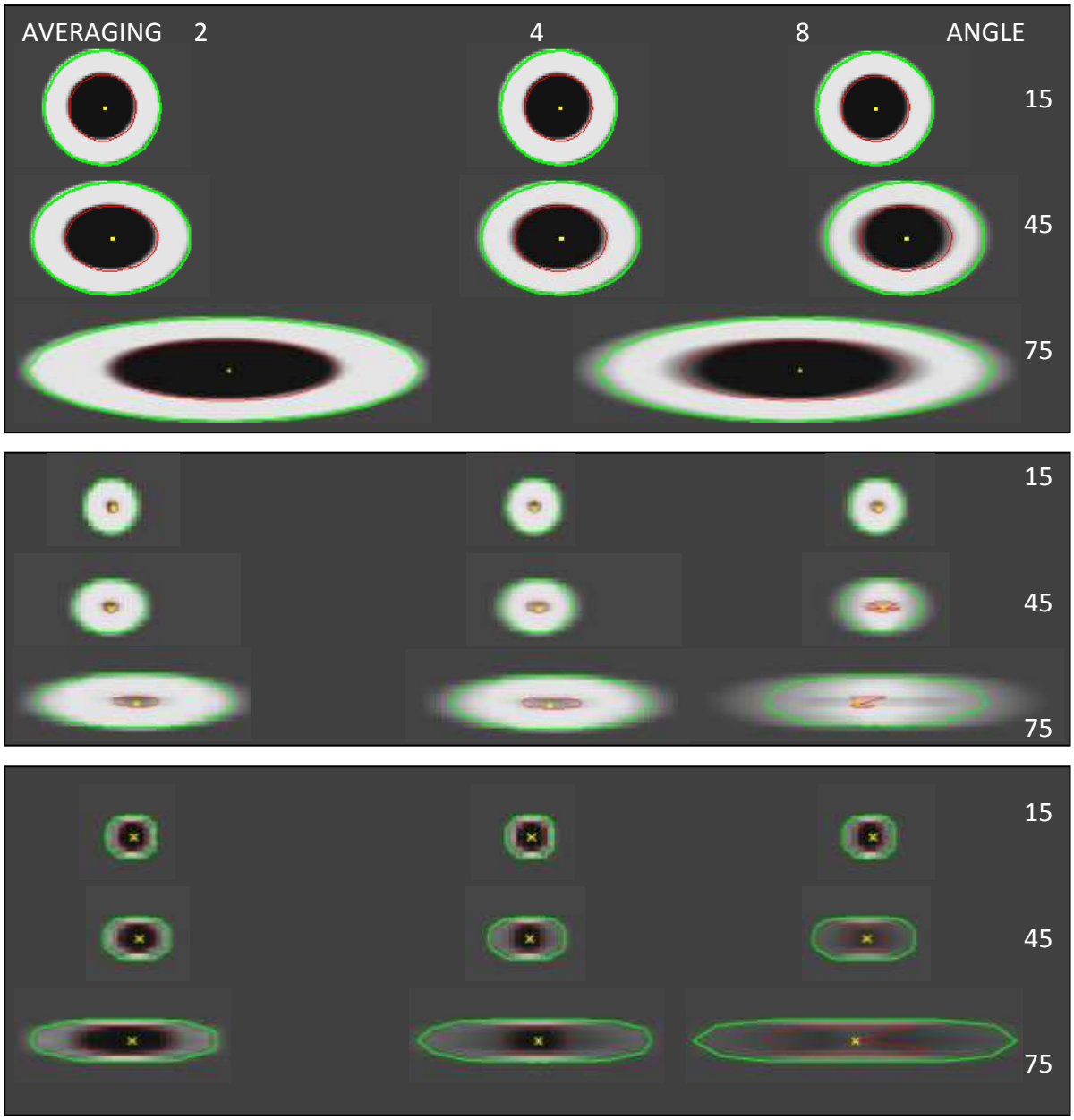

Figure 5.11: Example screenshots of airways showing the effect of volume averaging

Three airways: 2a (top), 7f (middle) and 7h (bottom) rotated at 15, 45 and 75 degrees with averaging of 2, 4 and 8 images. Algorithm measurements are superimposed on the airways as follows: centroids shown in yellow, lumen-wall boundary in red, wall-parenchyma boundary in green.

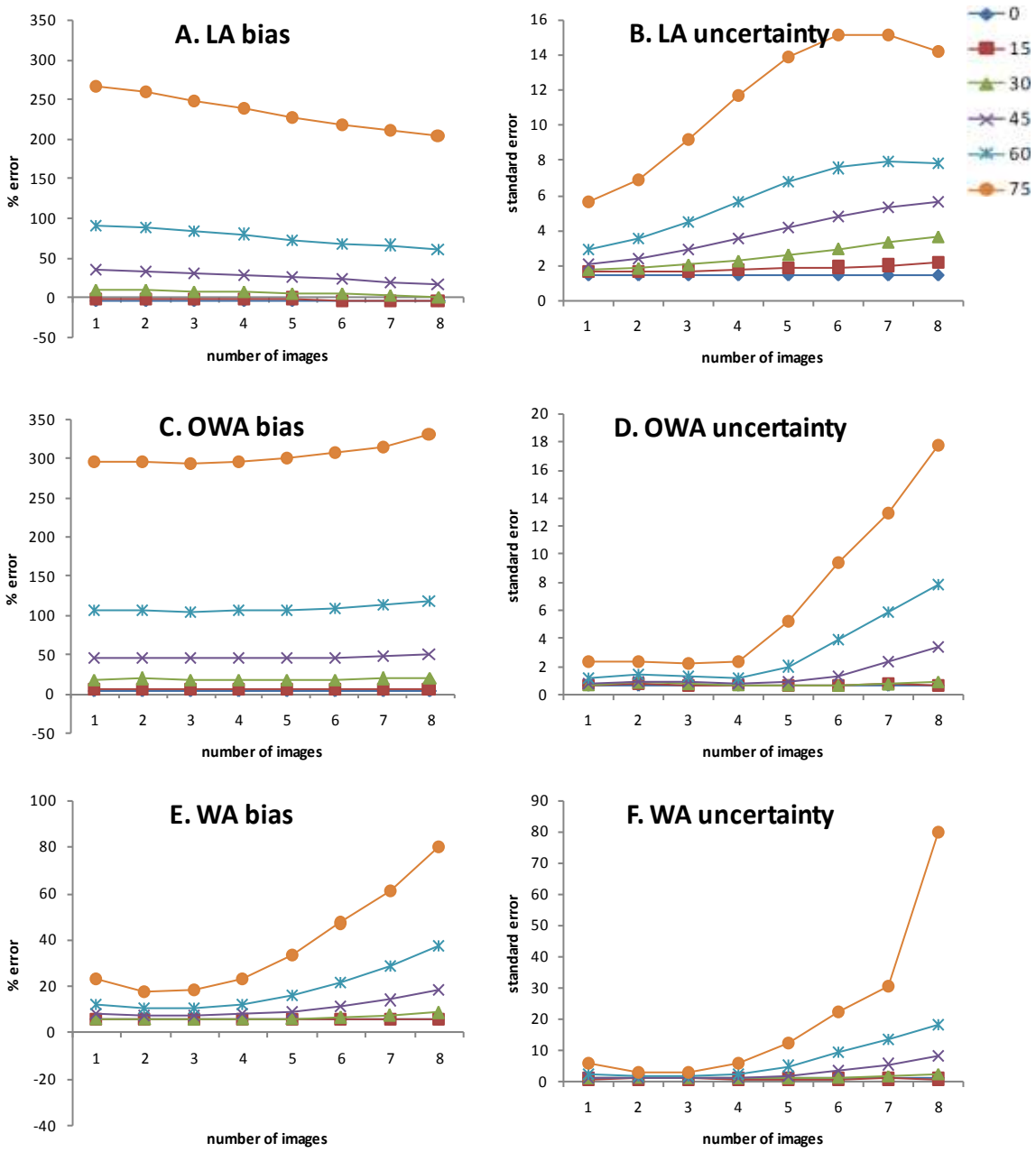

Figure 5.12: Effect of combined angle and volume averaging before correction

LA, OWA and WA bias and uncertainty with increasing averaging of images at 0, 15, 30, 45, 60 and 75 degrees in the 3.0mm^2 LA and 6.6mm^2 OWA grouped data.

Angle theory correction on averaged airways

As with non-averaged images, the application of the angle theory correction reduced the bias in all cases (Figure 5.13). However, the bias that remained after correction with angle theory was larger with averaged airways.

In LA the bias was negative. The magnitude of the bias was dependent on both the degree of volume averaging and the rotation angle (Figure 5.13A). There was a strong linear relationship between the remaining LA bias and volume averaging, with angle

increasing the steepness of the slope. Similar relationships were observed in the OWA estimation, except that the remaining bias was positive rather than negative (Figure 5.13C). These effects combine to increase the bias found in WA (Figure 5.13E).

Application of the angle theory correction equation had no effect on LA or OWA or WA uncertainty (Figure 5.13B and Figure 5.13D and Figure 5.13F), except for airways at WA uncertainty at 75 degrees, averaged at 8 images, where it was reduced.

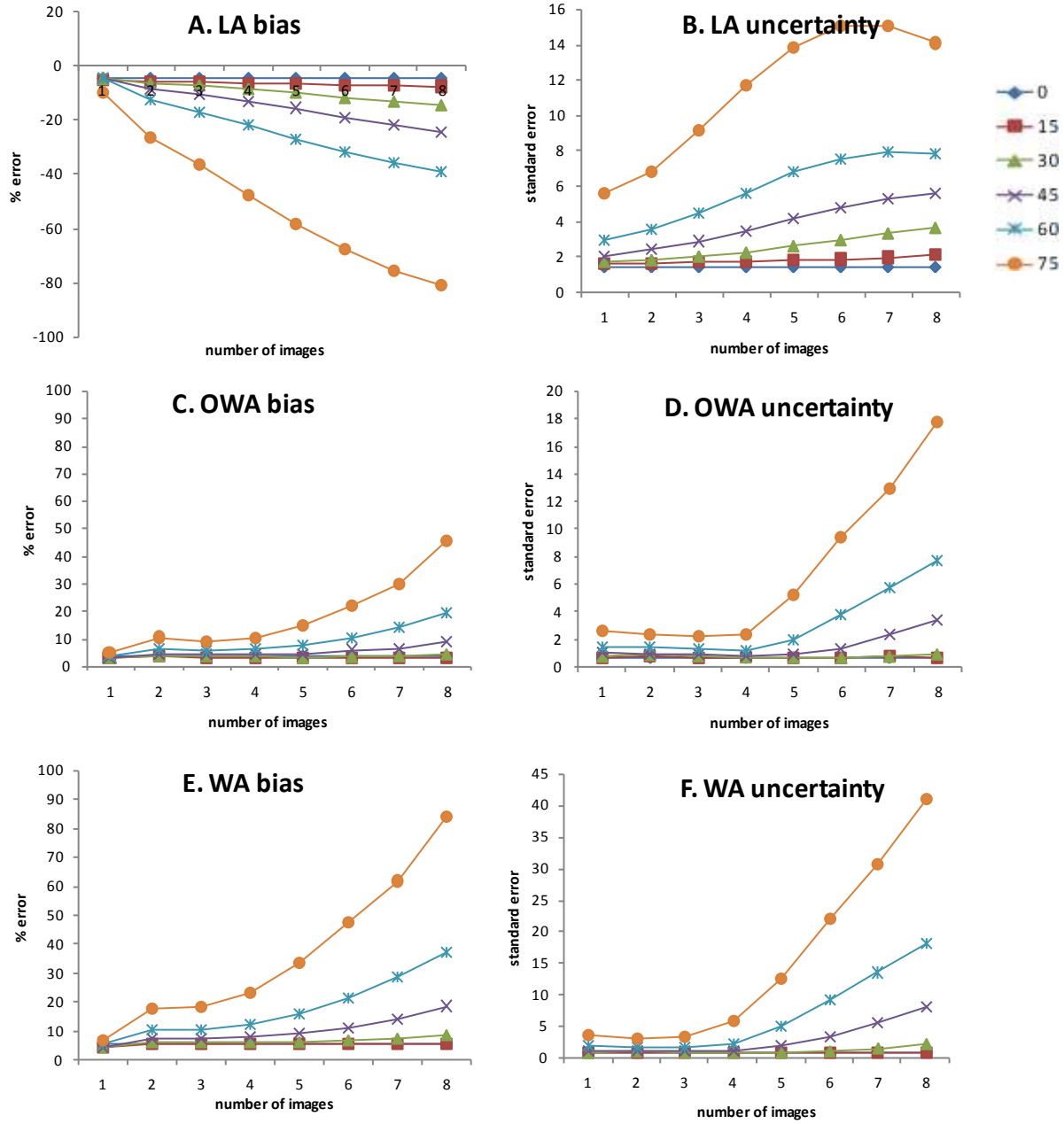

Figure 5.13: Effect of volume averaging after angle theory correction

LA, OWA and WA bias and uncertainty with increasing averaging of images at 0, 15, 30, 45, 60 and 75 degrees in the 3.0mm² LA and 6.6mm² OWA grouped data.

Combined correction on averaged airways

When the effect of angle theory correction (Figure 5.13) was compared to the combined effect of both equations (Figure 5.14), a further decrease in LA and OWA bias was observed—the bias was reduced to less than ± 8% for LA and ± 20% for OWA in all cases (Figure 5.14A and Figure 5.14C). As expected, increasing volume averaging with orthogonal airways (that is, at 0 degrees rotation) did not affect the bias which consistently remained at approximately -3% for LA and 4% for OWA. Similarly, when volume averaging had not been performed, angle had little effect on the corrected algorithm's performance (x=1 in Figure 5.14A and Figure 5.14C). The exception to this was at 75 degrees, where the bias increased to -7% in LA and -16% in OWA.

With increasing angle and volume averaging the remaining LA bias became more positive and the OWA became more negative. The combined effect of both equations on WA was to remove much of the volume averaging-dependent bias. Increasing the rotation angle resulted in increasingly negative bias (Figure 5.14E).

The combination of the two equations had no effect on LA or OWA uncertainty (Figure 5.14B and Figure 5.14D). However, WA uncertainty was reduced (Figure 5.14F), although increasing angle and increasing volume averaging still resulted in increasing uncertainty.

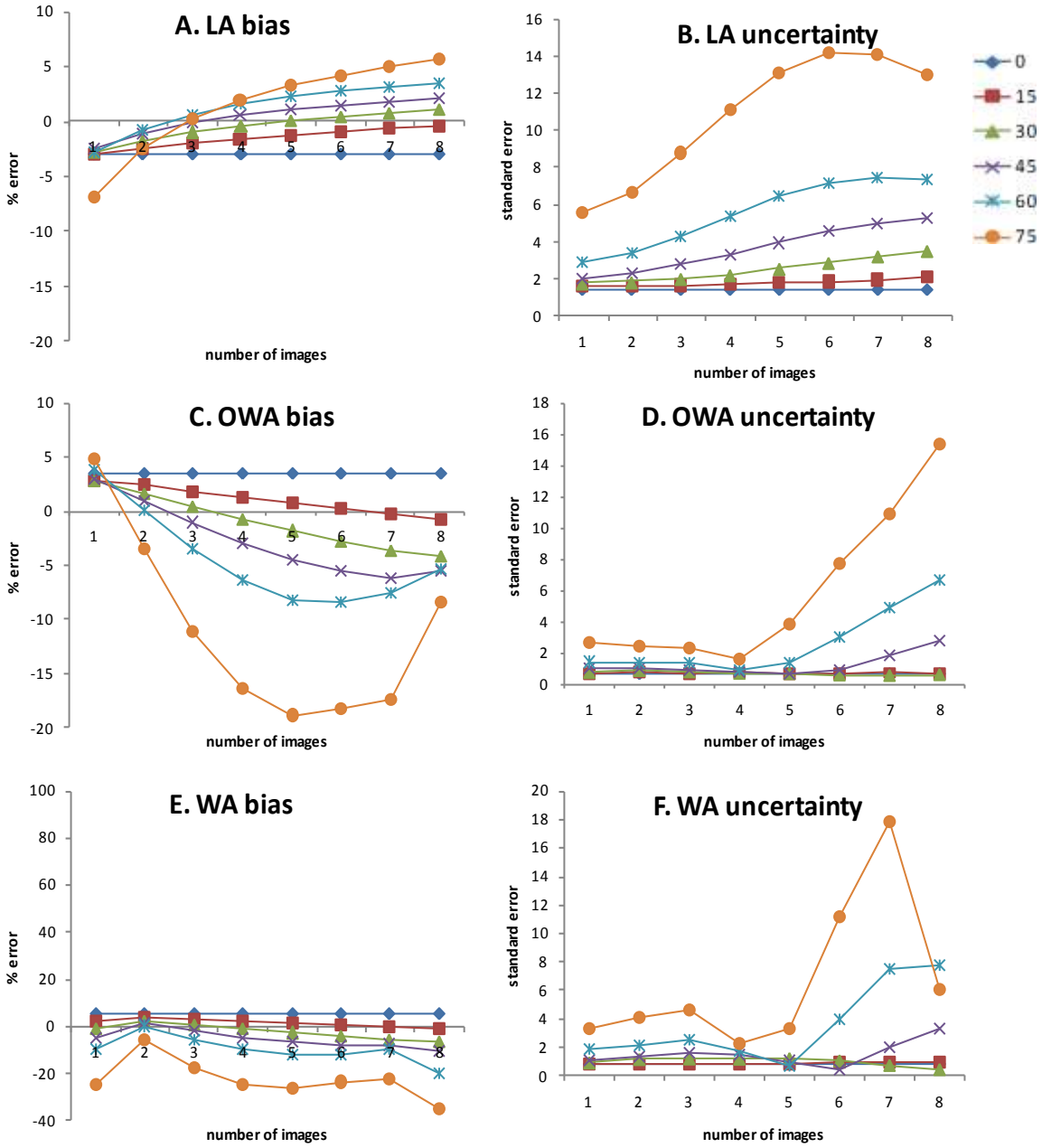

Figure 5.14: Effect of volume averaging after both corrections

LA, OWA bias and uncertainty with increasing averaging of images at 0, 15, 30, 45, 60 and 75 degrees in the 3.0mm² LA and 6.6mm² OWA grouped data.

5.4.3 Measurement after rotation back to orthogonal

To determine the effect of volume averaging on orthogonal airway measurement, the rotated and averaged data was re-rotated back to orthogonal prior to measurement.

Three example airways can be seen in Figure 5.15. Increased volume averaging caused the airway wall to appear blurred over a larger area.

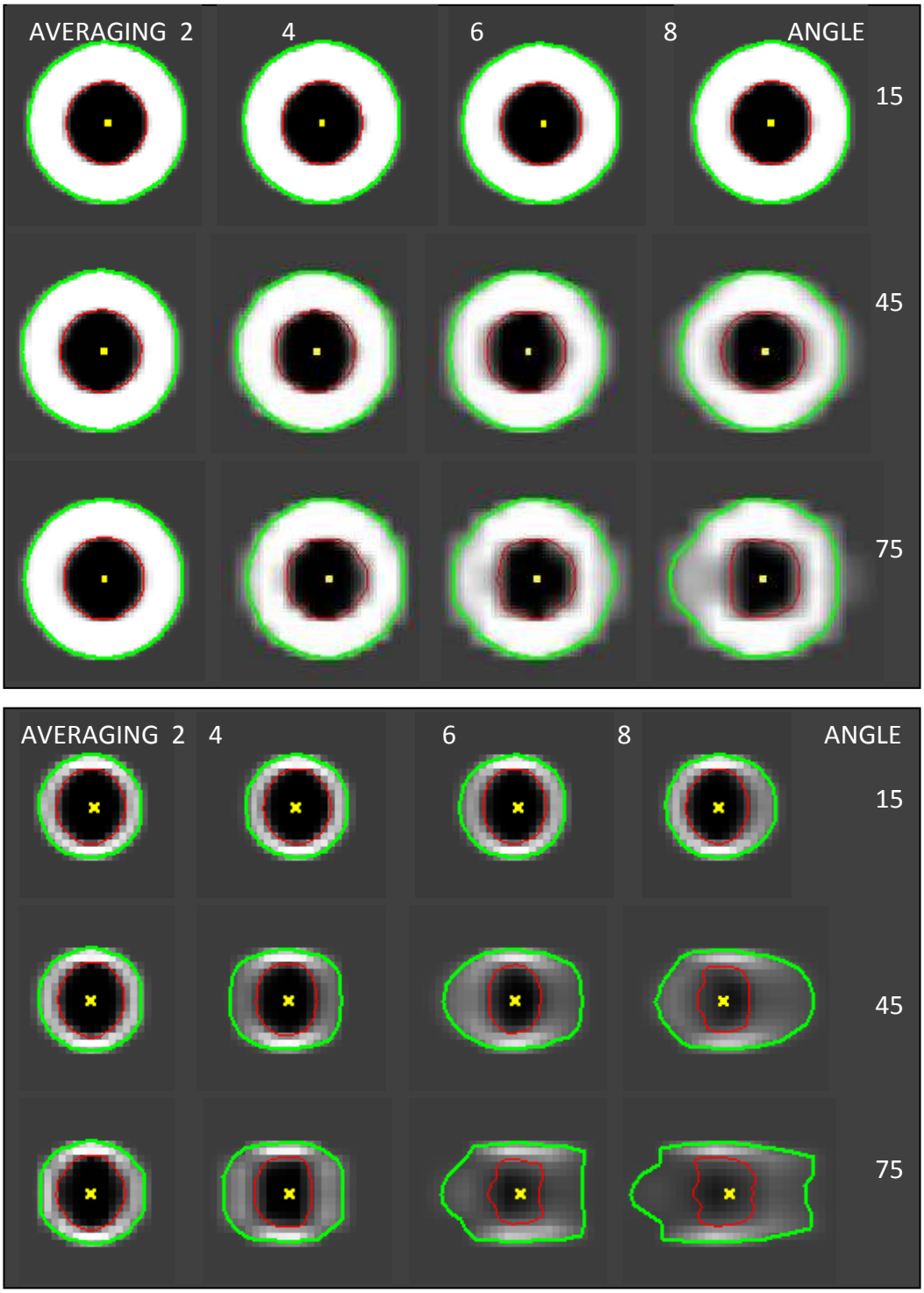
AVERAGING 2
4
6
8
ANGLE
15
45
75
AVERAGING 2
4
6
8
ANGLE
15
45
75

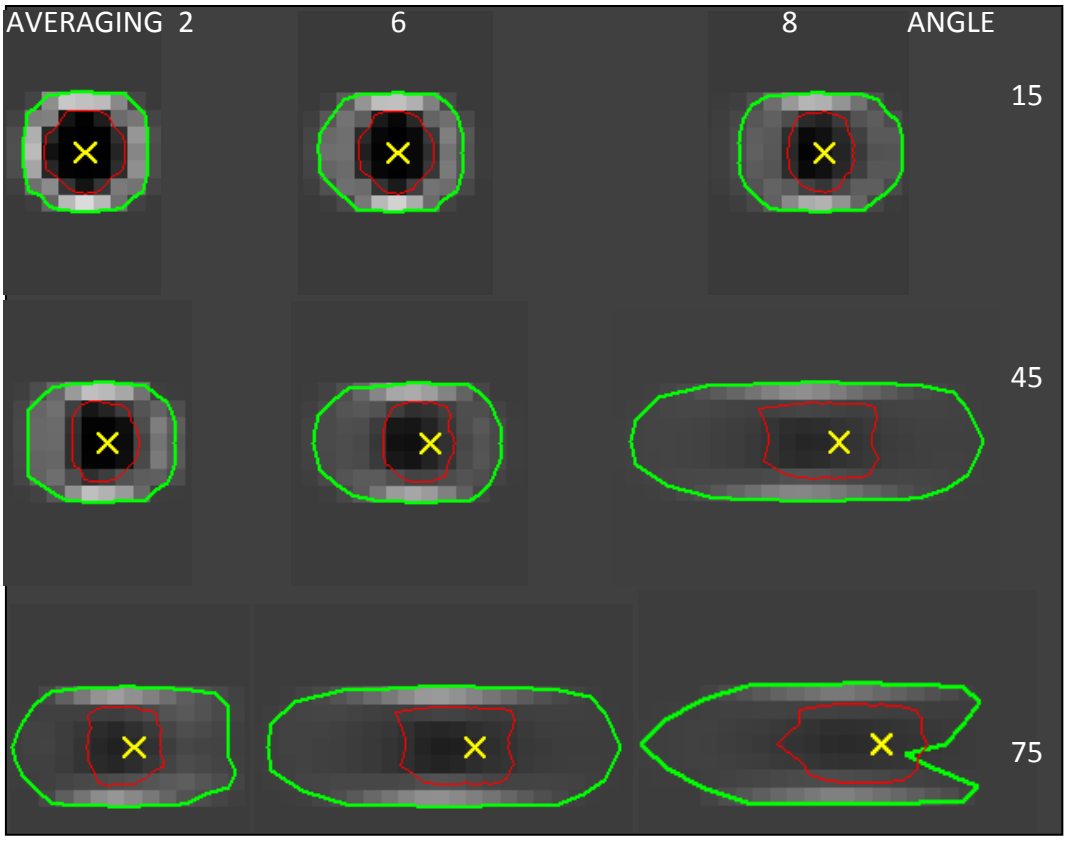

Figure 5.15: Screenshots of volume averaging effect after re-rotation back to orthogonal

Three airways: 2a (top) , 7f (middle) and 7h (bottom) rotated at 15, 45 and 75 degrees, then averaged with 2, 4 or 8 images and finally re-rotated back to orthogonal. Algorithm measurements are superimposed on the airways as follows: centroids shown in yellow, lumen-wall boundary in red, wall-parenchyma boundary in green.

Stair-step artifacts were also observed in some of the airways that were more pronounced at high angles. For instance, in Figure 5.15 a stair-step is visible in airway 7h at 75 degrees. The size and the number of the steps appeared to be related to the number of images used for averaging.

In some cases the algorithm measurements were not able to discriminate between the wall and the parenchyma boundaries. There was an increased measurement over-estimation of the wall-parenchyma boundary and to a lesser degree, measurement under-estimation of the lumen-wall boundary. These effects were more noticeable in smaller airways.

These observations were confirmed when the algorithm measurements were examined (Figure 5.16). LA bias became more negative with increasing angle and volume averaging (Figure 5.16A) and OWA bias became more positive with increasing angle and volume averaging (Figure 5.16C). LA and OWA uncertainty also increased with increasing angle and volume averaging especially for volume averaging greater than 4 and angles greater than 45 degrees (Figure 5.16B and Figure 5.16D). However,

the bias and uncertainty of the orthogonal measurements was much smaller than those found in comparable measurements made directly on rotated airways.

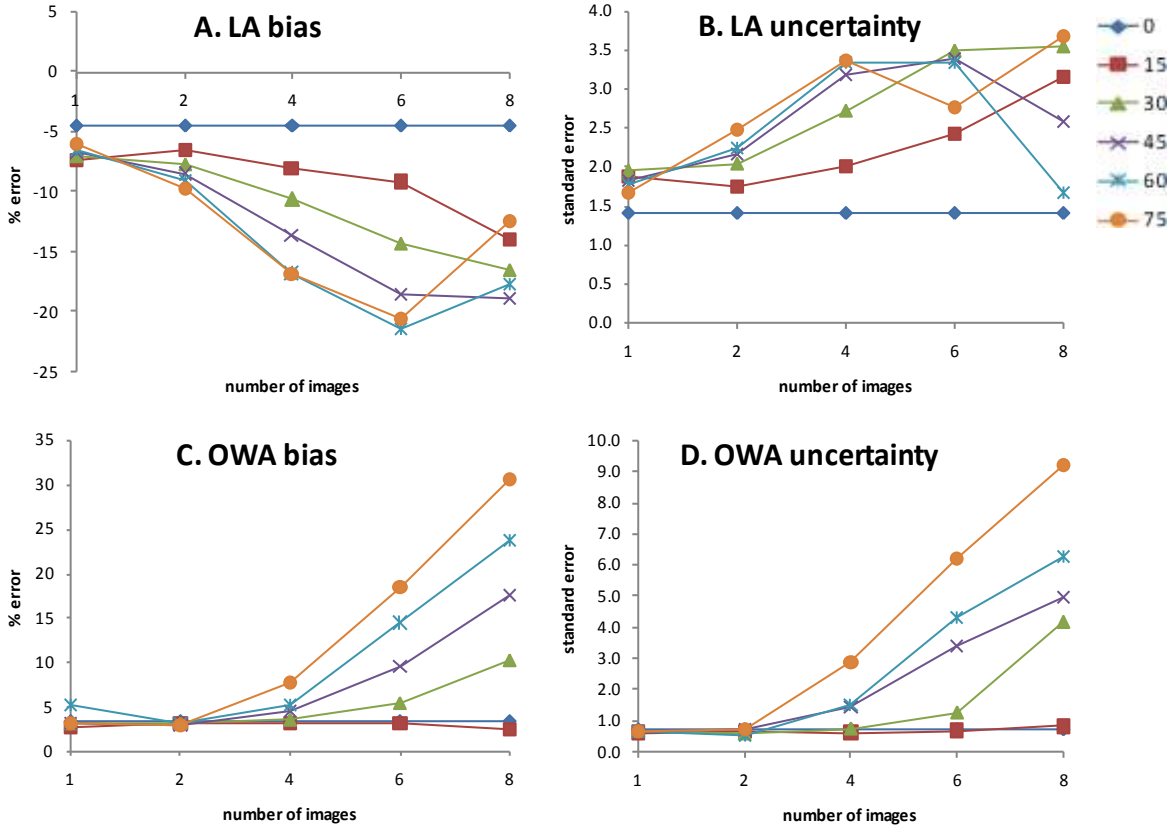

Figure 5.16: Volume averaging in re-rotated airway before correction

LA and OWA bias and uncertainty at 0, 15, 30, 45, 60 and 75 degrees in the 3.0mm² LA and 6.6mm² OWA grouped data.

Correction in airways rotated back to orthogonal

Since the airways had already been rotated back to orthogonal before measurement, no angle theory correction could be applied. Therefore the volume averaging correction only was applied to the measurements (Figure 5.17).

After correction, at high angles there was a tendency to underestimate the OWA and overestimate the LA. With LA bias, at angles of 60 degrees or more, under-estimation became over-estimation with increasing volume averaging (Figure 5.17A). With OWA bias the opposite relationship was found; at angles of 60 degrees or more, over-estimation became under-estimation with increasing volume averaging (Figure 5.17B).

Overall, the volume-averaging correction on the straightened airways reduced LA and OWA bias in all but the 75 degree groups. LA uncertainty was largely unaffected by the correction (Figure 5.17C) whereas OWA uncertainty was slightly reduced (Figure 5.17D).

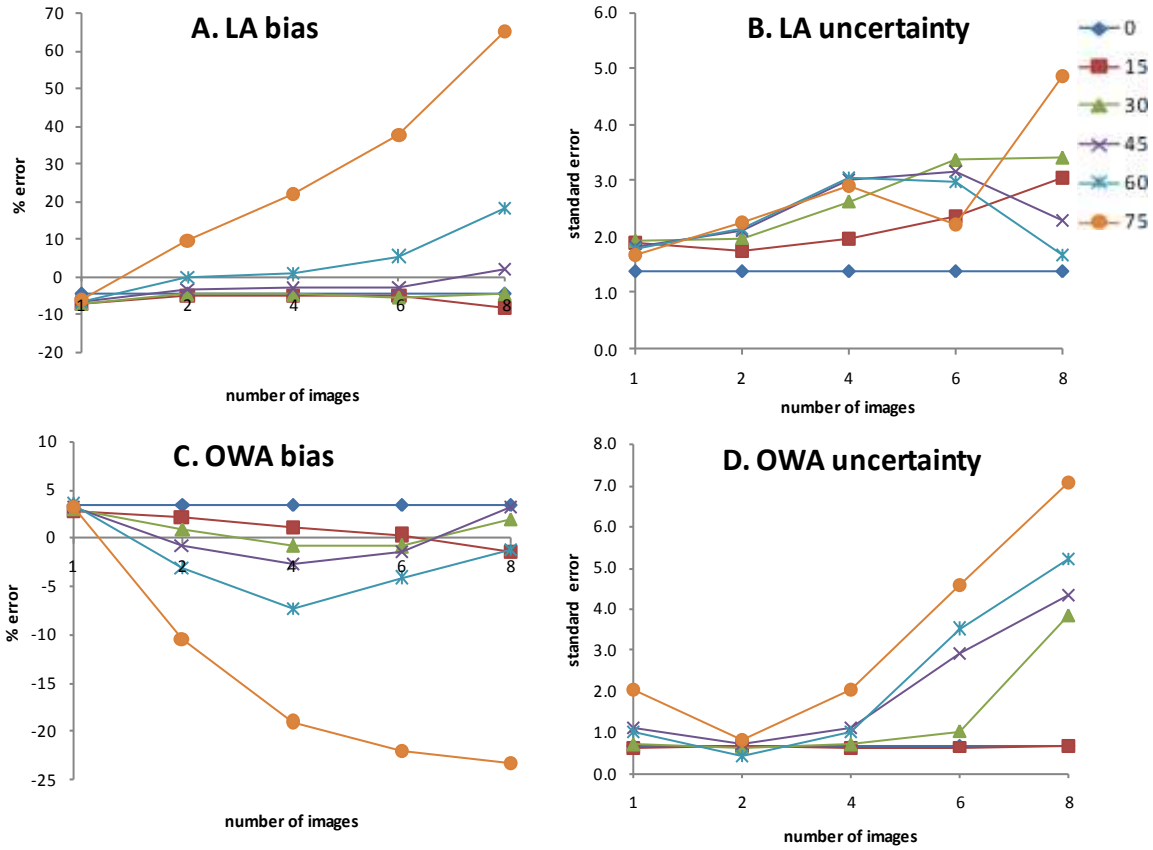

Figure 5.17: Volume averaging in re-rotated airways after correction

LA and OWA bias and uncertainty at 0, 15, 30, 45, 60 and 75 degrees in the 3.0mm² LA and 6.6mm² OWA grouped data.

Comparison between orthogonal and angled measurement

To determine whether rotating airways back to orthogonal would result in any significant improvement in CL algorithm performance compared with measuring the airways at an angle, an unpaired T-test was performed using the two groups of measurements. Correction was performed as follows:

- airways measured at an angle corrected by combined angle and volume averaging
- airway measured after re-rotation back to orthogonal corrected by volume averaging equation

In Table 5.1 these two approaches to airway measurement are compared. For this particular airway group with this amount of volume averaging, it was found that at low angles there was no significant difference between the two approaches. However at angles of 60 degrees or more for LA and 30 degrees or more for OWA, the orthogonal method performs with significantly less bias and uncertainty.

Furthermore, with increasing volume averaging, the difference between the two measurement techniques was exacerbated. For example at volume averaging of four images at 45 degrees or more for LA, and 15 degrees or more for OWA, the approaches were found to be significantly different (data not shown). This contrasted with the effect of airway size: with increasing airway size, the angle at which a significant difference between the two measurement techniques was found to grow larger. For instance, with the larger (5.8mm^2) LA group at volume averaging of two images a significant difference was found for 30 degrees or more.

TABLE 5.1: COMPARISON OF THE ROTATED VS STRAIGHTENED MEASUREMENT

Area	Rotated			Re-rotated		T-test
	Angle	*Bias*	*SD*	*Bias*	*SD*	*Probability*
LA	0	-4.46	4.86	-4.46	4.86	0.9999
	15	-5.67	5.75	-5.09	6.03	0.8131
	30	-6.40	6.42	-4.59	6.93	0.5127
	45	-8.14	8.33	-3.40	7.27	0.1520
	60	-12.23	12.27	0.00	7.39	0.0084
	75	-26.16	23.81	9.71	7.83	0.0002
OWA	0	3.46	1.53	3.46	1.53	0.9999
	15	3.52	1.71	2.16	1.50	0.2166
	30	3.73	2.00	1.01	1.35	0.0394
	45	4.53	2.14	-0.75	1.61	0.0027
	60	6.31	3.07	-3.11	1.00	0.0014
	75	9.97	5.22	-10.51	1.80	0.0004

Bias, standard deviation and statistical probability between the two measurement techniques with volume averaging of two images at different angles in the 3.0mm^2 LA and 6.6mm^2 OWA grouped data after correction.

5.5 Discussion

5.5.1 Rotation

As indicated in the theory and previously published work (King, Muller et al. 1999; Saba, Hoffman et al. 2003), LA, OWA and WA measurement bias was increased by rotation. This angle-dependent bias and uncertainty was largely removed using the angle theory correction equation.

With small airways, a size-dependent bias was introduced in LA and OWA. Interestingly, the LA and OWA size-dependent biases counter each other when calculating WA, resulting in a size-independent bias being present in WA measurements.

5.5.2 Volume averaging

As indicated in the theory, when volume averaging was introduced into rotated airways the airway lumen bias was reduced whereas wall areas bias was increased. Furthermore, the lumen-wall and wall-parenchyma boundaries became blurred and uncertainty was increased. The bias introduced by increasing the volume averaging and angle could be largely removed using a combination of both the correction equations. This was because the 'blurring' could be largely countered using the volume averaging correction equation, so that a combination of both correction equations largely eliminated the bias and reduced the uncertainty. However, some bias still remained and since the LA tended to be over-estimated and the OWA under-estimated by similar amounts for any given angle or volume averaging, the WA was under-estimated by approximately twice as much as the OWA. Both volume averaging and angle increased the uncertainty of the measurement but much of that was reduced post-correction.

At high levels of volume averaging, a stair-step (or saw-tooth effect) was observed on airway walls that were orientated at high angles. This aliasing artifact could have been reduced by smoothing and anti-aliasing techniques such as adaptive interpolation (Wang and Vannier 1994) or by Bayesian classification (Chiverton and Wells 2004). Although other correction equations have been developed to correct for the non-linear volume effect found in HRCTs of the human skull (Hsieh 1999) this is the first volume averaging correction that has been developed for airway measurement.

In this chapter no attempt was made to use the centroid's position to re-rotate the airways back to orthogonal. Instead, the re-rotation angle was simply the inverse of the original rotation angle. However, in HRCT airways this angle must be calculated using the relative position of the airway centroid in contiguous images. The angle's precision and accuracy and therefore the correction will be dependent on the accuracy and precision of the centroid calculation.

5.5.3 Airways re-rotated to orthogonal

In the majority of the studies to date measurements of airway lumen and wall area have been restricted to airways that appear to have been cut in cross-section (King, Muller et al. 2000). This was to minimise the effect of volume averaging in rotated airways.

Interestingly, the bias and uncertainty of the orthogonal measurements before correction was much smaller than those found in comparable measurements made directly on rotated airways. This implies that straightening the airways before

measurement will be more reliable than measuring them as they are presented in the HRCT data. After correction, the difference between the two approaches was found to be much smaller, and in the cases of larger airways at smaller angles insignificant. Therefore, the decision as to which approach to use depends on the size of the airway relative to the scanner z-axis resolution and the presenting angle of the airways to be measured.

LA and OWA measurement bias after straightening is not significantly different from measurement bias of rotated and averaged airways. It is, however, less uncertain. This may be because less correction needs to be applied, but it is more likely that it is because the algorithm performs with greater reliability with circular rather than elliptical structures. At high angles both approaches have low measurement accuracy and precision because data loss occurs due to averaging.

The equations presented in this chapter have been effectively used to reduce errors produced when measuring airways data, but errors still remain. These result from:

(a) the CL algorithm, which casts rays and then estimates the LA and OWA area based on a straight line between the rays. As discussed in the previous chapter the error obtained can be reduced by increasing the number of rays. It is possible that rotation and volume averaging may affect the number of rays required to obtain a small error.
(b) Pixel size-dependent sampling error. It was observed that measurement error reduced with increased structure size. There is a threshold at which airway measurement uncertainty is too large to allow the calculation of a size. This chapter has established that the airway wall area measurements have less uncertainty than the airway lumen measurements, and this may be a due to the smaller size of the airway lumens.
(c) Errors during rotation from tri-linear interpolation and rounding

The correction equations deduced in this chapter have been successfully used to calibrate the results from simulated data. However, the measurements obtained to this point do not take into account the fact that it may not be possible to measure the angle with high accuracy and precision. This is something which will be investigated in the next chapter when the correction equations will be applied to HRCT data to establish their viability in this technology.

CHAPTER 6

Validation using phantoms

Chapter 5 concluded that in simulated data, airway orientation had a bigger impact on measurement accuracy than volume averaging. Equipped with this finding, this chapter makes novel use of both artificial and tissue phantoms to test the CL algorithm's performance in data obtained directly from HRCT. It extends the work of previous chapters by establishing the effect of airway angle and volume averaging on airway measurement, but on this occasion, in HRCT images of phantoms. The purpose is to validate the CL algorithm in HRCT data, identifying the underlying differences between the simulated model from the previous chapter and HRCT phantom results.

CT scanner performance is often tested using artificial phantoms. Artificial phantoms are made from materials that have approximately the same density and dimensions of the structure they are simulating. Less common is the use of tissue phantoms, where a whole piece of the tissue of interest is explanted and scanned. The advantages of using tissue over artificial phantoms for CT validation arise from the fact that they more closely approximate the range of tissue densities and dimensions, as well as the complex structure of *in vivo* tissue. However, existing measurement techniques, such as planimetry, have been found to be inadequate for obtaining accurate 3-D measurements of tissue phantoms, limiting their usefulness (Dame Carroll, Chandra et al. 2006).

The newly emerged technique of micro-CT provides an ideal way of validating HRCT measurement accuracy in tissue phantoms since it effectively has the same X-ray absorptive basis as HRCT, but provides a fully 3-D isotropic data set and has two to three orders of magnitude higher spatial resolution, allowing volume averaging effects to be discounted. Thus micro-CT may provide the foundation for more effective use of a tissue phantom with airways of known dimensions.

6.1 Methods

Volumetric datasets from HRCT data were obtained using two novel phantoms:

(a) plastic tubing embedded in high density sponge; and
(b) explanted lung preparations from porcine lungs that were inflation-fixed in formalin.

True airway dimensions were obtained from:

(a) light microscopy for the artificial phantom; and
(b) micro-CT for the animal lung phantom.

Bias and uncertainty were examined for the same systematic trends as observed with the simulated model data in Chapter 5, and whether those trends could be corrected for using angle theory and volume-averaging equations.

By examining the accuracy and precision of the algorithm at various angles and airway sizes, the optimal method of measuring angled airways was determined from either:

(a) measurements made directly from the HRCT data with subsequent angle theory and volume-averaging correction to calibrate the 'measured area'; or
(b) reorientation of the airways to make them orthogonal to the scanning plane before measurement, with subsequent volume-averaging correction.

Plastic phantom construction

A lung airway phantom was constructed by embedding 10 plastic tubes in a high density Styrofoam (Clark Rubber, Bayswater, Vic, Australia). The plastic tubes were selected for similar size and density to airway wall (Table 4.1). The Styrofoam was also selected based on its similar density to lung parenchyma (Kitaoka and Kitaoka 2002).

Lung preparation and fixation

Excised porcine lungs were obtained from a local butcher and examined for intact lobes. Two lobes were removed and the main bronchus cannulated in both cases. A syringe was used to inflate each lobe to physiological pressure with air, examining the lobe for leaks. Both inflated lobes were immersed in a bath of formalin for four weeks to ensure complete fixation. After fixation, the lung lobes were scanned by HRCT as indicated below and airways of interest were identified. The lung was then cut into 2-cm cubes in a plane approximately perpendicular to the z-axis of the airways of interest. The cut surfaces of the lung cubes were photographed. Finally, the 2-cm lung cubes were wrapped in plastic wrap for protection (Paraplast; Tyco Healthcare, Mansfield, MA, USA).

HRCT phantom scanning

All phantoms were scanned in the HRCT scanner (GE 4-slice Lightspeed, GE Medical Systems, Minneapolis) at 0, 20, 40, 60, 90 degree angles to the scanning plane. Standard clinical HRCT settings were used; 100kV and 100mAs at a slice thickness of 0.625mm in helical mode. Images were reconstructed using the GE high spatial frequency 'Lung' and 'Bone' algorithm at two different field of views (FOV) of 36 cm, which yielded a voxel size of 0.703 x 0.703 x 0.625 mm. Images were recorded in 12-bit dicom format and recorded to CD for later analysis.

Plastic phantom measurement by light microscope

Orthogonal sections of the tubes were affixed to a slide and the horizontal lumen diameters (*LDx*) and vertical lumen diameters (*LDy*) were measured using a optical micrometer and light microscope (LM). The mean Wall Thickness (*WT*) was obtained by measuring the wall cross-sectional distance twice and taking the mean. These measurements allowed lumen area (LA) and outer wall area (OWA) to be calculated as follows:

If the tube is considered to have radius, *r*, area of the tube $= \pi r^2$. However since the tubing was not circular, but instead elliptical:

$$Area = \pi \,.\, rx \,.\, ry \qquad \textbf{(6.1)}$$

where rx and ry is radius in the two planes.

For the lumen area calculations:

$$rx = \frac{LDx}{2} \qquad \text{and} \qquad ry = \frac{LDy}{2} \qquad \textbf{(6.2)}$$

Similarly, outer wall area calculations:

$$rx = \frac{LDx+2.WT}{2} \qquad \text{and} \qquad ry = \frac{LDy+2.WT}{2} \qquad \textbf{(6.3)}$$

As indicated previously, WA was calculated by subtracting LA from OWA.

Micro-CT scanning

The pig lung cubes were scanned with a micro-CT SkyScan 1072 desktop system (SKYSCAN, Aartselaar, Belgium). Micro-CT settings were 100kV and 100mAs at a slice thickness of 0.019mm and a FOV of 19mm, which yielded a voxel size of 0.019 x 0.019 x 0.019 mm. Each cube was scanned every 0.23 degrees as it rotated around its vertical axis until it had rotated 180 degrees, at an exposure time of 0.9 seconds per scan. Images were reconstructed using *ConeRec* software (provided by SkyScan).

Reconstructed image data were recorded in 8-bit bitmap format onto DVD for later analyses.

Registration

For the pig lung phantom, stereotactic matching was performed to accurately align the HRCT and micro-CT data sets to a common frame of spatial reference. Airways were matched between the HRCT and micro-CT images using two synchronised copies of *winImageBase* and airway branch points as fiducial anatomical markers (Figure 6.1).

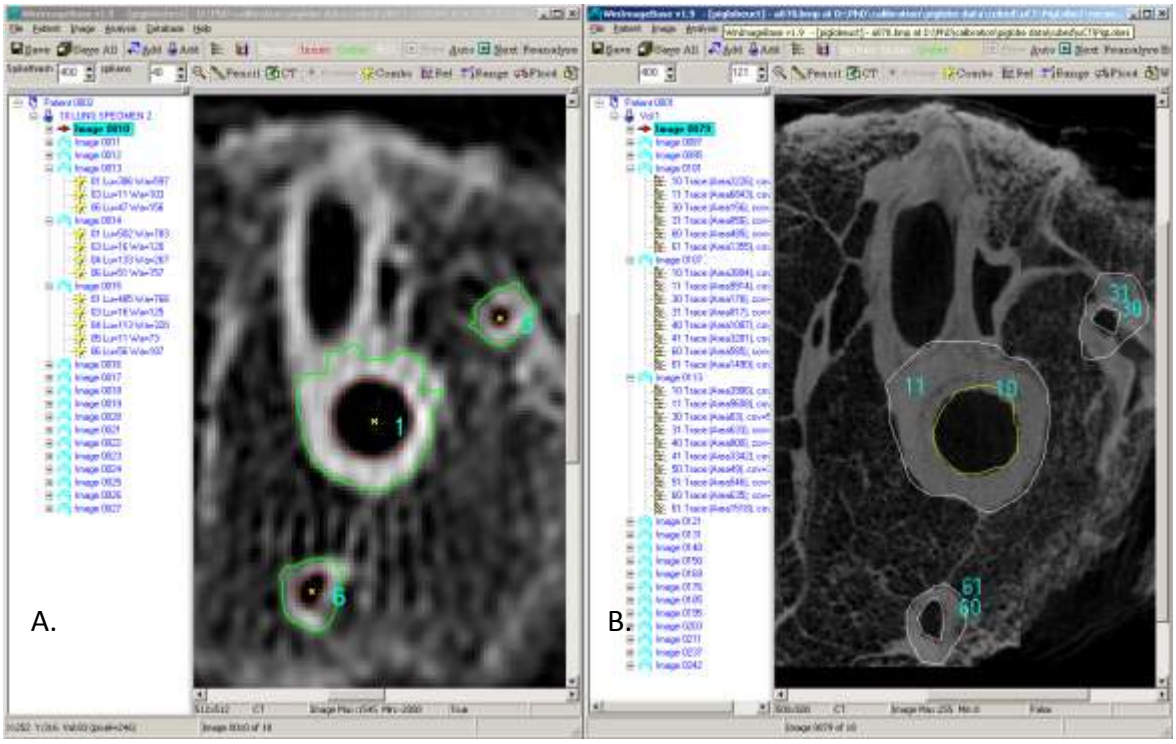

Figure 6.1: Screenshot of two synchronised copies of winImageBase

Airways matched between (A) HRCT and (B) micro-CT datasets. The HRCT airways were measured using the CL algorithm and the micro-CT airways traced using the wand tool. Zoom, panning and traversing between the two datasets was handled by communication between the two programs automatically. Superimposed CL algorithm measurements of lumen-wall boundary (red) and wall-parenchyma boundary (green), and (right) manual tracings of lumen-wall boundary (red) and wall-parenchyma boundary (green).

If approximate manual alignment of the datasets was found to be insufficient, the *winImageBase* software was used to calculate the mean difference in *x-y*, *x-z*, and *y-z* angles between stereotactically matched airways. This allowed the *win3D* software to rotate the micro-CT dataset for 3-D registration (Figure 5.7).

3-D rotation and registration

To perform 3-D rotation of the HRCT phantom data, a preliminary step was required. The dicom images previously recorded onto CD were converted from 12-bit to 8-bit

bitmaps using contrast shrinking with *VgStudioMax* (Volume Graphics GmbH Heidelberg, Germany). The bitmap data was imported into *win3D* and 3-D rotation of the micro-CT dataset was performed using the *x-y*, *x-z*, and *y-z* angles so that it aligned with the corresponding HRCT dataset.

Airway measurement by CL algorithm

For both the pig lung and plastic phantom, HRCT data was imported into the *winImageBase* software, where airway lumen and wall area measurements were made using the CL algorithm with standard settings of 40 interpolated rays and half-max edge detection. For each of the 10 plastic tubes, 11 random images were selected and one CL measurement was made from each. Thus, a total of 110 measurements were made at each scanning angle 0, 20, 40, 60 degrees.

Image analysis

Micro-CT datasets were imported into *winImageBase* where airway lumen and wall areas were measured by manually tracing the lumen-wall and parenchyma-wall boundaries (Figure 6.1). Two copies of *winImageBase* were run simultaneously on a dual-screen workstation allowing visual matching of corresponding airways in both the HRCT and micro-CT datasets. All airways that were visible in each of the HRCT images were measured, allowing the creation of a contiguous branching airway tree. The centroid of each airway in adjacent images was used to calculate the angle changes within the airway (Figure 6.2).

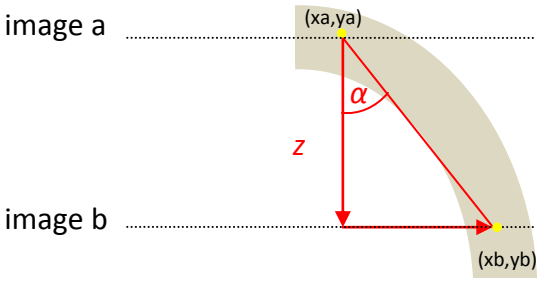

Figure 6.2: Schematic of airway angle measurement between two adjacent HRCT images.

(xa, ya) represents the centroid of the airway in image a and (xb, ya) the centroid of the same airway in image b, with z being the distance between adjacent images.

The *x-z* and *y-z* angle calculations used in the correction were obtained from the perimeter mass centroid from the micro-CT data as follows:

$$\alpha x = \tan\frac{\mathrm{xa} - \mathrm{xb}}{z} \quad \text{and} \quad \alpha y = \tan\frac{\mathrm{ya} - \mathrm{yb}}{z} \qquad \textbf{(6.4)}$$

The angle information was used to correct the LA, OWA and WA as previously demonstrated in Chapter 5.

Statistical analysis

Mean and standard deviation of the measurement error were calculated. Percentage error was calculated using the following equation:

$$\%\ error = \frac{true\ area - measured\ area}{true\ area}\ x\ 100 \qquad \textbf{(6.5)}$$

The degree to which these measurements agreed when the lumen and wall algorithms were applied in micro-CT and HRCT was calculated by the method of Bland & Altman (Bland and Altman 1986; Bland and Altman 1996; Bland and Altman 2003). Bias and uncertainty were calculated as in Chapter 5. All data are shown as mean ±95% confidence interval unless otherwise specified. The 95% limits of agreement were calculated as $t_{0.05}$ x standard deviation of the differences between micro-CT and HRCT measurements where $t_{0.05}$ is the critical t-value corresponding to the sample size at the 0.05 level of significance.

6.2 Results

6.2.1 Plastic phantom before correction

After importing the HRCT images into *winImageBase*, CL algorithm measurement of the 10 plastic tubes at all the scanning angles was possible, with the exception of 90 degrees.

When the plastic tubes were measured by LM, the LA ranged from 3.3mm^2 to 42.2mm^2 and the wall area from 4.0mm^2 to 45.7mm^2.

During examination of the tube images it was observed that scanning at different angles had caused the airways to appear elliptical with larger airway lumen and walls (Figure 6.3) as expected. The greater the scanning angle, the greater this effect appeared to be. Furthermore, with increased angle there was increased blurring of the airway walls both into the airway lumen and into the surrounding space.

The CL algorithm measurements followed the contours well in all cases, LA, WA and OWA visibly increased with increasing rotation.

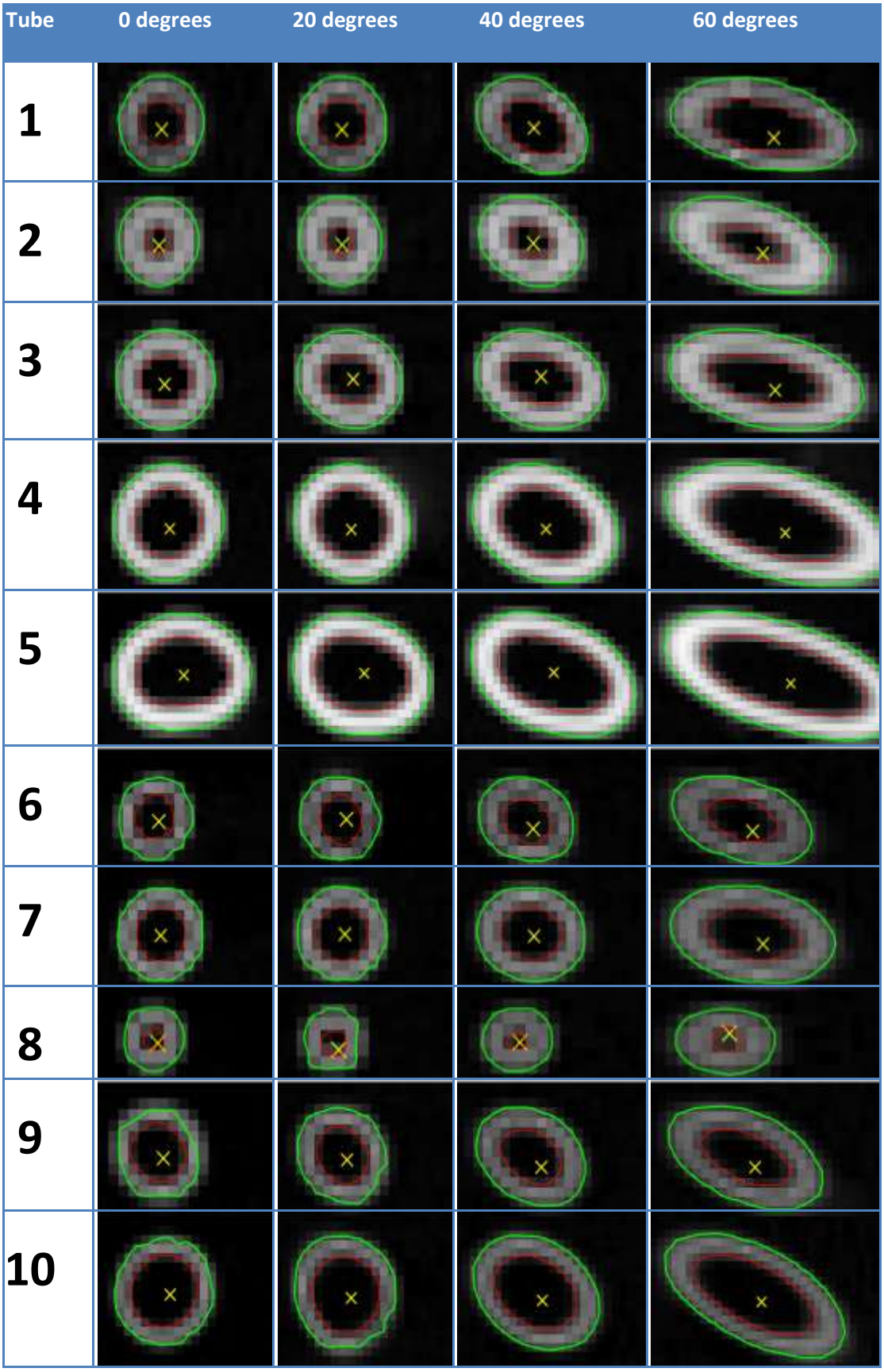

Figure 6.3: HRCT images of plastic phantom scanned at various angles

10 plastic tubes scanned at 0, 20, 40 and 60 degrees. CL algorithm measurements superimposed: lumen-tube boundary (red), wall-sponge boundary in green and centroid in yellow.

These observations were confirmed when examining the effect of scanning angle on the measurement of LA (Figure 6.4A), OWA (Figure 6.4C) and WA (Figure 6.4E). In all cases increasing angle caused increased measurement size, with size increases becoming progressively larger with larger angles. Furthermore, with increasing angle increasing measurement uncertainty was observed, particularly at 60 degrees.

When percentage errors were investigated, a similar angle-dependent error relationship was obtained for all tubes in LA (Figure 6.4B), OWA (Figure 6.4D) and WA (Figure 6.4F), where increasing angle caused increasing over-estimation.

The major difference between individual tubes appeared to be a size-dependent error at any one scanning angle, where smaller structures were progressively under-estimated. This relationship is further explored in Figure 6.5. With LA error (Figure 6.5A) and LA %error (Figure 6.5B) there was a strong linear size-dependency. For OWA, although there was also a linear size-dependent error (Figure 6.5C), when this was converted to percentage error, there was no size dependency present (Figure 6.5D). When these measurements were used to calculate WA, the error (Figure 6.5E) and %error (Figure 6.5F) largely followed that of OWA.

At 0 degrees, the smaller the airway structure being measured, the larger the LA under-estimation. Furthermore, although LA was under-estimated, WA and OWA were over-estimated. With increasing scanning angle, the bias became less negative to the point where under-estimation became over-estimation. Since the bias was largely independent of airway size, the bias depended on the amount of under-estimation at 0 degrees and the angle only.

Overall, the estimation of the OWA was less precise than for the LA. With increasing angle, over-estimation of OWA was obtained. However this over-estimation does not appear to be dependent on airway size.

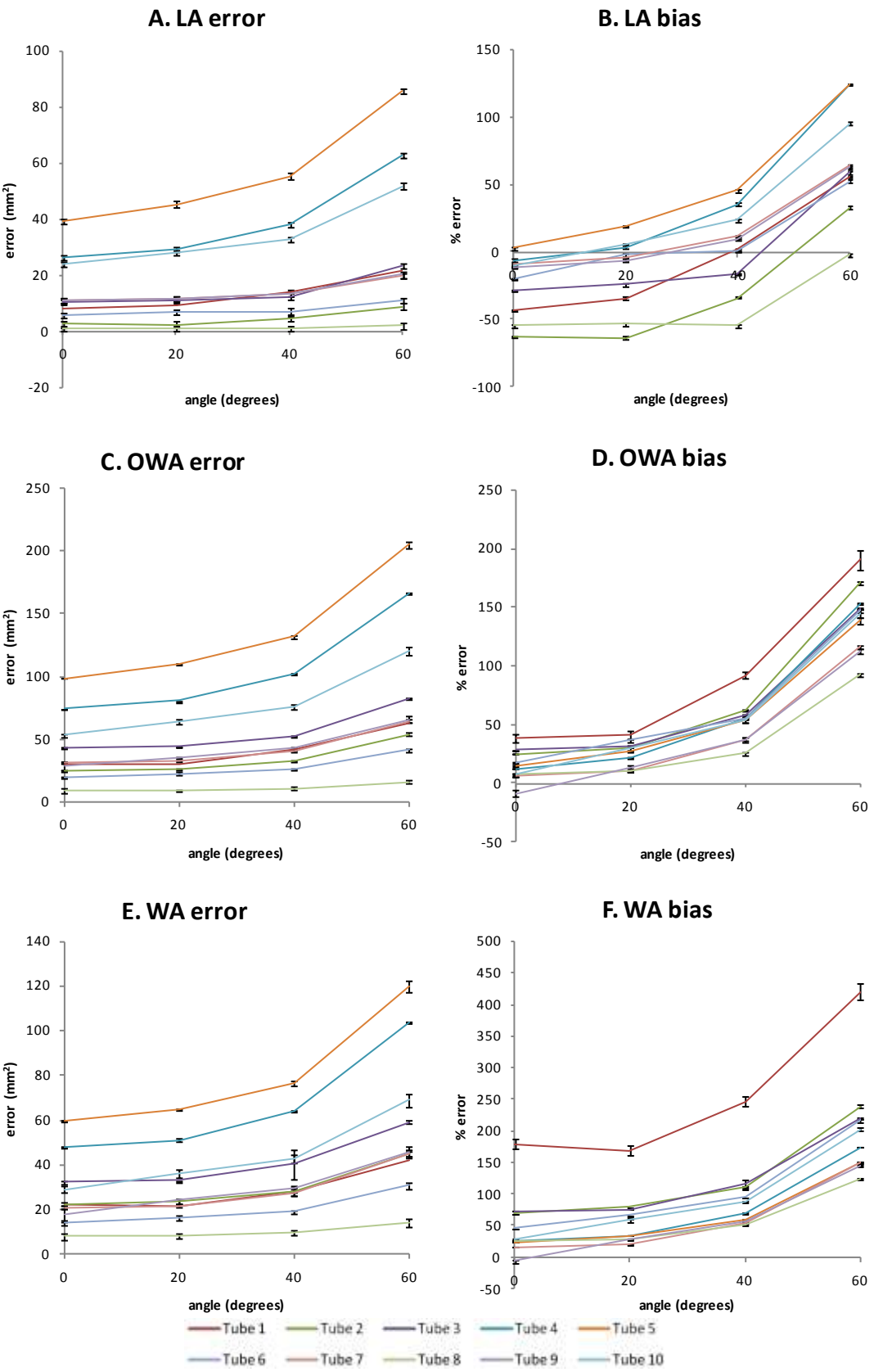

Figure 6.4: The effect of rotation on measurement area and bias

(A), (C), (E) error and (B), (D), (F) % error of measured LA, WA, OWA areas with increasing angle in 10 phantoms. Each point is the mean of 11 repeat measures, error bars represent ± standard deviation.

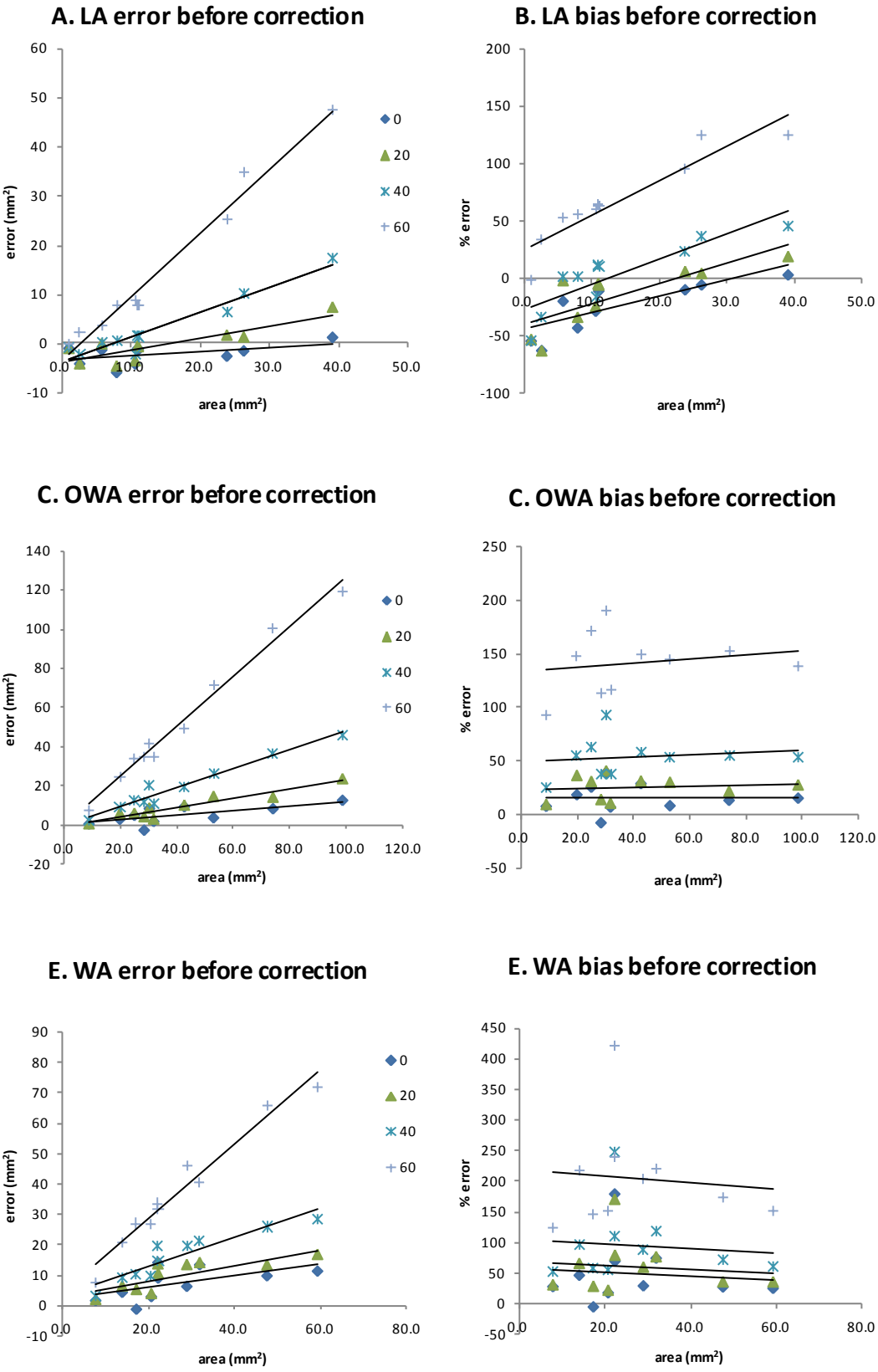

Figure 6.5: The effect of phantom size on error and bias before correction

mean LA (A), OWA (C) and WA (E) error and % error (B, D, F) with increasing structure size at 0, 20, 40, 60 angles. Each point is the mean from 11 repeat measures a single phantom.

6.2.2 Plastic phantom after correction

Using the combined angle theory and volume averaging equation presented in Chapter 4, the LA and OWA for each tube at 20, 40 and 60 degrees were calculated from the LM measurements at zero degrees (Table 6.1).

TABLE 6.1: CALCULATED PHANTOM AREAS AT 20, 40 AND 60 DEGREES

Tube	0			20			40			60		
	LA	WA	OWA	LA	WA	OWA	LA	WA	OWA	LA	WA	OWA
1	13.7	8.0	21.7	13.9	10.2	24.1	16.3	14.8	31.1	24.1	28.0	52.1
2	6.6	13.3	19.9	6.5	15.6	22.1	7.5	21.2	28.7	10.8	37.5	48.3
3	14.7	18.4	33.2	15.0	21.4	36.4	17.7	28.8	46.5	26.3	50.1	76.4
4	27.9	37.7	65.6	28.7	42.9	71.5	34.1	56.3	90.4	51.0	95.3	146.2
5	38.1	47.9	86.0	39.5	53.7	93.2	47.4	69.6	117.0	71.5	115.7	187.1
6	7.1	9.7	16.7	7.0	11.7	18.7	8.0	16.3	24.3	11.6	29.7	41.3
7	12.0	17.8	29.8	12.1	20.8	32.9	14.0	28.2	42.2	20.7	49.4	70.1
8	2.0	6.2	8.2	1.8	7.5	9.4	2.0	10.5	12.4	2.7	19.2	21.9
9	12.3	18.6	30.9	12.5	21.6	34.0	14.6	29.0	43.6	21.5	50.6	72.1
10	26.5	22.7	49.2	27.2	26.6	53.8	32.3	36.0	68.3	48.2	63.1	111.3

LA=lumen area, WA=wall area, OWA=outer wall area

Comparison of the corrected LM measurements with the mean CL algorithm measured areas is shown in Figure 6.6. Before correction, the expected scanning angle-dependent bias and uncertainty were observed in the mean measurements (Figure 6.6A and Figure 6.6B). After angle correction, these were removed (Figure 6.6C and Figure 6.6D). Following the combined angle and volume averaging correction, increasing angle resulted in decreased measurement bias (Figure 6.6E). However, no difference could be observed between the uncertainty after angle correction and the uncertainty after combined correction (Figure 6.6F). As expected, no effect was observed at zero degrees.

In summary, the effect of correction was to remove the scanning angle-dependent nature of the error and uncertainty. This resulted in reduced mean measurement error of -18.8% ± 7.1% for LA, 15.0% ± 4.0% for WA, and 41.2% ± 12.6% OWA at angles up to 60 degrees.

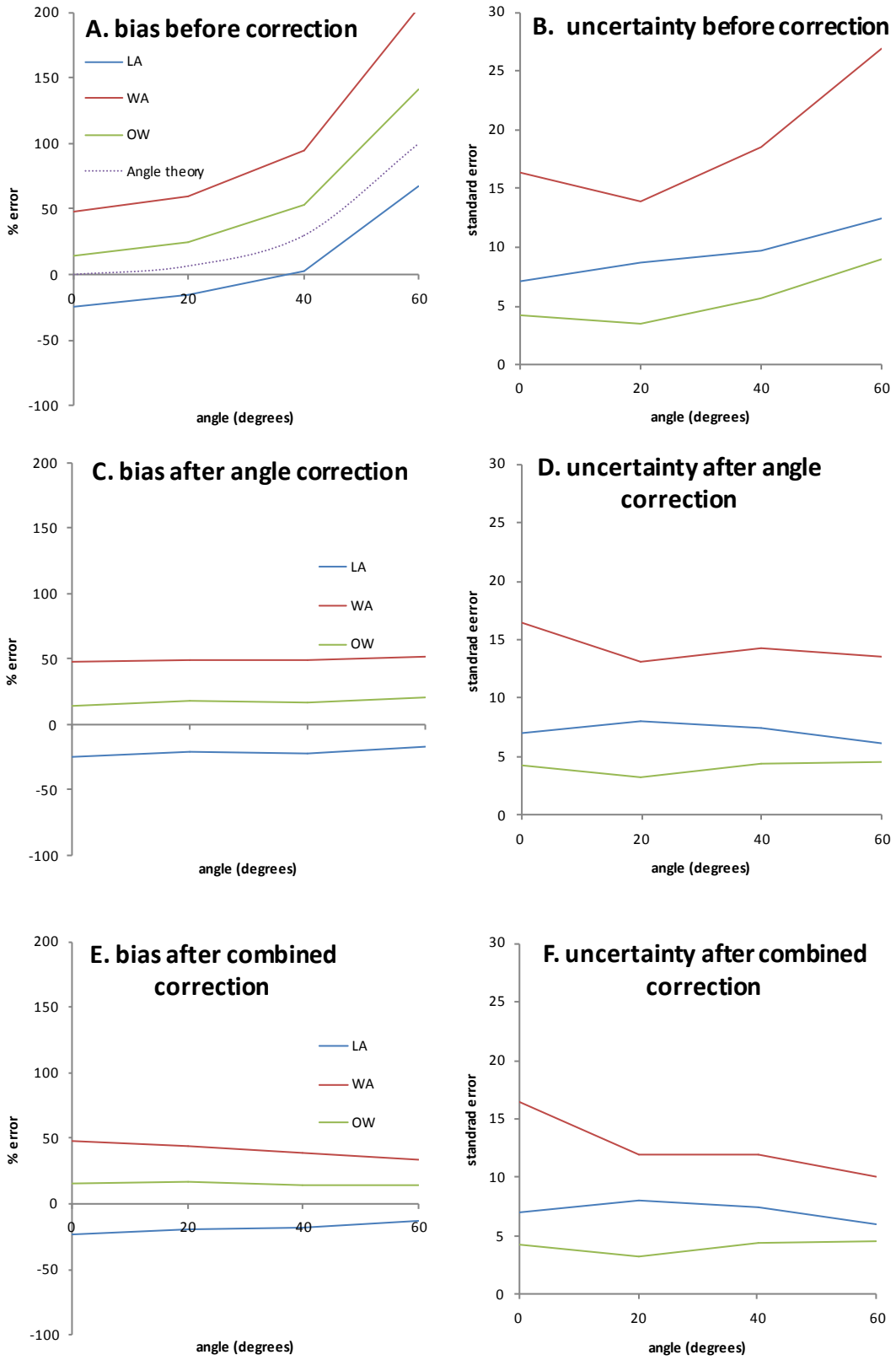

Figure 6.6: Correction in the plastic phantom at various angles

(A), (C), (E) mean bias and (B), (D), (F) uncertainty in measured LA, WA, OWA areas with increasing angle in 10 phantoms with 11 repeat measures: before (top), after angle correction (middle,) and after combined angle and volume averaging correction (bottom)

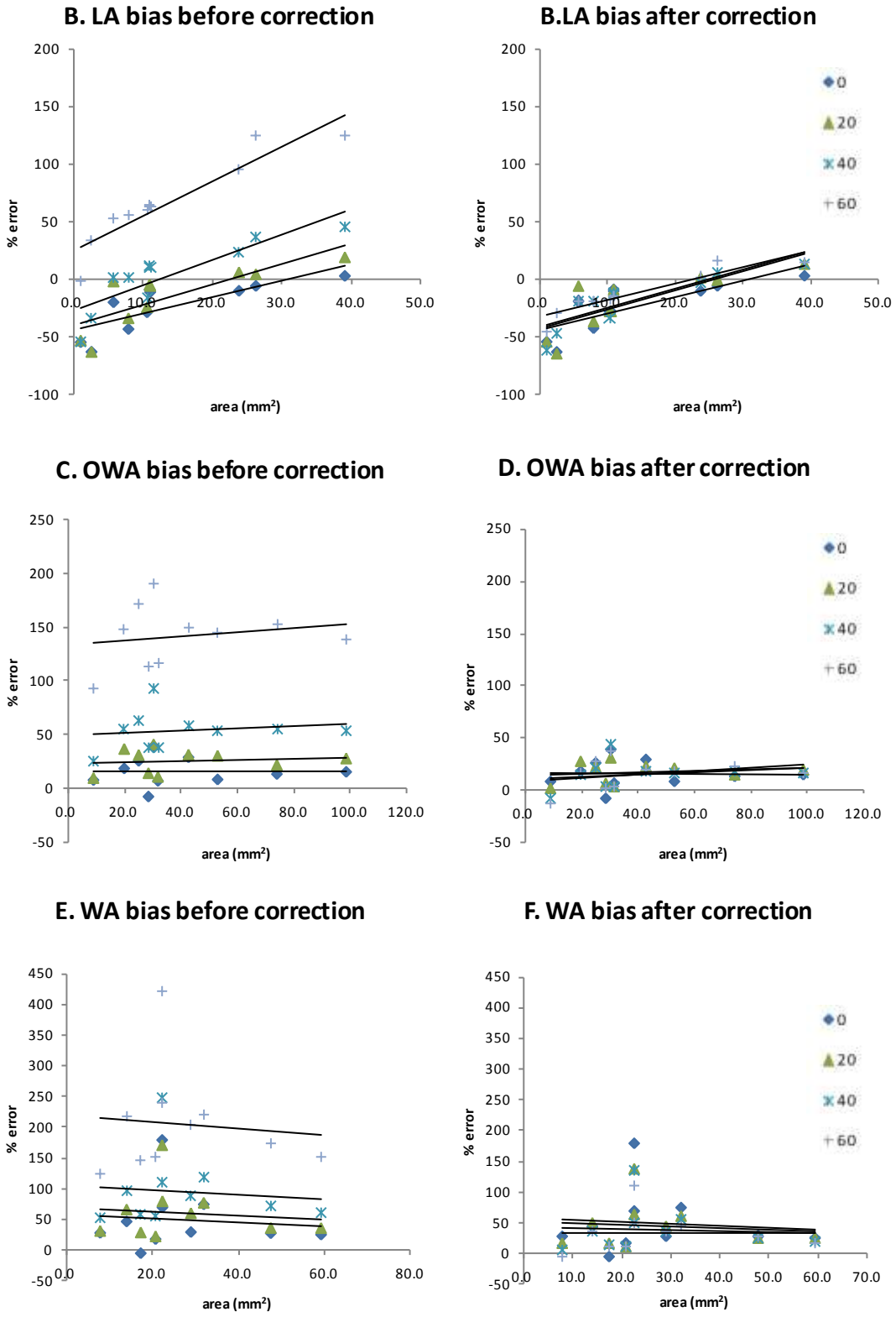

Figure 6.7: Effect of phantom size before and after combined correction

% error LA (A), OWA (C) and WA (E) before and after (B, D, F) with increasing structure size at 0, 20, 40, 60 angles. Each point is the mean from 11 repeat measures a single phantom.

.

In Figure 6.7 the size-dependent nature of the errors before and after correction was compared. With increasing angle there is a linear increase in both LA and OWA area error, although the size-dependency is reduced from previous . There appears to be no relationship between size and WA. The uncertainty of the LA error appeared to be size dependent, so that with small areas at high angles, we obtain increased uncertainty in the degree of estimation.

6.2.3 Measurement after rotation back to orthogonal

To determine whether rotating the phantom back to orthogonal significantly improves the CL algorithm performance compared with measuring the airways at an angle, the HRCT data must be rotated.

To do this, the data were first converted from 12-bit, since *win3D* required 8-bit images. The effect of converting the data to 8-bit was found to be non-significant in this data with excellent agreement between measurements obtained from 8-bit and 12-bit data (Figure 6.8).

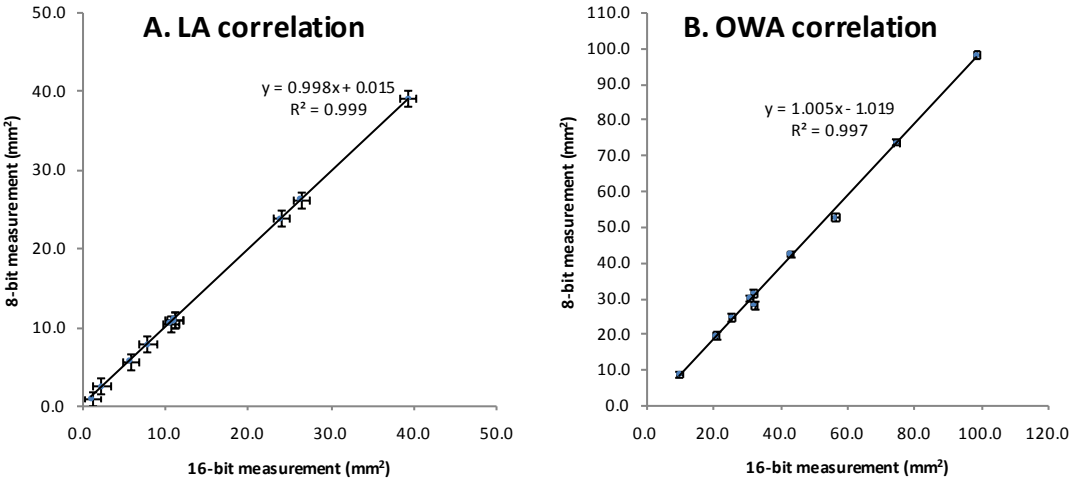

Figure 6.8: Effect of converting 12-bit dicom data into 8-bit bitmap data

Effect of converting the HRCT plastic phantoms at zero degrees with (A) LA, and (B) OWA. Each point is the mean of 11 measurements with error bars presenting standard error.

After rotation to orthogonal, inspection of HRCT images was carried out (Figure 6.9). No differences were observed between the control airways (scanned orthogonally) and those that had been rotated to orthogonal from their scanning plane.

When the effect of angle on mean LA and OWA bias was examined mean LA was under-estimated whereas OWA was over-estimated at all angles. With increasing angle, both biases increased slowly. Similar to OWA, WA was over-estimated, and over-estimation increased with increasing angle. When examining the uncertainty of

these measurements a similar pattern was observed both in the magnitude, direction and effect of angle in LA, WA and OWA.

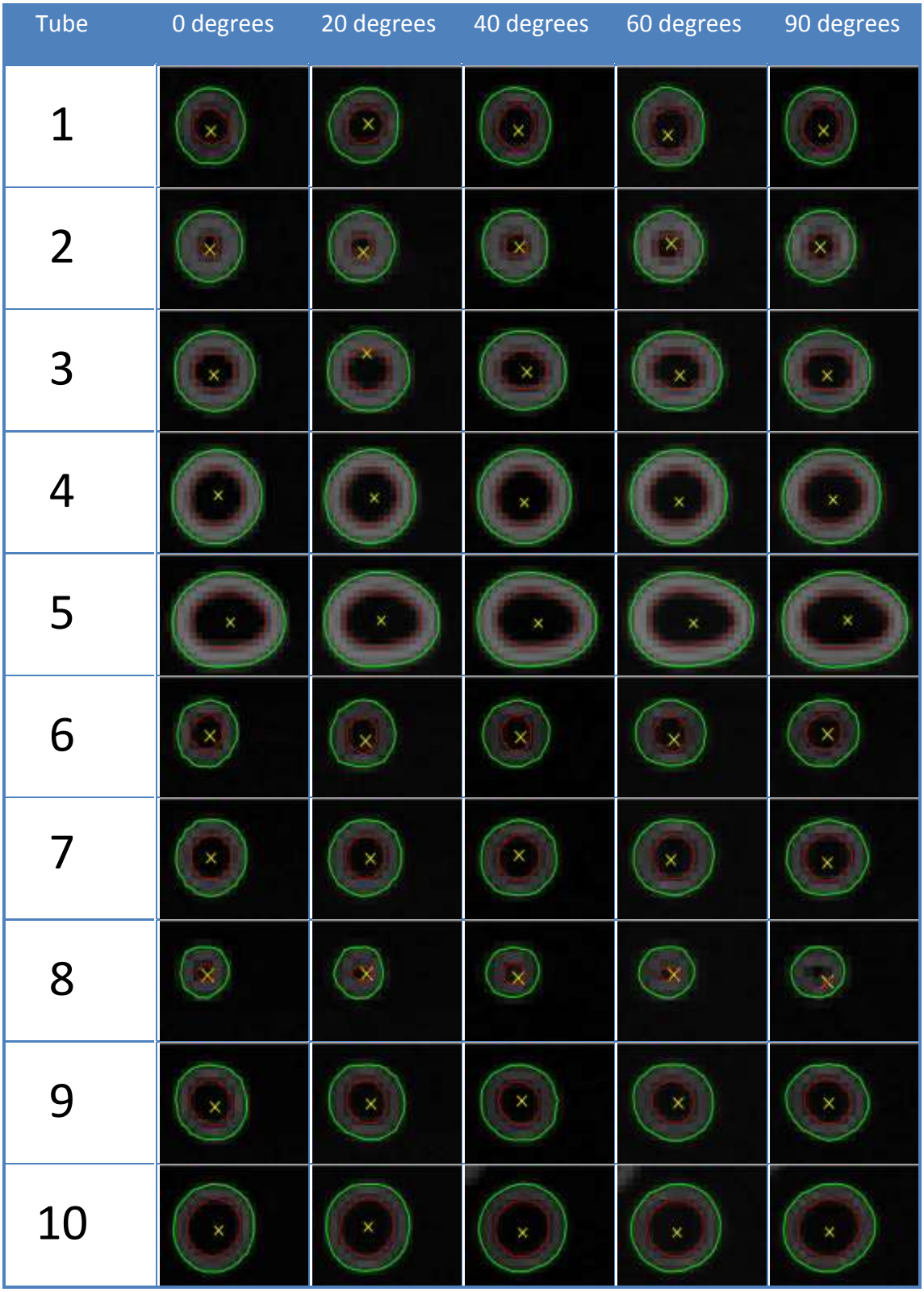

Figure 6.9: Re-rotation to orthogonal in HRCT images of plastic phantom

10 plastic tubes scanned at 0, 20, 40 and 60 degrees and then rotated back to orthogonal before measurement. CL algorithm measurements superimposed: lumen-tube boundary (red), wall-sponge boundary in green and centroid in yellow.

After the volume-averaging correction had been applied to the orthogonally rotated airway measurements, the effects of scanning angle on bias and uncertainty were examined. Since the volume-averaging correction was dependent on a scanning angle being present, the equation had no effect on the airways at zero degrees. However, angle-dependent bias increases in LA were prevented by the use of the volume-averaging equation and reduced bias and uncertainty with increasing angle was observed in OWA and WA. A similar pattern was observed with uncertainty; angle-dependent increases in LA and OWA were prevented, leading to a reduction in WA uncertainty with increasing angle.

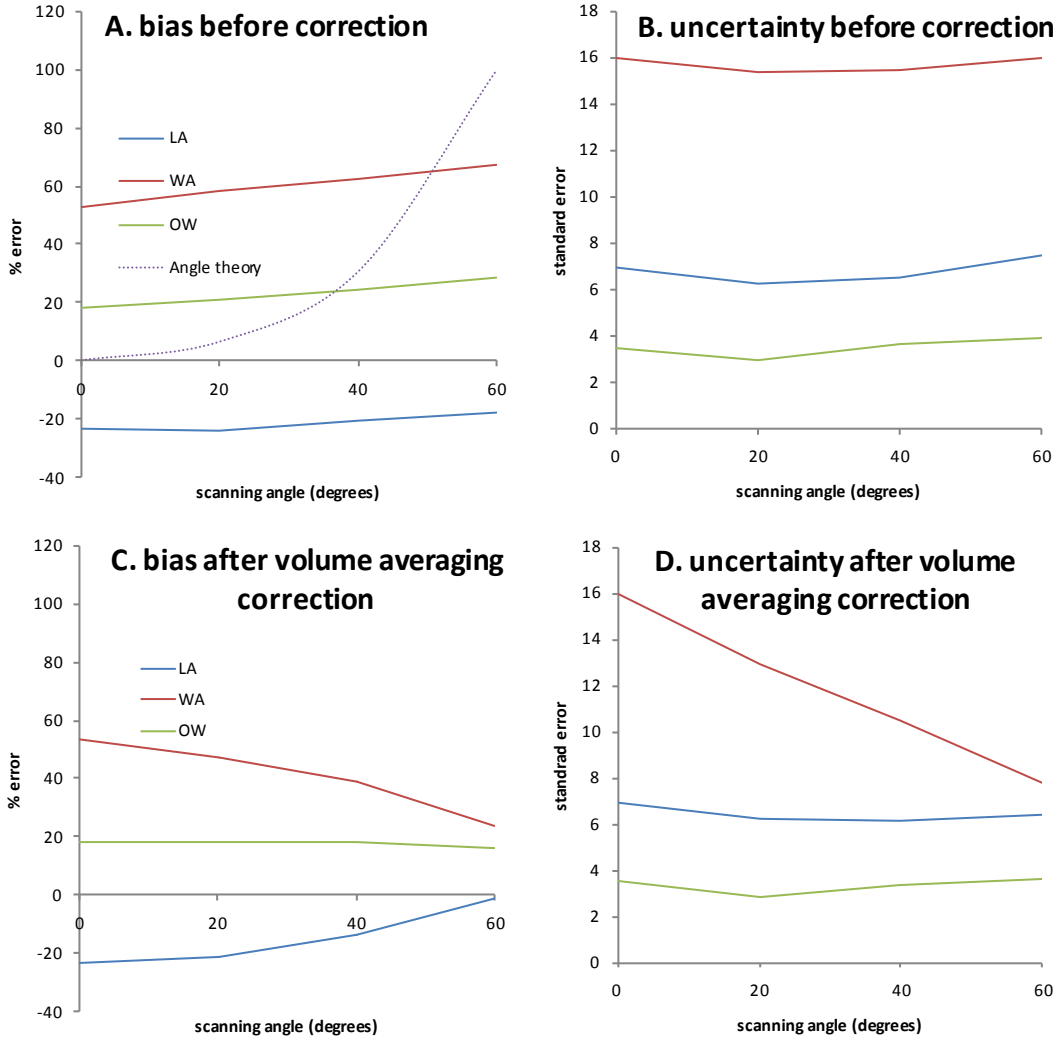

Figure 6.10: Effect of scanning angle on re-rotated phantom before and after correction

(A), (C) mean bias and (B), (D) uncertainty in measured LA, WA, OWA areas with increasing angle in 10 phantoms with 11 repeat measures: before (top), after volume averaging correction (bottom)

6.2.4 Pig lung phantom before correction

A total of 140 micro-CT and HRCT measurements from two pig lungs scanned on different occasions were compared. The two cubes had airways of different size ranges. The airways measured from cube 1 had larger airways than those measured from cube 2 (Table 6.2).

TABLE 6.2: INITIAL RESULTS FROM THE PIG LUNG CUBES

		LA	OWA	WA
CUBE 1	error mean (mm^2)	-0.5	1.7	2.2
	error 95% CI limits	2.8	4.2	4.6
	range max	18.9	50.3	36.9
	range min	0.4	1.7	1.0
CUBE 2	error Mean (mm^2)	-0.2	1.7	1.8
	error 95% CI limits	0.7	1.6	1.5
	range max	3.9	9.2	5.7
	range min	0.3	1.1	0.3

No size-dependency in errors in LA (Figure 6.11A), OWA (Figure 6.11C) or WA (Figure 6.11E) were revealed in either cube. However, errors were systematic in distribution so that for any sized airway LA was under-estimated, whereas OWA and WA were over-estimated. Furthermore, mean errors were similar for both cubes, but the 95% CI was lower for the second cube, demonstrating more precise area estimation in this cube.

Figure 6.11B, Figure 6.11D and Figure 6.11F show the relative errors in LA, OWA and WA. For both cubes a similar pattern in relative error distribution was observed. With increasing airway size, relative errors became smaller. In addition, with OWA and WA, decreasing airway size resulted in increasing over-estimation.

Further analysis was continued with the second cube.

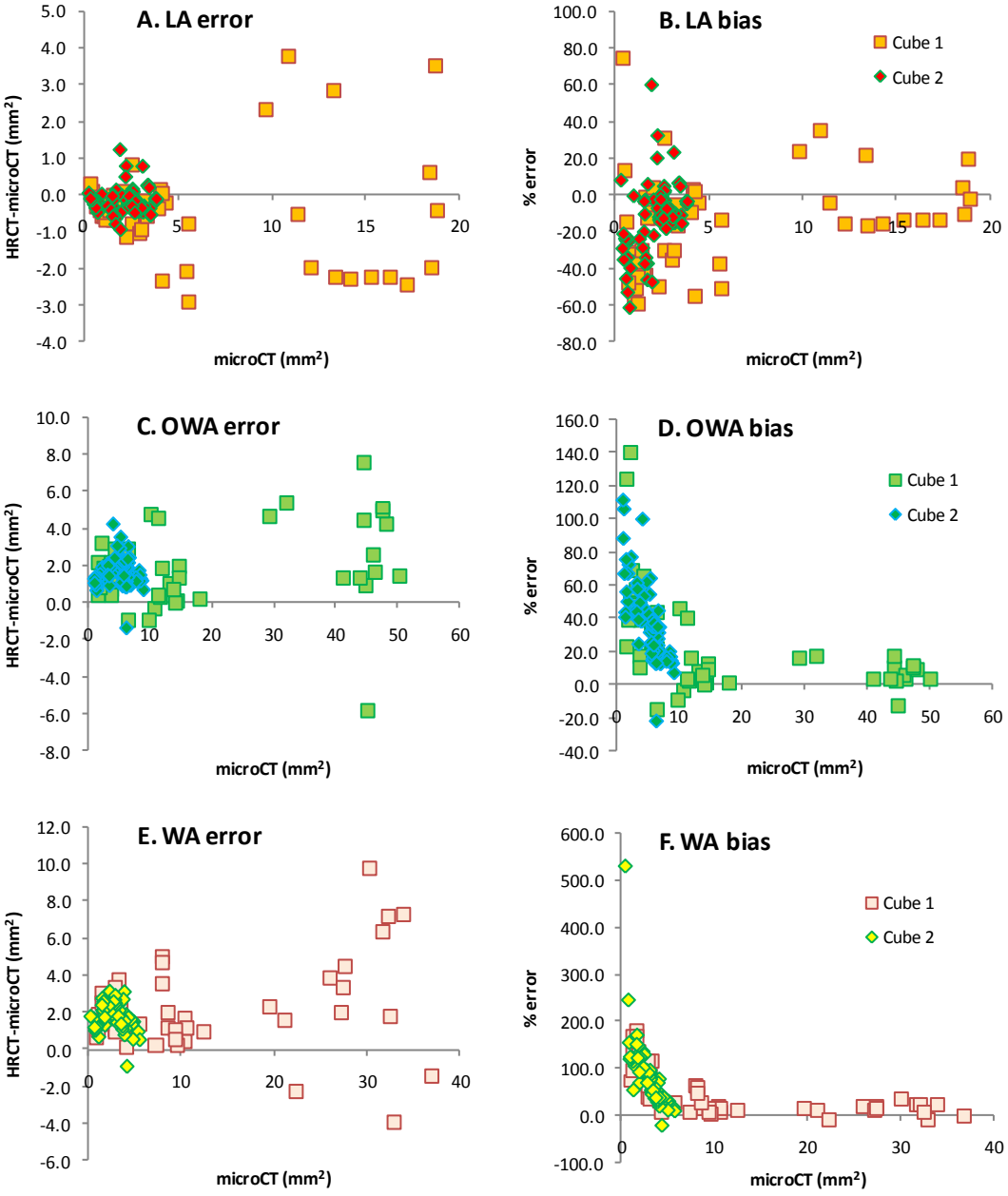

Figure 6.11: The effect of pig lung airway size on error and bias in 2 pig lung cubes

LA (top), OWA (middle) and WA (bottom) errors(A, C, E) and % errors (B, D, F) in various sized airways

.

6.2.5 Pig lung phantom after correction

Application of the angle theory correction and volume averaging equations to the measurement results introduced a size dependency in LA, OWA and WA errors (Figure 6.12). In all cases the mean error decreased, but the 95% CI increased (Table 6.3).

TABLE 6.3: PIG LUNG CUBE 2 AFTER CORRECTION

Mean error	LA	OWA	WA
Before correction (mm^2)	-0.2	1.6	1.8
95% CI limits before calibration	0.7	1.5	1.4
After calibration (mm^2)	-0.1	1.4	1.5
95% CI limits after correction	1.9	4.0	5.5

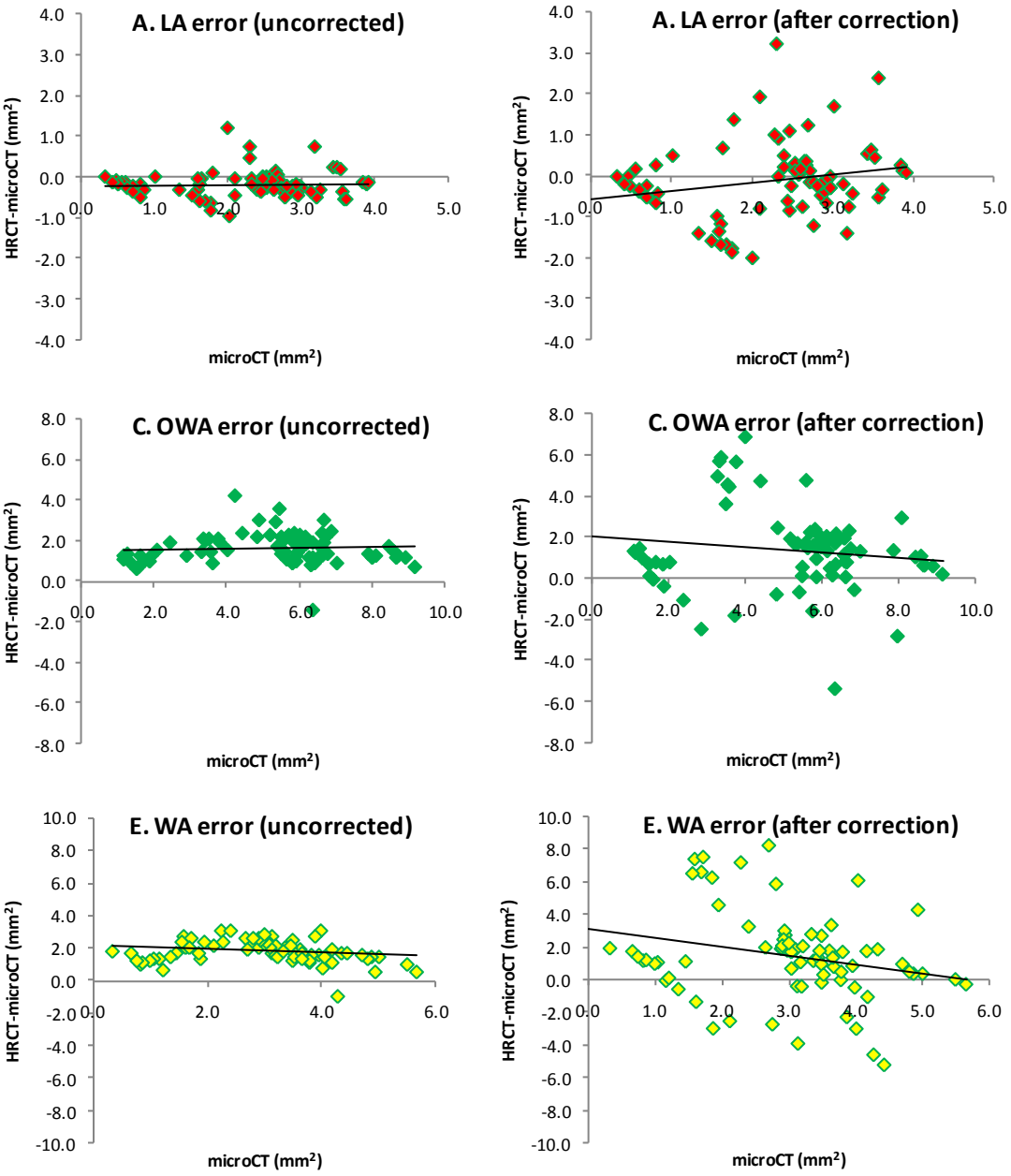

Figure 6.12: Comparison between pre and post corrected pig lung airways

LA (top), OWA (middle) and WA (bottom) errors in various sized airways

6.3 Discussion

6.3.1 Plastic phantom

The results from the plastic phantom validated those from the simulated data. The same patterns of bias and uncertainty were observed. In HRCT images of plastic tubing, the effect of scanning angle on bias and uncertainty followed a similar pattern to the effect of rotation that was hypothesised and then observed in simulated data (Chapter 5). The effect of volume averaging was also similar to that observed in the simulated data.

However, LA, OWA and WA bias at zero degrees was larger than previously observed in Chapter 5 in simulated airways of equivalent size. This was due to the large field of view necessitated by the size of the phantom sponge. The large field of view increased the voxel size imposed during HRCT scanning, reducing the voxel resolution and introducing the size-dependency previously observed in the model data in larger airways. Although redesign of the phantom to allow for a smaller field of view would effectively solve this problem, this does not affect the underlying principle investigated in the thesis. Simply, the smallest detectable structure size is increased, and the correction equations still hold.

Application of the angle and volume averaging correction equations in combination successfully reduced the angle-dependent error in all cases. This was combined with a reversal of the increasing uncertainty associated with pre-corrected area measurements.

Further improvement could have been found by refinement of the experimental technique used during this study.

Measurement errors resulted from difficulty obtaining an accurate estimation of the tube angle. As has been demonstrated with the angle theory in Chapter 4, small changes in the angle at which an airway is measured will have large effects on the airway size measurement. Errors in estimating the true tube size were not expected since they were measured by LM, which can provide an accurate measure of small structures. However this ability depends on the tubing being cut and mounted exactly orthogonally, which was difficult to achieve manually.

In addition, the angle of the phantom during HRCT scanning was estimated using an image of a protractor on the scanning bed. This rough angle estimation was compounded by the residual curvature of the plastic tubes as they passed through the styrofoam, so the angle at which they passed through the Styrofoam was dependent on where in the styrofoam the airways were measured. Both these errors could have

been addressed by an improved phantom. Using plexiglass rather than plastic would ensure a constant angle and mounting the phantom on a pivot would ensure more accurate angle estimation. Additionally, the blurring results in increasing variability which results in angle-dependent uncertainty. This can be countered to some extent by the correction equations or by rotation of the airways back to orthogonal prior to measurement.

Conversion of the HRCT data from 12 bit to 8 bit was found to have no effect on measurement error. This is due to the relatively large differences in density between the wall, the parenchyma and the lumen.

The phantom construction was fairly simple. A phantom such as that created by (Tzeng, Hoffman et al. 2007) would have enabled better measurement of branching patterns. However this was not part of the current study.

6.3.2 Pig lung phantom

Micro-CT validation of HRCT measurements allows quantification of the true airway dimensions found in tissue. Since the dimensions of the airways being measured are much larger than the spatial resolution of the micro-CT, volume averaging effects can be discounted.

This study is the second study to the use of micro-CT in an animal model to validate HRCT airway measurement. The first study by (Dame Carroll, Chandra et al. 2006) used an earlier iteration of the CL algorithm which used max-grad edge detection and did not incorporate the interpolation or the refinements. (Dame Carroll, Chandra et al. 2006) found accuracy 3.2mm^2 LA and 11.2 mm^2 WA, whereas this study improved on this by increasing accuracy to 0.5mm^2 LA and and 5.7 mm^2 WA.

Two pig lung cubes were investigated in this study. One cube was found to have smaller airways than the other. Contrary to expected findings, the cube with larger airways was found to have larger errors. The similar pattern of errors between the different sized airways in the two cubes indicated the repeatability and the suitability of the micro-CT validation technique. The measurement errors observed especially in the first cube could have resulted from poor experimental technique. In future studies, alignment differences between the micro-CT and HRCT datasets could be addressed by the development of automatic registration. Inherent variability in the manual tracing, could be improved by the use of a graphics tablet rather than a mouse.

Prior to correction, little or no size dependency was demonstrated in the algorithm's errors. Deformation and/or drying of the tissue between micro-CT and HRCT scans could be addressed by paraffin-embedding the tissue.

Using a similar validation technique, a previous iteration of the algorithm was demonstrated to have a larger size-dependency (Dame Carroll, Chandra et al. 2006). In addition the algorithm's 95% CI was much higher than the previous iteration. This indicates an improvement in the algorithm's performance.

The bias found in the measurements was indicative of LA under-estimation, and OWA and WA over-estimation. This in accordance with the hypotheses that volume averaging will cause under-estimation of lumen-wall boundary and over-estimation of wall-parenchyma boundary. However, the bias was not found to be size dependent. This is in strong contrast to other similar studies (Dame Carroll, Chandra et al. 2006; (King, Muller et al. 2000) that found systematic size-dependent under-estimation.

In this study the volume averaging relationships were uncovered. Rather than using empirical 'black box' calibrations to correct the errors inherent in the data, the deduced equations governing the confounders found in HRCT data were used to correct the errors. However, after correction, the error 95% limits of agreement increased. This may have been due to errors in the angle calculation, which were dependent on the precision with which the centroid location was estimated. Since the current centroid estimation calculation is inaccurate with small airways, volume averaging corrections cannot currently be performed in these airways

6.4 Conclusions

The results from both phantoms were in accordance with the thesis hypothesis that volume averaging will cause under-estimation of lumen-wall boundary and over-estimation of wall-parenchyma boundary. Use of the deduced correction equations (5.8) and (5.9) presented in the previous chapter has effectively reduced the angle dependent error present in the HRCT phantom data.

The LA measurements were very precise and accurate, which was as expected since the inner lumen wall was easy to define. The OWA was slightly over-estimated, but this may due to the small sample size.

The effect of application of the angle correction was to reduce the accuracy and precision of both the LA and OWA measurements. This was not as expected, but possible explanations for this are as follows:

- airways were found to not be cylindrical although this could have been a result the tissue drying out over time or an artifact produced by the fixation method

- airways are known to taper along their length which would have changed the effect of volume averaging
- alignment problems with the two data sets resulting in increased measurement error
- angle calculations were based on polygon mass centre, which is not an accurate estimate of the airway centroid; this was found to be a problem in airways from the animal lung because airways were bifurcating, leading to a skewing of the angle calculation from the mass centre
- current study only used airways at less than 50 degrees and in these airways angle theory and volume averaging have fewer effects
- airways may have mucosal folding which may not be able to be measured.

The effect of the derived correction equations have been demonstrated using the CL algorithm in a variety of data sets. In the next chapter it will be applied in a clinical setting with the aim of establishing whether these corrections provide improved accuracy and precision of airway measurement.

CHAPTER 7

Application to clinical data

Many studies have compared airway dimension measurements to PFTs, including studies into asthma (Niimi, Matsumoto et al. 2004), COPD (Nakano, Wong et al. 2005) and cystic fibrosis (de Jong, Nakano et al. 2005; Martinez, Llapur et al. 2005). Trials have also investigated the effects on airway dimension of inhaled pharmacological agents, such as methacholine (Brown 2000; Brown, Kaczka et al. 2008), anaesthetics (Brown 2000) and corticosteroids (Niimi 2003).

Chapter 7 tests the usefulness of this thesis' calibrated CL algorithm in a clinical setting. This study used HRCT data obtained as part of a clinical trial evaluating the effect of mannitol in bronchiectasis.

Bronchiectasis is a disease that causes localised, irreversible dilatation of part of the bronchial tree. Involved bronchi are dilated and inflamed, resulting in airflow obstruction and impaired clearance of secretions. Subjects with bronchiectasis usually have increased and persistent mucus secretion (Lourenco, Loddenkemper et al. 1972) and impaired mucociliary transport which results in mucus accumulation, cough and recurrent infections (Currie, Pavia et al. 1987). Bronchiectasis is a debilitating disease and reduces patients' quality of life (Wilson, Jones et al. 1997).

Mannitol dry inhalation powder, under the name Bronchitol, has been approved in the United States by the FDA for use in cystic fibrosis patients with or at risk for bronchiectasis. The original orphan drug indication approved in February 2005 allowed its use for the treatment of bronchiectasis. The original approval was based on the results of Phase II clinical studies showing the product to be safe, well-tolerated, and effective for stimulating mucus hydration/clearance, thereby improving quality of life in patients with chronic obstructive lung diseases like bronchiectasis. Long-term studies are underway as of 2007 to ensure the safety and effectiveness of the treatment (Waknine 2005).

Studies to date have focused on using mannitol for the treatment of asthma (Daviskas, Robinson et al. 2002) and for other diseases (Daviskas, Anderson et al. 2008). As

mannitol is an osmotic agent, it drives water from the airway wall, into the lumen, reducing the viscosity of any mucous present in the lungs and facilitating expellation of the mucous via coughing (Daviskas, Anderson et al. 2008). Although it is clear that mannitol is effective in improving the clearance of mucous, it is not known if there is any effect on airway wall inflammation or airway lumen area. The hypotheses to be tested are that:

- mannitol treatment will result in decrease airway wall area and
- airway lumen area will be increased in patients with bronchiectasis
- the CL algorithm's discriminatory ability would be improved by correction.

7.1 Methods

The study was conducted at the Royal North Shore Hospital as part of a multi-centre clinical trial evaluating the effectiveness of mannitol in the treatment of bronchiectasis. The structure and subject of the study made it suitable for a comparison of the sensitivity and specificity of the candidate airway segmentation algorithm against conventional methods for diagnosing lung disease.

The comparison was made within the mannitol study by conducting both conventional lung function testing (spirometry) and analysis of CT images using the CL algorithm.

7.1.1 Subjects

A sub-group of twelve subjects with stable non-cystic bronchiectasis agreed to undergo baseline and post-treatment HRCT treatment in the clinical trial. Subject characteristics are shown in Table 7.1.

This study was approved by the Ethics Review Committee of Sydney South West Area Health Service (Australia; Protocol No. X05 0259) and was performed under the Clinical Trial Notification Scheme of the Therapeutic Goods Administration of Australia (CTN No. 2005/602). Written informed consent was obtained from all subjects.

7.1.2 Study design

The subjects were randomized into active and placebo groups at a 2:1 ratio. Both groups underwent a 12-week double-blind study of twice daily mannitol or placebo inhalation for 12 weeks. Subjects underwent several types of lung testing including spirometry, mucous clearance studies, and HRCT at the start and the end of the trial.

TABLE 7.1: SUBJECT DETAILS AND BASELINE LUNG FUNCTION VALUES

Subject number	Sex	Age (years)	Height (cm)	Weight (Kg)	FEV1	FVC	FEF 25-75	%fall FEV1 post mannitol
3	M	76	166	54	1.6	2.16	1.19	8.8
4	M	58	163	48	1.3	1.86	0.85	0.8
11	M	59	168	61.5	1.92	3.1	1.05	-16.1
14	F	60	169	76	1.51	1.96	1.27	4.6
16	F	71	156	64	1.54	1.99	1.4	10.4
17	F	56	168	74	1.71	2.6	1.01	-4.1
19	F	65	165	56	1.22	1.78	1.03	3.4
31	M	66	171	85	2.93	3.49	2.67	9.9
5	M	79	174	66	1.44	2.01	0.94	5.6
10	M	64	154	61	1.4	2.03	0.82	5.0
15	F	67	177	87	2.38	3.55	1.41	-4.6
20	F	61	165	88	1.72	2.26	1.38	-4.1

FEV1: forced expiratory volume in one second, FVC: forced vital capacity, FEF25-75: mean forced expiratory flow between 25 and 75% of FVC, F: female, M: Male

Dry powder mannitol

Dry powder mannitol (Pharmaxis Ltd, Frenchs Forest, Australia) was inhaled from capsules using the low resistance dry powder inhaler Osmohaler (RS 01 Plastiape, Osnago-Lecco, Italy). Mannitol was delivered in a dose of 320 mg.

Measurement of lung function

Spirometry was measured using the *SpiroScore+* software (Bird Healthcare Australia). All subjects were clinically stable and had reproducible spirometry.

Measurement of mucous clearance and quality of life

Clearance of mucus was measured by each subject collecting all expectorated sputum over the 24 hours of the day before the visit. Quality of life was assessed using the SF36 self-administered questionnaire scoring system that includes eight independent scales and two main dimensions and has been widely used and validated.

Digital imaging of the lung

HRCT scans were performed with the GE 4-slice Lightspeed HRCT Scanner (GE Medical Systems, Minneapolis) from Aortic arch to diaphragm over 35cm of the whole lung at total lung capacity using a helical protocol (120 kVp, 100 mA and 1.0mm collimation). Images were reconstructed using the GE high spatial frequency 'Lung' algorithm at

field of views ranging from (FOV) of 21 cm to 26 cm. Images were archived in 12-bit dicom format and recorded to CD for later analyses.

Airway measurement by the CL algorithm

In each subject approximately 50 airway measurements from all visible airways from generation three downwards in the right lung presenting at angles less than 75 degrees were measured using the CL algorithm. Branch point identification across a number of adjacent HRCT images in pre- and post-treatment lung scans allowed manual alignment and semi-automatic measurement of airways as described in Figure 3.2. Algorithm parameters were as defined optimal in Chapter 4. Measurements were corrected for angle and volume averaging using the equations presented in Chapter 5.

7.1.3 Statistical analysis

Since the image locations were matched pre- and post-mannitol or placebo treatment, changes in LA and WA could be calculated for each subject. Paired T-tests were used to examine the changes within each subject for significance. Results grouped by treatment (active or placebo) were presented as mean ± standard error the mean, and differences between these groups were tested for significance using unpaired t-tests.

7.1 Results

7.1.1 Primary outcomes

There were no significant changes in FEV1 following treatment with mannitol (1.79 ± 0.54 and 1.75 ± 0.51L) or with placebo (1.74 ± 0.45L and 1.74 ± 0.54L).

However, highly significant improvement in quality of life after 12 weeks of treatment with Bronchitol ($p< 0.005$) and a significant improvement in quality of life compared to placebo ($p< 0.05$) was obtained.

In addition, there was a highly significant difference in mucus clearance at 12 weeks for patients receiving Bronchitol versus those patients receiving placebo ($p<0.001$).

7.1.2 HRCT visual inspection

On examination of HRCT images of the subjects' lungs, the airways were characteristically thickened and dilated. It was noted that airway plugging with mucous often occurred (Figure 7.1). Airways with plugging were not measured with the CL algorithm.

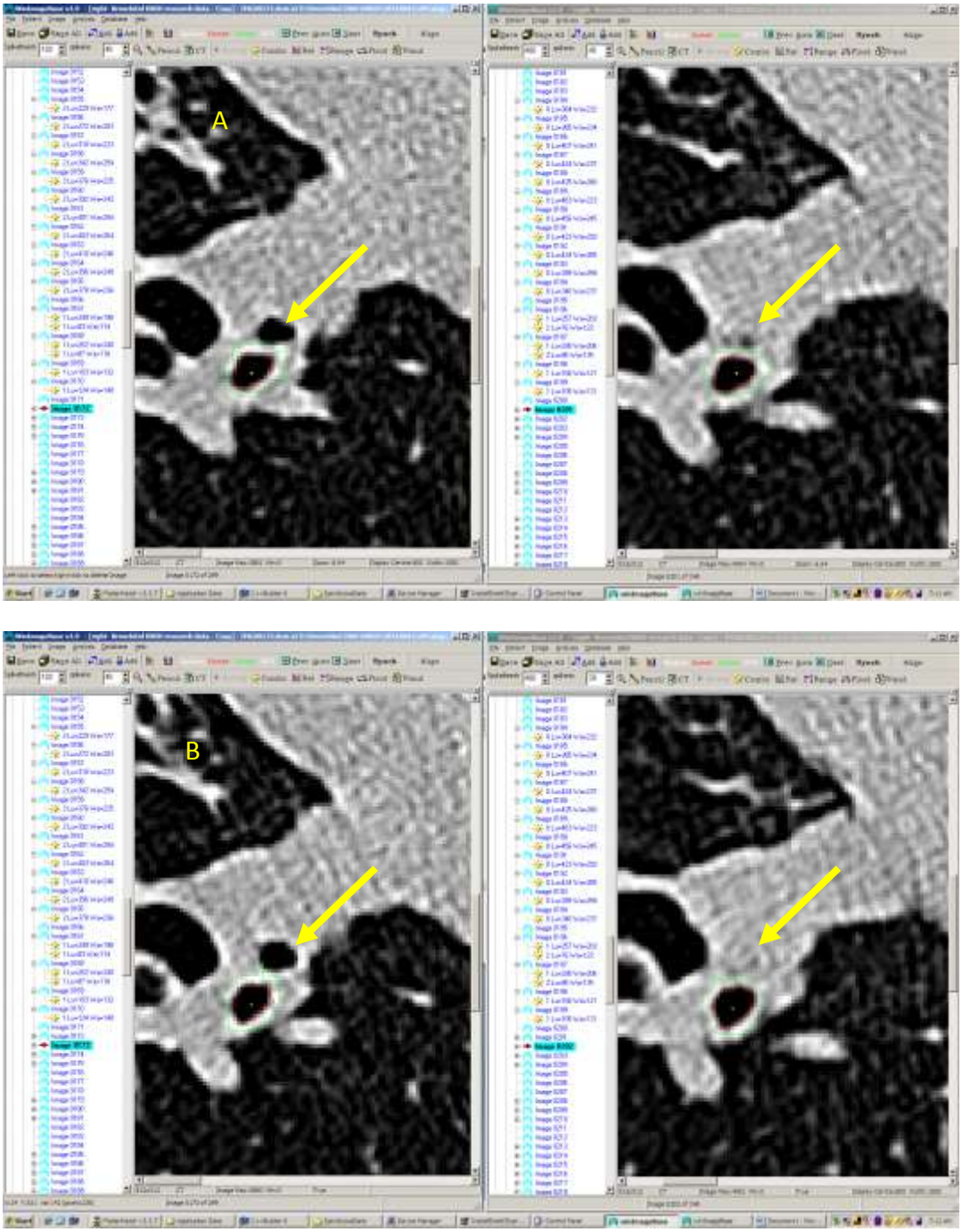

Figure 7.1: Example HRCT images of mucous plugging in bronchiectasis

Airway segmentation with the outer wall in green and inner wall in red. Notice the apparent disappearance of the airway seen on the left (A) airway partially obscured by mucous and (B) airway fully obscured by mucous. These airways were excluded from analysis.

Distribution of airway dimensions

When the distributions of LA and OWA were examined, it was evident that neither the airway lumen nor the airway walls were normally distributed. Before and after

treatment the median lumen area was 2.7mm^2 and the wall area was 3.6mm^2. The treatment appeared to have little or no effect on the distribution of lumen area.

7.1.3 HRCT wall caliber

To test whether treatment had affected airway caliber the relative amount of wall was calculated.

In Figure 7.2 it can be seen that the proportion of the total area that the wall area makes up is dependent on the size of the airway. Both results are comparable with the existing literature, for instance in subjects with cystic fibrosis (Martinez, Llapur et al. 2005).

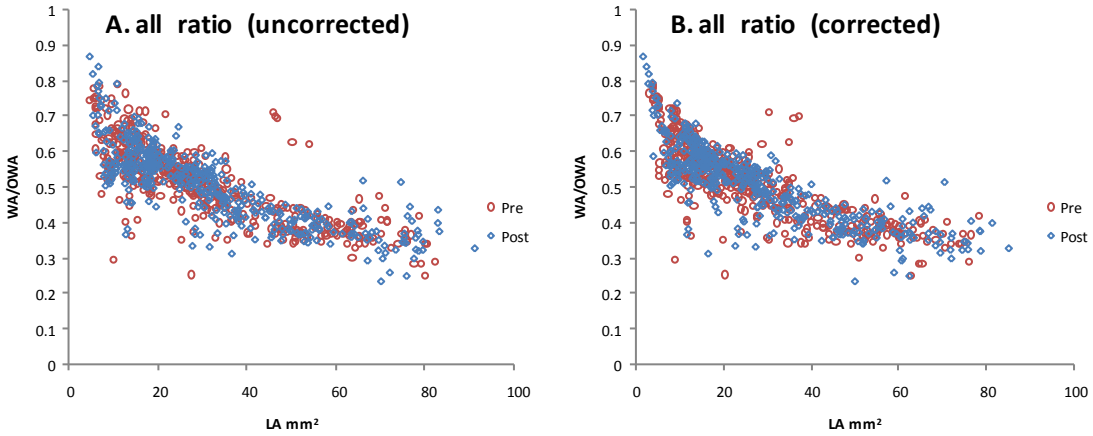

Figure 7.2: Effect of treatment on airway calibre

When the data was further stratified into the active and placebo groups, due to the small number of samples in the groups no significant difference could be observed (Figure 7.3). This relationship was not affected by the treatment (graph not shown).

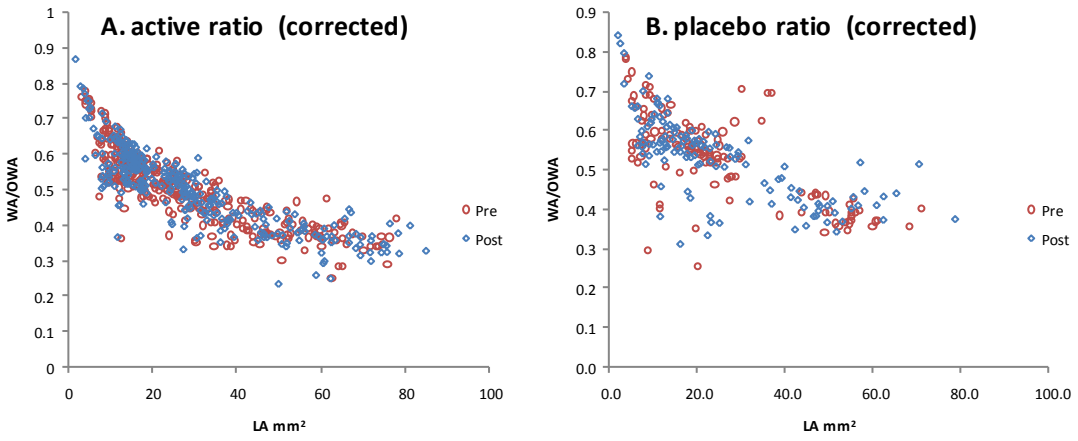

Figure 7.3: Effect of treatment on airway calibre (grouped)

7.1.4 HRCT wall to lumen relationship

To investigate whether the treatment had any effect on the lumen to wall area relationships in these subjects, the active and placebo groups were plotted as correlations in Figure 7.4. There was a strong linear relationship between lumen and wall area (R-squared >0.88) but no effect was observed with treatment in either group.

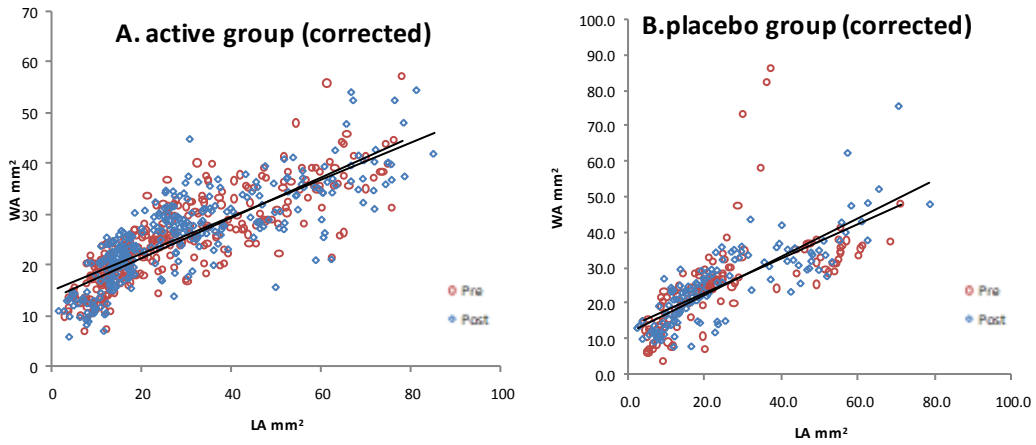

Figure 7.4: Treatment has no effect on WA to OWA relationship

Figure 7.5 was plotted to investigate whether correction had improved the correlation between the pre-treatment and post-treatment measurements. It appeared that both lumen and wall areas appeared more widely distributed as a result of correction, although some of the outliers were removed by the correction process.

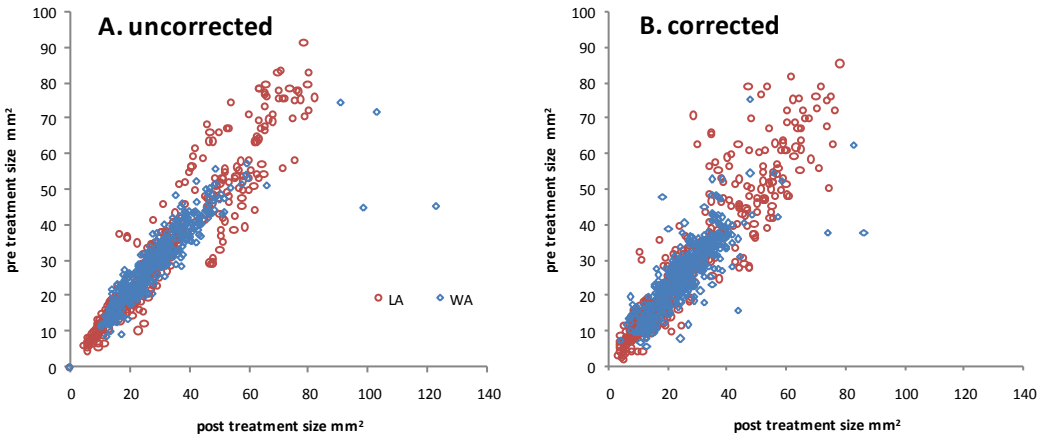

Figure 7.5: Effect of correction on regression relationship in LA and WA in all data

HRCT analysis by subject

Table 7.2 below presents a summary of the mannitol study results, separating the subjects into two groups, 'Active' and 'Placebo'. Table 7.2 over-leaf presents the 'Direction of change' as 'up' or 'down' if the magnitude of the mean differences were greater than the 95% CI identified for the corrected CL results when applied to the animal model in Chapter 6 (Table 6.3). The table is separated into two parts, before correction and after correction to assess the effect of correction on the results.

Before correction, of the eight subjects that form the Active group, five increased in lumen area and three decreased. After correction, two increased in lumen area, one decreased and five showed no change. Similarly, in the placebo group before correction, three subjects had decreases in LA and one increased. After correction in the placebo group, one increased, two decreased, and one showed no change. Before correction in the active group, six had no change in WA and two decreased, whereas in the placebo group two had no change and two decreased. Interestingly, after correction no changes were observable in the WA measurements.

When paired T-tests were used to test the changes in wall and lumen area between the two groups, Active and Placebo, for significance, post-treatment differences ($P<0.05$) emerged, both up and down, in the LA and WA in some subjects in both groups.

Before correction, two of the subjects in the active group had significant decreases in LA. Four had significant increases in LA, with two of these four also having significant increases in WA. All of the placebo group had significant changes in LA, with one subject having an increase and three having decreases. One subject had a significant decrease in WA. Correction had little effect on the significance of these changes, except in WA where there was no significant change.

Both before and after correction, the subjects' LA and WA measurements compared pre- and post-treatment in Table 7.2 reflect variable study results. After correction the results become clearer since the signal: noise ratio becomes higher. That is although the correction results in higher noise it also increases the signal. For example, when examining the placebo subjects we can see that before correction there are significant differences both up and down between the pre and post treatment groups. After correction, the significance was removed and so was the direction of change.

TABLE 7.2: LA AND WA IN BRONCHIECTASIS PATIENTS BEFORE AND AFTER MANNITOL TREATMENT

Before correction

Patient		Lumen area (mean)				Wall area (mean)			
ID	*Treatment*	*Pre*	*Post*	*T-test*	*Direction of change*	*Pre*	*Post*	*T-Test*	*Direction of change*
3	Active	33.7	34.6	0.32703	Up	27.8	26.9	0.13028	None
4	Active	28.6	27.7	0.00027	Down	24.2	23.8	0.16526	None
11	Active	44.9	41.4	0.01714	Down	34.6	34.4	0.71316	None
14	Active	23.8	30.8	0.00000	Up	25.1	26.6	0.01949	Up
16	Active	26.4	27.5	0.03256	Up	27.7	27.4	0.40529	None
17	Active	19.7	20.9	0.00061	Up	23.5	28.3	0.00000	Up
19	Active	42.5	42.0	0.21187	Down	36.5	37.1	0.19402	None
31	Active	31.1	35.9	0.00000	Up	28.5	29.4	0.06439	None
5	Placebo	25.7	24.6	0.00625	Down	24.9	23.6	0.02666	Down
10	Placebo	24.1	19.5	0.00000	Down	29.9	29.5	0.33365	None
20	Placebo	43.8	39.0	0.00097	Down	36.5	36.8	0.72862	None
15	Placebo	21.0	27.8	0.00000	Up	31.3	27.6	0.16573	Down

After correction

Patient		Lumen area (mean)				Wall area (mean)			
ID	*Treatment*	*Pre*	*Post*	*T-test*	*Direction of change*	*Pre*	*Post*	*T-Test*	*Direction of change*
3	Active	32.1	32.2	0.92484	None	26.3	24.7	0.23426	None
4	Active	26.4	25.3	0.01918	Down	20.1	19.8	0.50562	None
11	Active	41.6	38.2	0.01738	Down	29.4	29.0	0.66356	None
14	Active	21.5	27.9	0.00003	Up	22.1	25.0	0.00380	None
16	Active	25.3	26.3	0.07170	None	24.2	22.2	0.00909	None
17	Active	18.0	18.9	0.04102	None	20.2	24.6	0.00000	None
19	Active	39.1	38.6	0.41746	None	31.6	32.8	0.07364	None
31	Active	26.0	31.7	0.00001	None	26.2	27.9	0.10434	None
5	Placebo	23.9	22.3	0.01172	None	21.6	20.1	0.07581	None
10	Placebo	20.7	16.6	0.00003	Down	24.5	24.4	0.86006	None
20	Placebo	39.9	35.6	0.00144	Down	31.7	32.1	0.64725	None
15	Placebo	15.8	23.6	0.00009	Up	24.2	23.4	0.67917	None

7.1.5 HRCT analysis by group

To evaluate whether any difference was observable as a result of correction between the active and placebo groups, the mean and standard error of LA, OWA and WA was calculated for each group (Figure 7.6).

Before correction, significant increases were found in LA, OWA and WA in the active group (Figure 7.6A) and significant decreases in OWA and WA in the placebo group (Figure 7.6B). After correction, significant increases remained in the active group (Figure 7.6C) but were absent from the placebo group (Figure 7.6D).

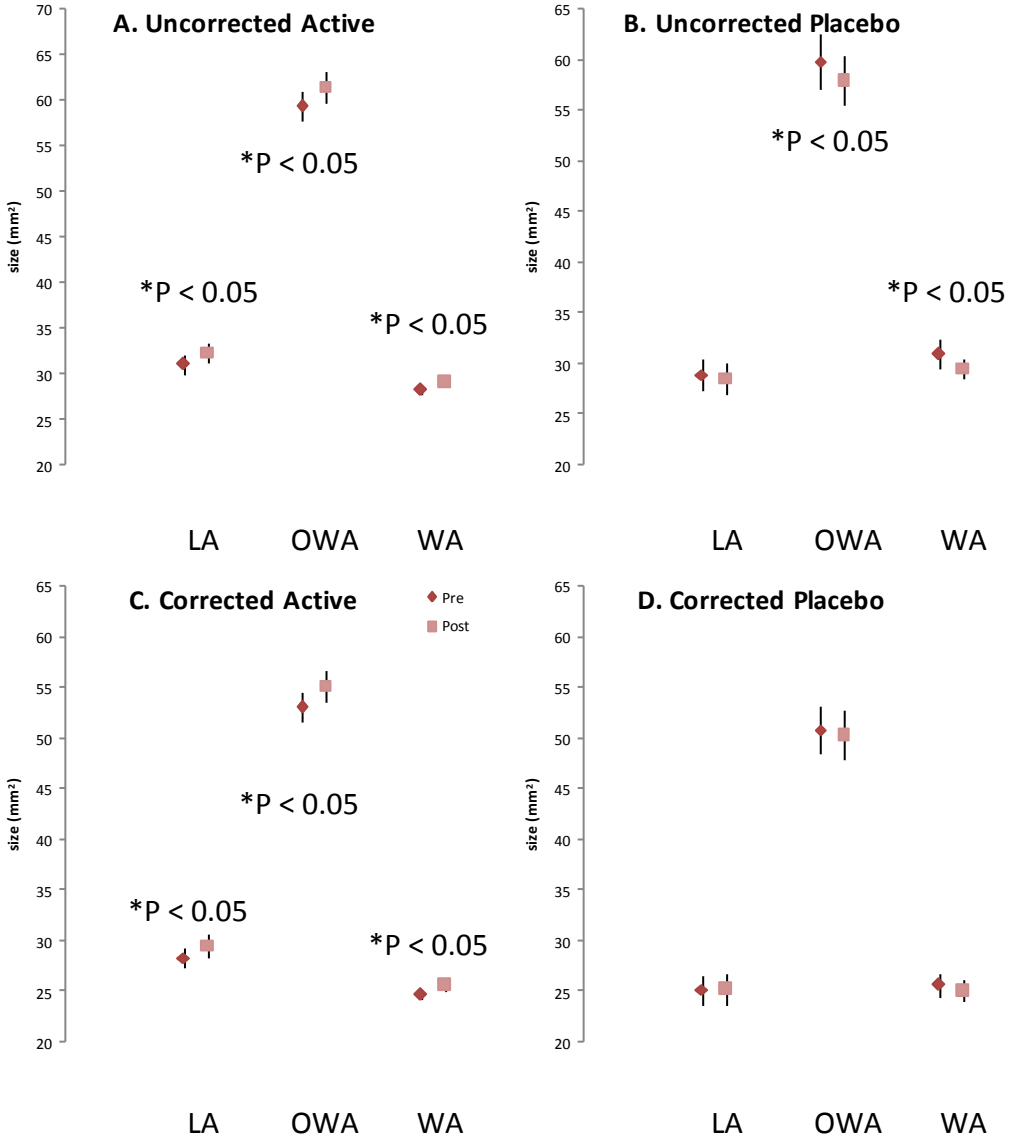

Figure 7.6: Effect of treatment on airway dimensions in the mannitol study

Mean LA, OWA and WA in Active (A, C) and the eight Placebo (B, D) subjects pre and post treatment with and without correction Values expressed as mean size for 311 (active) and 129 (placebo) individual measurements, with error bars as standard error.

To test whether the correction allowed any greater discrimination between the two independent active and placebo groups, unpaired t-tests were carried out (Table 7.3).

In the uncorrected measurements before treatment there was no detectable significant difference between the active and placebo groups for LA and OWA. However there was a significant difference in the WA measurements. After treatment with mannitol, no significant difference could be observed between the active and placebo groups.

In the corrected measurements no significant difference was found between the active and placebo groups before treatment. However, after treatment with mannitol, the corrected measurements indicated that there was a significant difference between the active LA and placebo LA.

TABLE 7.3: DIFFERENCES BETWEEN ACTIVE AND PLACEBO GROUPS

	PRE-TREATMENT			POST-TREATMENT		
	LA	OWA	WA	LA	OWA	WA
Uncorrected	0.265	0.890	0.044	0.063	0.257	0.763
Corrected	0.094	0.425	0.368	0.031	0.095	0.619

unpaired T-Test comparison (0<p<1). Significant changes are shown in red

To probe the reasons for these significant changes further analysis was performed. Percentage changes were calculated for the two groups (Table 7.4). Correction caused an increase in both the magnitude and standard deviation of the LA change. It was notable that the effect of correction was larger in the active group than the placebo group.

TABLE 7.4: % CHANGE FOR THE ACTIVE AND PLACEBO GROUPS BEFORE AND AFTER CORRECTION

	Active			Placebo		
	LA	OWA	WA	LA	OWA	WA
Uncorrected	-2.3±15.2	0.2±12.5	0.3±13.4	-5.2±26.0	-4.6±16.0	-4.3±15.7
Corrected	-6.9±24.0	-3.3±19.9	-4.2±24.5	-6.1±41.1	-5.5±27.2	-6.0±31.2

Results expressed as mean ± standard deviation

7.2 Discussion

7.2.1 Effect of mannitol

Visual inspection of the images clearly showed mucous plugs in the airways before and after treatment with mannitol. As with similar HRCT studies where mucous secretions are present (de Jong, Nakano et al. 2005) airways that were plugged with mucous were excluded from analysis. Since airway measurement was not carried out on airways that were plugged, some of the mannitol-induced change may have been missed by the CL algorithm.

The effect of the mannitol on airways was not detectable using routine lung function testing but with the CL algorithm, significant increases in the LA of the active group and no change in WA were detected. This may have not been as a result of the mannitol but instead an artifact of the low patient number and the high number of airways measured. These results were interesting but not definitive, and the significance of the changes observed with mannitol needs further clarification from a larger study. This pilot data, although not conclusive, is the first step in larger multi-centre study which will be undertaken shortly.

7.2.2 Effect of correction

Correction of the CL algorithm increased the variability of the data. It also increased the differences between the active and placebo groups, resulting in a significant difference in LA between the active and placebo groups. Interestingly, after correction of the CL algorithm, the differences remained significant for the mannitol treated group but became non-significant for the placebo group. Despite the low subject numbers, this result may indicate that the correction equations have increased the discriminatory ability of the HRCT test.

As stated in the discussion of the previous chapter, the correction assumes accurate placement of the airway centroid and the method for centroid identification needs further refinement. The noise variance in the correction method may have masked part of the mannitol-induced change. Further study is required with a larger group of subjects and a pharmacological agent (such as methacholine) with known effects on airway lumen and wall area. This will allow measurement changes to be correlated against standard lung function test results and the effect of correction to be better quantified facilitating an improved correction technique.

CHAPTER 8

Conclusion

This thesis has revealed relationships between variables that were not separable in previous studies. By examining the volume averaging and angle of rotation relationships separately and in total, the thesis has enabled a better understanding of the relative contributions of each confounder to the total error. The finding that even when airway orientation angles are relatively high, the contribution of volume averaging to overall measurement error is relatively small is important and significant. Better understanding of the confounders of HRCT measurement error will enable future airway measurement studies to be designed and carried out with more certainty.

Many previous studies have used variations of the ray-casting technique but to date none have examined the effect of the underlying parameters governing this algorithm, with qualitative best-guesses being used. The thesis sought to characterise and improve the performance of the ray-casting algorithm in HRCT data. Selection of parameters such as interpolation, edge-detection and the number of rays used as well as the development of novel refinements enabled optimal performance, in terms of speed, accuracy and precision from this algorithm in 2-D simulated data. When tested in pig lung phantom data this resulted in a large improvement in algorithm precision and accuracy when compared to a non-optimised ray-casting algorithm (Dame Carroll, Chandra et al. 2006) and similar algorithms that were tested in this way (King, Muller et al. 2000; Nakano, Whittall et al. 2002).

A series of validation steps were carried out in 3-D simulated and phantom data. Novel correction equations were demonstrated in rotated and averaged airways from a number of types of data. In all cases in simulated data the equations effectively removed the measurement error, validating the derivations. The correction equations presented here could be used for calibration of the airway measurements obtained from HRCT data. To date, HRCT data has not been used for airway measurement unless the airways present orthogonally to the scanning plane. These corrections open up the possibility of using angled airways for the first time. However, important constraints

relating to the angle and airway size at any level of averaging apply. For instance, this investigation has found that whichever measurement technique is used, airways at an angle of 75 degrees or more will have a disproportionate measurement bias. At this level of rotation, further bias created by increased volume averaging could not be countered. Therefore in highly averaged data such as HRCT, airways oblique to the scanning plane should be avoided.

In HRCT plastic phantom data similar airway orientation and volume averaging error relationships were also found. Application of the correction equations resulted in increased precision and accuracy. However, in the micro-CT dataset, correction resulted in increased measurement precision and accuracy. This reflected the need to improve the micro-CT validation method by registration of the micro-CT data set onto the HRCT data. Misalignment errors were found to exacerbate the angle estimation errors, resulting in decreased precision and precision after correction.

This thesis has uncovered that post-processing of the HRCT data to re-orientate the data back to the orthogonal angle is more effective than measuring airways as they present in the simulated data and the plastic phantom. However, due to difficulties in calculating the airway angle with high accuracy, this step was not carried out in the pig lung phantom and it is not clear whether this step translates well into clinical usage.

Correction in the Bronchitol data increased the variance in WA measurements, and this finding is in keeping with the pig lung data. Before the correction equations can be applied in clinical data, the angles need accurate calculation. Until this is achieved the Bronchitol data should be interpreted using the uncorrected values.

The validation protocol developed in this thesis can be used for comparative studies of algorithm performance. In particular, the micro-CT validation technique provides a true 3-D dataset, which has been used to validate HRCT airway measurements (Dame Carroll, Chandra et al. 2006). This thesis extended the micro-CT validation previously developed by using a simpler approach to fixation, although further studies are required to establish the reproducibility of the technique.

The advent of *winImageBase* has enabled researchers to explore airway disease in new ways (Brown 2008; Carroll 2008). As *winImageBase* emerged as a commercially viable product it became apparent that most users were interested in pre/post treatment analysis. Here the most promising avenue for further studies are to identify the airways that can act as leading indicators of treatment effect. Although *winImageBase* can be used very successfully for pre/post treatment analysis it was not designed specifically for this role. Most of the actual work for pre/post treatment analysis involves the identification of suitable study volunteers and collection of appropriate

data sets; combining leading airways and identifying bifurcations. For this we really require a separate 3-D software tool which can act as an image reslicer. Moreover, this thesis has shown that for activities such as determining the centroid other, possibly faster, algorithms, for example mass centre, can also be profitably used. There is also the interesting question of extending the CL algorithm to identify bifurcations. Ideally, all these analysis tools should be combined into a software platform specifically designed for airway tree analysis.

Continued improvement in quantitative image-analysis techniques and the use of spirometrical control of the lung volume at acquisition make it possible to more easily assess airways lumen and wall areas and lung density. This quantitative assessment of the airways will lead to the increasing use of CT as a research tool for better insights in physiopathology of obstructive lung disease, particularly in COPD and asthma, with an ultimate benefit in clinical practice.

CT analysis of airway dimensions in asthma provides additional data to that derived from traditional measures of lung function. Although much work remains to be done in terms of standardising the approach to image acquisition and analysis, there is some evidence that CT may be a more sensitive end-point in clinical trials. As important questions remain to be answered for this common disease, the use of CT in research settings seems justified. The relationship between airway hyper-responsiveness and airway wall dimension (as assessed by CT) remains unclear and is a topic that requires more study, as does the contribution of airway wall dimensions to the wide variation in airway responsiveness that can be demonstrated in normal individuals. Further work is needed that relates the degree of airway remodelling (as measured by histology) to the degree of airway wall thickening (as measured by HRCT) in subjects with asthma and COPD.

References

Amirav, I., S. S. Kramer, et al. (1993). "Assessment of methacholine-induced airway constriction by ultrafast high-resolution computed tomography." Journal of Applied Physiology **75**(5): 2239-2250.

Asia Pacific, C. R. G. (2005). "Global Initiative for Chronic Obstructive Lung Disease strategy for the diagnosis, management and prevention of chronic obstructive pulmonary disease: an Asia-Pacific perspective." Respirology **10**(1): 9-17.

Aykac, D., E. A. Hoffman, et al. (2003). "Segmentation and analysis of the human airway tree from three-dimensional X-ray CT images." IEEE Transactions on Medical Imaging **22**(8): 940-50.

Beachey, W. (2007). "Respiratory Care Anatomy and Physiology: Foundations for Clinical Practice." Mosby; 2 edition (January 22, 2007).

Berend, N. (2001). "Epidemiological survey of chronic obstructive pulmonary disease and alpha-1-antitrypsin deficiency in Australia." Respirology **6 Suppl**: S21-5.

Berger, P., V. Perot, et al. (2005). "Airway wall thickness in cigarette smokers: quantitative thin-section CT assessment." Radiology **235**(3): 1055-64.

Bergeron, C., M. K. Tulic, et al. (2007). "Tools used to measure airway remodelling in research." European Respiratory Journal **29**(3): 596-604.

Berry, E. (2008). "A practical Approach to Medical Image Processing." (Published by CRC Press. ISBN 13:978-1-58488-824-6).

Bland, J. M. and D. G. Altman (1986). "Statistical methods for assessing agreement between two methods of clinical measurement." Lancet **1**: 307-310.

Bland, J. M. and D. G. Altman (1996). "Measurement error." British Medical Journal: 313-744.

Bland, J. M. and D. G. Altman (2003). "Applying the right statistics: analyses of measurement studies." Ultrasound in Obstetrics & Gynecology **22**(1): 85-93.

Brealey, S. (2001). "Measuring the effects of image interpretation: an evaluative framework.[see comment]." Clinical Radiology **56**(5): 341-7.

Brenner, D. J., E. J. Hall, et al. (2007). "Computed tomography--an increasing source of radiation exposure.[see comment]." New England Journal of Medicine **357**(22): 2277-84.

Brown, N. (2008). "Airway distensibility in asthma." PhD thesis: Sydney University.

Brown, R. H. (2000). "HRCT imaging of airway responsiveness: effects of anesthetics." Journal of Clinical Monitoring & Computing **16**(5-6): 443-55.

Brown, R. H., D. W. Kaczka, et al. (2008). "Temporal variability in the responses of individual canine airways to methacholine." Journal of Applied Physiology **104**(5): 1381-6.

Brown, R. H., N. Scichilone, et al. (2001). "High-Resolution Computed Tomographic Evaluation of Airway Distensibility and the Effects of Lung Inflation on Airway Caliber in Healthy Subjects and Individuals with Asthma." American Journal of Respiratory Critical Care Medicine **163**(4): 994-1001.

Burrowes, K. S., A. J. Swan, et al. (2008). "Towards a virtual lung: multi-scale, multi-physics modelling of the pulmonary system." Philosophical Transactions of the Royal Society London, Series a (Mathematical, Physical & Engineering Sciences) **366**(1879): 3247-63.

Camiciottoli, G., M. Bartolucci, et al. (2006). "Spirometrically Gated High-Resolution CT Findings in COPD*." Chest **129**(3): 558-564.

Carroll, J. (2008). "Greater heterogeneity of airway narrowing and closure in asthma " PhD thesis: Sydney University.

Carroll, N., J. Elliot, et al. (1993). "The structure of large and small airways in nonfatal and fatal asthma." American Review of Respiratory Disease **147**(2): 405-10.

Catallo, W. J., C. H. Kennedy, et al. (2001). "Combustion products of 1,3-butadiene are cytotoxic and genotoxic to human bronchial epithelial cells." Environmental Health Perspectives **109**(9): 965-71.

Chiverton, J. P. and K. Wells (2004). Volumetric partial volume quantification via a statistical model of 3-D voxel gradient magnitude. Nuclear Science Symposium Conference Record, 2004 IEEE.

Cooper, C. and K. Little (1979). "Casualty x-rays." British Journal of Hospital Medicine **22**(6): 633.

Corcoran, H. L., W. R. Renner, et al. (1992). "Review of high-resolution CT of the lung." Radiographics **12**(5): 917-939.

Cormack, A. (1963). "Representation of a function by its line integrals, with some radiological applications." Journal of Applied Physics **34**(9): 2722-7.

Cowin, S. (2001). "Bone Mechanics Handbook." 9-5.

Currie, D. C., D. Pavia, et al. (1987). "Impaired tracheobronchial clearance in bronchiectasis." Thorax **42**(2): 126-30.

Dame Carroll, J. R., A. Chandra, et al. (2006). "Airway dimensions measured from micro-computed tomography and high-resolution computed tomography." European Respiratory Journal **28**(4): 712-20.

Daviskas, E., S. D. Anderson, et al. (2008). "Effect of increasing doses of mannitol on mucus clearance in patients with bronchiectasis." European Respiratory Journal **31**(4): 765-72.

Daviskas, E., M. Robinson, et al. (2002). "Osmotic stimuli increase clearance of mucus in patients with mucociliary dysfunction." Journal of Aerosol Medicine **15**(3): 331-41.

de Jong, P. A., N. L. Muller, et al. (2005). "Computed tomographic imaging of the airways: relationship to structure and function." European Respiratory Journal **26**(1): 140-52.

de Jong, P. A., Y. Nakano, et al. (2005). "Changes in airway dimensions on computed tomography scans of children with cystic fibrosis." American Journal of Respiratory & Critical Care Medicine **172**(2): 218-24.

Djukanovic, R. and R. Djukanovic (2002). "Airway inflammation in asthma and its consequences: implications for treatment in children and adults." Journal of Allergy & Clinical Immunology **109**(6 Suppl): S539-48.

Dodd, J. and N. L. Muller (2006). "Conventional high-resolution CT versus helical high-resolution MDCT in the detection of bronchiectasis." American journal of roentgenology **187**(2): 414-420.

Dougherty, R. H. and J. V. Fahy (2009). "Acute exacerbations of asthma: epidemiology, biology and the exacerbation-prone phenotype." Clinical & Experimental Allergy **39**(2): 193-202.

Enright, P. and M. McCormack (2008). "Assessing the airways." Chronic Respiratory Disease **5**(2): 115-9.

Farncombe, T. H. (2008). "Software-based respiratory gating for small animal conebeam CT." Medical Physics **35**(5): 1785-1792.

Fatz, D. (2004). "Digital X-Ray: The Market in Focus." Theta reports **1241**: 3.

Ford, N. L., M. M. Thornton, et al. (2003). "Fundamental image quality limits for microcomputed tomography in small animals." Medical Physics **30**(11): 2869-2877.

Frith, P. A., P. A. Cafarella, et al. (2008). "Chronic obstructive pulmonary disease (COPD) is a major personal and public health burden in Australia." Australian & New Zealand Journal of Public Health **32**(2): 139-41.

Gevenois, P. A., P. De Vuyst, et al. (1996). "Comparison of computed density and microscopic morphometry in pulmonary emphysema." American Journal of Respiratory Critical Care Medicine **154**(1): 187-192.

Gomez, F. P., R. Rodriguez-Roisin, et al. (2002). "Global Initiative for Chronic Obstructive Lung Disease (GOLD) guidelines for chronic obstructive pulmonary disease." Current Opinion in Pulmonary Medicine **8**(2): 81-6.

Grenier, P. A., C. Beigelman-Aubry, et al. (2003). "Multidetector-row CT of the airways." Seminars in Roentgenology **38**(2): 146-57.

Hart, D. and B. F. Wall (2004). "UK population dose from medical X-ray examinations." European Journal of Radiology **50**(3): 285-91.

Hogg, J. C., P. T. Macklem, et al. (1968). "Site and nature of airway obstruction in chronic obstructive lung disease." New England Journal of Medicine **278**(25): 1355-60.

Holdsworth, D. W. and M. M. Thornton (2002). "Micro-CT in small animal and specimen imaging." Trends in Biotechnology **20**(8): S34-S39.

Hopper, K. D., T. A. Iyriboz, et al. (1998). "CT bronchoscopy: optimization of imaging parameters." Radiology **209**(3): 872-7.

Hounsfield, G. N. (1973). "Computerized transverse axial scanning (tomography): Part I. Description of system. ." British Journal of Radiology **46**: 1016-1002.

Hsieh, J. (1999). "Nonlinear partial volume artifact correction in helical CT." Nuclear Science, IEEE Transactions on **46**(3): 743-747.

James, A. L., P. S. Maxwell, et al. (2002). "The relationship of reticular basement membrane thickness to airway wall remodeling in asthma." American Journal of Respiratory & Critical Care Medicine **166**(12 Pt 1): 1590-5.

Jones, A. S., A. Reztsov, et al. (2007). "Application of invariant grey scale features for analysis of porous minerals." Micron **38**(1): 40-48.

Khaled, N., D. Enarson, et al. (2001). "Chronic respiratory diseases in developing countries: the burden and strategies for prevention and management." Bulletin of the World Health Organization **79**(10).

King, G. G., J. D. Carroll, et al. (2004). "Heterogeneity of narrowing in normal and asthmatic airways measured by HRCT.[see comment]." European Respiratory Journal **24**(2): 211-8.

King, G. G., N. L. Muller, et al. (1999). "Evaluation of airways in obstructive pulmonary disease using high-resolution computed tomography." American Journal of Respiratory & Critical Care Medicine **159**(3): 992-1004.

King, G. G., N. L. Muller, et al. (2000). "An analysis algorithm for measuring airway lumen and wall areas from high-resolution computed tomographic data." American Journal of Respiratory & Critical Care Medicine **161**(2 Pt 1): 574-80.

Kitaoka, H. and H. Kitaoka (2002). "Computational morphology of the lung and its virtual imaging." European Journal of Radiology **44**(3): 164-71.

Kraft, E. and N. Finby (1980). "Rontgen's discovery of X-ray and Lenard's priority claim; award of first Nobel Prize in physics in 1901." New York State Journal of Medicine **80**(10): 1623-5.

Lamprecht, B., L. Schirnhofer, et al. (2008). "Non-reversible airway obstruction in never smokers: results from the Austrian BOLD study." Respiratory Medicine **102**(12): 1833-8.

Langheinrich, A. C., B. Leithauser, et al. (2004). "Acute Rat Lung Injury: Feasibility of Assessment with Micro-CT." Radiology: 2331031340.

Lourenco, R. V., R. Loddenkemper, et al. (1972). "Patterns of distribution and clearance of aerosols in patients with bronchiectasis." American Review of Respiratory Disease **106**(6): 857-66.

Madau, D. P. (2008). "An architecture for designing reusable embedded systems software." http://www.embedded.com/design/opensource/.

Maher, M. M., M. K. Kalra, et al. (2004). "Application of rational practice and technical advances for optimizing radiation dose for chest CT." Journal of Thoracic Imaging **19**(1): 16-23.

Mansour, M. E., B. P. Lanphear, et al. (2000). "Barriers to Asthma Care in Urban Children: Parent Perspectives." Pediatrics **106**: 512-519.

Martinez, T. M., C. J. Llapur, et al. (2005). "High-resolution computed tomography imaging of airway disease in infants with cystic fibrosis." American Journal of Respiratory & Critical Care Medicine **172**(9): 1133-8.

Matsuoka, S., Y. Kurihara, et al. (2005). "Serial change in airway lumen and wall thickness at thin-section CT in asymptomatic subjects." Radiology **234**(2): 595-603.

McLennan, G., E. Namati, et al. (2007). "Virtual Bronchoscopy." Imaging Decisions MRI **11**(1): 10-20.

McNamara, A. E., N. L. Muller, et al. (1992). "Airway narrowing in excised canine lungs measured by high-resolution computed tomography." Journal of Applied Physiology **73**(1): 307-16.

McNitt-Gray, M. F., J. G. Goldin, et al. (1997). "Development and testing of image-processing methods for the quantitative assessment of airway hyperresponsiveness from high-resolution CT images." Journal of Computer Assisted Tomography **21**(6): 939-47.

McParland, B. E., P. T. Macklem, et al. (2003). "Airway wall remodeling: friend or foe?" Journal of Applied Physiology **95**(1): 426-34.

Minasian, C., C. Wallis, et al. (2008). "Bronchial provocation testing with dry powder mannitol in children with cystic fibrosis." Pediatric Pulmonology **43**(11): 1078-84.

Mori, I. (1986). "US Patent No. 4630202."

Mori, K., J. Hasegawa, et al. (1996). "Recognition of bronchus in three-dimensional X-ray CT images with application to virtualized bronchoscopy system." Proceedings of the International Conference on Pattern Recognition **7276**: 528-532.

Nakano, Y., N. L. Muller, et al. (2002). "Quantitative assessment of airway remodeling using high-resolution CT." Chest **122**(6 Suppl): 271S-275S.

Nakano, Y., S. Muro, et al. (2000). "Computed tomographic measurements of airway dimensions and emphysema in smokers. Correlation with lung function." American Journal of Respiratory & Critical Care Medicine **162**(3 Pt 1): 1102-8.

Nakano, Y., K. P. Whittall, et al. (2002). "Development and validation of human airway analysis algorithm using multidetector row CT." Society of Photo-Optical Instrumentation Engineers (SPIE) Conference Series **4683**: 460-469.

Nakano, Y., J. C. Wong, et al. (2005). "The prediction of small airway dimensions using computed tomography." American Journal of Respiratory & Critical Care Medicine **171**(2): 142-6.

Nakata, H., T. Kimoto, et al. (1985). "Diffuse peripheral lung disease: evaluation by high-resolution computed tomography." Radiology **157**(1): 181-185.

Niimi, A., H. Matsumoto, et al. (2004). "Clinical assessment of airway remodeling in asthma: utility of computed tomography." Clinical Reviews in Allergy & Immunology **27**(1): 45-58.

Ohara, T., T. Hirai, et al. (2006). "Comparison of airway dimensions in different anatomic locations on chest CT in patients with COPD." Respirology **11**(5): 579-85.

Palagyi (2003). "Quantitative Analysis of Intrathoracic Airway Trees: Methods and Validation. In Information Processing in Medical Imaging. ISBN 978-3-540-40560-3."

Palagyi, K., J. Tschirren, et al. (2006). "Quantitative analysis of pulmonary airway tree structures." Computers in Biology & Medicine **36**(9): 974-96.

Poulos, L. M., B. G. Toelle, et al. (2005). "The burden of asthma in children: an Australian perspective." Paediatric Respiratory Reviews **6**(1): 20-7.

Rabe, K. F., S. Hurd, et al. (2007). "Global strategy for the diagnosis, management, and prevention of chronic obstructive pulmonary disease: GOLD executive summary.[see comment]." American Journal of Respiratory & Critical Care Medicine **176**(6): 532-55.

Raven, C. (1998). "Numerical removal of ring artifacts in microtomography." Review of Scientific Instruments **69**(8): 2978-2980.

Reid, L. (1976). "Visceral cartilage." Journal of Anatomy **122**(Pt 2): 349-55.

Reinhardt, J. M., N. D'Souza, et al. (1997). "Accurate measurement of intrathoracic airways." Medical Imaging, IEEE Transactions on **16**(6): 820-827.

Remy-Jardin, M., J. Remy, et al. (1998). "Tracheobronchial tree: assessment with volume rendering--technical aspects." Radiology **208**(2): 393-8.

Rennard, S. I. (2002). "Overview of causes of COPD. New understanding of pathogenesis and mechanisms can guide future therapy." Postgraduate Medicine **111**(6): 28-30.

Saba, O. I., E. A. Hoffman, et al. (2003). "Maximizing quantitative accuracy of lung airway lumen and wall measures obtained from X-ray CT imaging." Journal of Applied Physiology **95**(3): 1063-75.

Saetta, M., G. Turato, et al. (2000). "Structural basis for airflow limitation in chronic obstructive pulmonary disease." Sarcoidosis Vasculitis & Diffuse Lung Diseases **17**(3): 239-45.

San Jose Estepar, R., J. J. Reilly, et al. (2008). "Three-Dimensional Airway Measurements and Algorithms." Proceedings of the American Thoracic Society **5**(9): 905-909.

Seneterre, E., F. Paganin, et al. (1994). "Measurement of the internal size of bronchi using high resolution computed tomography (HRCT)[see comment]." European Respiratory Journal **7**(3): 596-600.

Sera, T., H. Fujioka, et al. (2003). "Three-dimensional visualization and morphometry of small airways from microfocal X-ray computed tomography." Journal of Biomechanics **36**(11): 1587-94.

Shofer, S., C. Badea, et al. (2007). "A micro-computed tomography-based method for the measurement of pulmonary compliance in healthy and bleomycin-exposed mice." Experimental Lung Research **33**(3-4): 169-83.

Sugiyama, K., H. Sagara, et al. (2008). "[Advocating the diagnostic criteria for early stage of asthma]." Arerugi - Japanese Journal of Allergology **57**(12): 1275-83.

Suter, M. J., J. M. Reinhardt, et al. (2008). "Integrated CT/bronchoscopy in the central airways: preliminary results." Academic Radiology **15**(6): 786-98.

Tanaka, H., G. Yamada, et al. (2003). "Increased airway vascularity in newly diagnosed asthma using a high-magnification bronchovideoscope." American Journal of Respiratory & Critical Care Medicine **168**(12): 1495-9.

Tschirren, J., E. Hoffman, A., et al. (2004). Airway tree segmentation using adaptive regions of interest. Proceedings of the SPIE. **5369:** 117-124.

Tschirren, J., E. A. Hoffman, et al. (2005). "Segmentation and Quantitative Analysis of Intrathoracic Airway Trees from Computed Tomography Images." Proceedings of the American Thoracic Society **2**(6): 484-487.

Tzeng, Y. S., E. Hoffman, et al. (2007). "Comparison of airway diameter measurements from an anthropomorphic airway tree phantom using hyperpolarized 3He MRI and high-resolution computed tomography." Magnetic Resonance in Medicine **58**(3): 636-42.

Udupa, J. K., V. R. Leblanc, et al. (2006). "A framework for evaluating image segmentation algorithms." Computerized Medical Imaging & Graphics **30**(2): 75-87.

Uzun, H., I. S. Curthoys, et al. (2007). "A new approach to visualizing the membranous structures of the inner ear â€“ high resolution X-ray micro-tomography." Acta Oto-Laryngologica **127**(6): 568 - 573.

Vasiljevic, L. K. and H. K. Khalil (2008). "Error bounds in differentiation of noisy signals by high-gain observers." Systems & Control Letters **57**(10): 856-862.

Venkatraman, R., R. Raman, et al. (2006). "Fully Automated System for Three-Dimensional Bronchial Morphology Analysis Using Volumetric Multidetector Computed Tomography of the Chest." Journal of Digital Imaging **19**(2): 132-139.

Voros, S. and S. Voros (2009). "What are the potential advantages and disadvantages of volumetric CT scanning?" Journal of cardiovascular computed tomography **3**(2): 67-70.

Waknine, Y. (2005). " Orphan Drug Approvals: Bronchitol, Prestara, GTI-2040." Medscape today for WebMD.

Walter, D., B. De Man, et al. (2004). "Future generation CT imaging." Thoracic Surgery Clinics **14**(1): 135-149.

Wang, G. and M. W. Vannier (1994). "Stair-step artifacts in three-dimensional helical CT: an experimental study." Radiology **191**(1): 79-83.

Wang, G., M. W. Vannier, et al. (1999). "Iterative X-ray Cone-Beam Tomography for Metal Artifact Reduction and Local Region Reconstruction." Microscopy and Microanalysis **5**(01): 58-65.

Wang, G., S. Zhao, et al. (2005). "Design, analysis and simulation for development of the first clinical micro-CT scanner1." Academic Radiology **12**(4): 511-525.

Webb, W. R., G. Gamsu, et al. (1984). "CT of a bronchial phantom. Factors affecting appearance and size measurements." Investigative Radiology **19**(5): 394-8.

Weibel, E. R. and D. M. Gomez (1962). "Architecture of the human lung. Use of quantitative methods establishes fundamental relations between size and number of lung structures." Science **137**: 577-85.

West, J. (1998). "Pulmonary Pathophysiology – The Essentials." Williams and Wilkins.

WHO (2008). "Fact sheet number 307 on Asthma."

WHO (2008). "Fact sheet number 315 on chronic obstructive pulmonary disease (COPD)."

Wiemker, R., T. Blaffert, et al. (2004). "Automated assessment of bronchial lumen, wall thickness and bronchoarterial diameter ratio of the tracheobronchial tree using high-resolution CT." International Congress Series **1268**: 967-972.

Wilson, C. B., P. W. Jones, et al. (1997). "Validation of the St. George's Respiratory Questionnaire in bronchiectasis." American Journal of Respiratory & Critical Care Medicine **156**(2 Pt 1): 536-41.

Wilson, T. A. (1967). "Design of the bronchial tree." Nature **213**(5077): 668-9.

Wink, O., W. J. Niessen, et al. (2000). "Fast delineation and visualization of vessels in 3-D angiographic images." IEEE Transactions on Medical Imaging **19**(4): 337-46.

Wood, S. A., J. D. Hoford, et al. (1995). "A method for measurement of cross sectional area, segment length, and branching angle of airway tree structures in situ." Computerized Medical Imaging & Graphics **19**(1): 145-52.

Wood, S. A., E. A. Zerhouni, et al. (1995). "Measurement of three-dimensional lung tree structures by using computed tomography." Journal of Applied Physiology **79**(5): 1687-97.